

Micromorphic media: Interpretation by homogenisation

Dissertation

zur Erlangung des Grades

Doktor der Ingenieurwissenschaften (Dr.-Ing.)

der Naturwissenschaftlich-Technischen Fakultät III

Chemie, Pharmazie, Bio- und Werkstoffwissenschaften
der Universität des Saarlandes

vorgelegt von

Dipl.-Ing. Ralf Jänicke

Saarbrücken

29. April 2010

Tag der Einreichung: 29.04.2010
Tag des Kolloquiums: 12.07.2010

Dekan: Prof. Dr.-Ing. Stefan Diebels
Gutachter: Prof. Dr.-Ing. Stefan Diebels
Prof. Dr. Samuel Forest
Prof. Dr.-Ing. habil. Dr. h.c. Holm Altenbach

Preface

The research presented within this contribution was carried out during my time as a PhD student at the Chair of Applied Mechanics, Saarland University, Saarbrücken, from December 2006 to April 2010.

First of all, I would like to express my gratitude to my adviser Professor Dr.-Ing. Stefan Diebels. Already during my time as a diploma student at his institute, he provided me an environment of scientific stimulation in a pleasant working atmosphere. He always encouraged me to think independently and to act on my own initiative. However, he never lost sight of assisting me during my journey through the mystic world of micromorphic media if necessary. Stefan, special thanks for your unselfish support with regard to the arising changes in my life! Secondly, I would like to thank Professor Samuel Forest. In the very beginning of my time as a PhD student, I had the opportunity to attend his lectures given during a summer school in Udine, Italy. His ideas and his way of thinking micromorphically became formative throughout my work on this field and I have always enjoyed the revealing discussions with him. Special thanks for having been the co-referee of my thesis. Moreover, I would like to thank my second co-referee, Professor Dr.-Ing. habil. Dr. h.c. Holm Altenbach, for his spontaneous support, for his inspiring suggestions and for his interest in my work.

Besides my scientific advisers, the former and the present colleagues from the Chair of Applied Mechanics deserve my special thanks for the always cheerful working atmosphere. Special thanks go to Prof. Dr.-Ing. Holger Steeb, Dr.-Ing. Michael Johlitz and to my project partner Hans-Georg Sehlhorst, MSc, cordially supporting and accompanying me if necessary.

Finally, I would like to thank all my friends and my family, my wife Lilian in particular, for their love, their patience and their encouragement.

Saarbrücken, July 2010

Ralf Jänicke

Abstract

In order to develop more and more resource-saving strategies for engineering tasks, the efficient application of cellular materials, such as various open cell foams, is of high interest in science and technology. Strongly influenced by their underlying microtopology, cellular materials feature a complex material behaviour. Modelling aspects to be taken into account are e. g. the deformation induced evolution of anisotropy and porosity on the one hand and the description of size dependent stiff or soft boundary layers, activated by the interaction close to material interfaces, on the other hand.

The present contribution is focusing on that second feature by introducing a numerical homogenisation procedure. It allows to replace the heterogeneous microcontinuum by a homogeneous micromorphic macrocontinuum. Doing so, the microstructural deformation mechanisms can be geometrically interpreted as generalised degrees of freedom, which can be transferred on the macroscopic level. In the context of a FE^2 strategy, the macroscopic constitutive equations are replaced by the computation of a nested microscopic boundary value problem in each macroscopic material point.

The power of the proposed interpretation of the micromorphic degrees of freedom in combination with the numerical homogenisation approach is demonstrated for several microstructures in various numerical experiments validated in comparison to numerical reference calculations.

Zusammenfassung

In einer Welt immer knapper werdender Rohstoffe kommt dem ressourcenschonenden Einsatz von anwendungsspezifisch optimierten Materialien eine immer höhere Bedeutung zu. Vor diesem Hintergrund werden zelluläre Materialien wie z. B. offenporige Schäume sowohl im Bereich des konstruktiven Leichtbaus als auch für diverse weitere Anwendungsgebiete eingesetzt. Aufgrund ihrer ausgeprägten Mikrotopologie zeichnen sich diese Materialien durch ein komplexes mechanisches Verhalten aus. Für die Materialmodellierung müssen dabei sowohl die Anisotropie und die Porosität Berücksichtigung finden als auch Maßstabeffekte an Materialgrenzen, die sich in steifen oder weichen Randschichten äußern.

Eben diese Maßstabeffekte stehen im Mittelpunkt der vorliegenden Arbeit. Zu ihrer Modellierung wird das zu Grunde liegende heterogene Mikrokontinuum durch ein homogenes mikromorphes Makrokontinuum ersetzt. Dazu müssen die mikroskopischen Deformationsprozesse einer makroskopischen Interpretation als erweiterte Freiheitsgrade zugeführt werden. Dies geschieht mit Hilfe eines numerischen Homogenisierungsverfahrens. Die Formulierung einer makroskopischen Konstitutivbeziehung wird umgangen, indem an jeden makroskopischen materiellen Punkt ein mikroskopisches Randwertproblem geheftet und im jeweiligen Deformationszustand berechnet wird.

Die Leistungsfähigkeit der vorgestellten Homogenisierungstechnik wird anschließend am Beispiel verschiedener Mikrostrukturen und geeigneter Referenzberechnungen nachgewiesen.

Contents

1	Introduction	1
1.1	Motivation and state of research	1
1.2	Scope of this work	5
1.3	Outline	6
1.4	Notations	7
I	Theoretical aspects	9
2	Classical continuum mechanics	11
2.1	Kinematics	11
2.1.1	The physical picture	11
2.1.2	Deformation and strain quantities	13
2.1.3	Material time derivatives	14
2.2	Balance equations	15

3	Homogenisation of Cauchy media	19
3.1	Two-scale modelling	19
3.2	Averaging theorems	21
3.3	Microscopic deformation modes	23
3.4	Hill-Mandel condition	24
3.5	Discussion of the method	27
4	Theory of micromorphic media	29
4.1	Kinematics	30
4.1.1	Physical picture	30
4.1.2	Deformation and strain quantities	31
4.1.3	Material time derivatives	34
4.2	Balance equations	35
5	Homogenisation of micromorphic media	41
5.1	Averaging theorems	42
5.2	Microscopic deformation modes	43
5.3	Extension of the Hill-Mandel condition	49
5.4	Discussion of the method	51

II	Numerical investigations	53
6	Relevance of the higher order deformation modes	57
7	Scale-transition by the higher order deformation modes	65
8	Single-cross microstructures	69
8.1	Microtopology	69
8.2	Experimental setup	70
8.3	Shear test	73
8.4	Tension test	78
8.5	Bending test	79
8.6	Size of the microvolume	82
8.7	Discussion	84
9	Modified single-cross microstructures	85
9.1	Microtopology and experimental setup	85
9.2	Shear test	86
9.3	Discussion	87
10	Honeycomb structure	89
10.1	Microtopology	89

10.2 Shear test	92
10.3 Tension test	95
10.4 Bending test of a sandwich structure	96
10.5 Discussion	104
11 Auxetic structures	105
11.1 Folded honeycomb	106
11.2 Undulated single-cross	108
11.2.1 Tension test	108
11.2.2 Shear test	111
11.3 Discussion	114
12 Discussion of the methodology	119
A Alternative micromorphic projection polynomial	123
B Downwards compatibility	127
C Balance equations in the weak form	131
Bibliography	135

1

Mechanical modelling of cellular materials – an introduction

1.1 Motivation and state of research

Living in times where humankind is more and more influencing and threatening its natural environment, it is the main obligation of science and industry to develop strategies for all of us how to organise our way of living in an as far as possible resource-saving manner. Within this broad subject, the design of novel materials plays an important role. During the last decades, the class of cellular materials has become one focal point of interest among numerous further ones. Due to their low mass density, cellular materials, e. g. ceramic, polymer or metal foams, are widely used for light-weight constructions in various fields of engineering applications. Nevertheless, cellular materials are well-known to feature a peculiar mechanical behaviour. Modelling aspects to be taken into account comprise on the one hand a distinct anisotropy in the effective material behaviour, on the other hand pronounced size-dependent boundary layer effects under various loading conditions. The

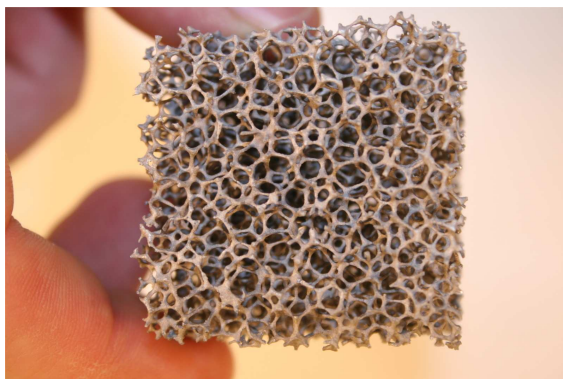


Figure 1.1: Open-cell Aluminium foam (10 ppi, 95 % porosity)

anisotropy effects material properties which depend on the orientation of the microstructure. Furthermore, it is possible that the anisotropy develops during the deformation process due to local reorientations. By contrast, boundary layers mainly occur close to material interfaces, where, in general, the microstructural deformation mechanisms are more restricted than without the interface, cf. [3, 5, 13, 17, 73, 82, 100, 119, 127, 128]. Altogether, one may summarise the overall material properties to be strongly dominated by the particular microtopology. The mechanical modelling of those materials implies an exact knowledge of the underlying microstructure. For open-cell polymer and metal foams, a detailed microscopic characterisation can be found e. g. in [67].

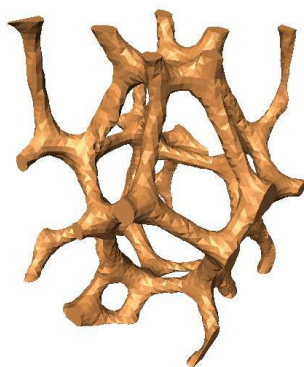


Figure 1.2: Detail of a three-dimensional CT-reconstruction.¹

¹Special thanks to E. Thoma (Fraunhofer IZFP) and M. Engstler (MECS, both at Saarland University, Germany) for the CT-scan and the reconstruction.

For the material modelling of heterogeneous materials, mainly three different approaches are to be found in literature. The first one deals with a microscopic fidelity, resolving the entire microstructure within the Finite Element Method (FEM). On the one hand, this first approach captures all relevant effects due to the microtopology. On the other hand, it generates an immense number of degrees of freedom (DOF), which results in huge equation systems incorporating immense numerical costs from the numerical point of view, at least when considering sufficiently large samples.

The second technique replaces the microheterogeneous material by an appropriate homogeneous material incorporating extended kinematics, i. e. an extended continuum theory. From the historical point of view, this concept goes back to the seminal work of the brothers Cosserat [18] and was later on generalised by Eringen and Mindlin [32, 35, 92]. Initially, the ideas of additional degrees of freedom have found their way into application for the formulation of beams, plates and shells. A detailed review can be found in [2]. Without the restriction to one- or two-dimensional problems and based on the formulations of Günther [54] and Schaefer [108], the Cosserat theory, only assuming microscopic rotations as additional degrees of freedom, has been elaborated in literature e. g. with applications to crystal plasticity, foams, layered or particle systems, making no claim to be complete cf. [6, 7, 12, 20, 21, 27, 28, 30, 31, 43, 45, 95, 126]. Discussions concerning the more general micromorphic continuum, taking into account microstructural shearing and stretching deformations, can be found e. g. in [9, 24, 41, 42, 49, 52, 63, 64, 65, 75, 97, 116]. Except for a few approaches, the microdeformation is considered to be affine, cf. [34, 49]. Special applications to the material modelling of foam structures, with or without extended kinematics, can be found e. g. in [4, 29, 50, 53, 98, 105, 120, 124, 125]. The second gradient continuum theory is representing a further class of extended continuum theories, related to the micromorphic continuum theory via the internal constraint that the microdeformation is not completely independent from the displacement field but equals the macroscopic first deformation gradient, cf. e. g. [16, 44, 47, 48, 77, 79, 93, 96, 102, 103]. Altogether, one may point out the necessity of introducing an extended constitutive modelling involving additional material parameters, cf. e. g. [92, 97], as the main disadvantage of this purely macroscopic approach, because, in general, the extended parameters are hard to interpret from the physical point of view and furthermore hard to identify by experiments. Under certain circumstances, the solution of the inverse problem bears a helpful alternative for the parameter identification e. g. making use of evolution strategies, cf. [106, 110].

As a third strategy, one may combine both above mentioned approaches in terms of a two-scale modelling, commonly called FE^2 modelling. Based on the idea of replacing a heterogeneous microcontinuum by a homogeneous but extended macrocontinuum, the constitutive equations on the macroscale governed by the unknown material parameters are substituted by a small but finite microscale calculation in each macroscopic material point, e. g. [26, 37, 79, 84, 90, 91]. This approach will be the main issue of the following investigations. Finally, in order to complete the considerations found in literature, one should mention the aspect of an efficient numerical modelling within the FE^2 technique. The formulation of a consistent tangent has been discussed e. g. in [78, 89, 90, 109].

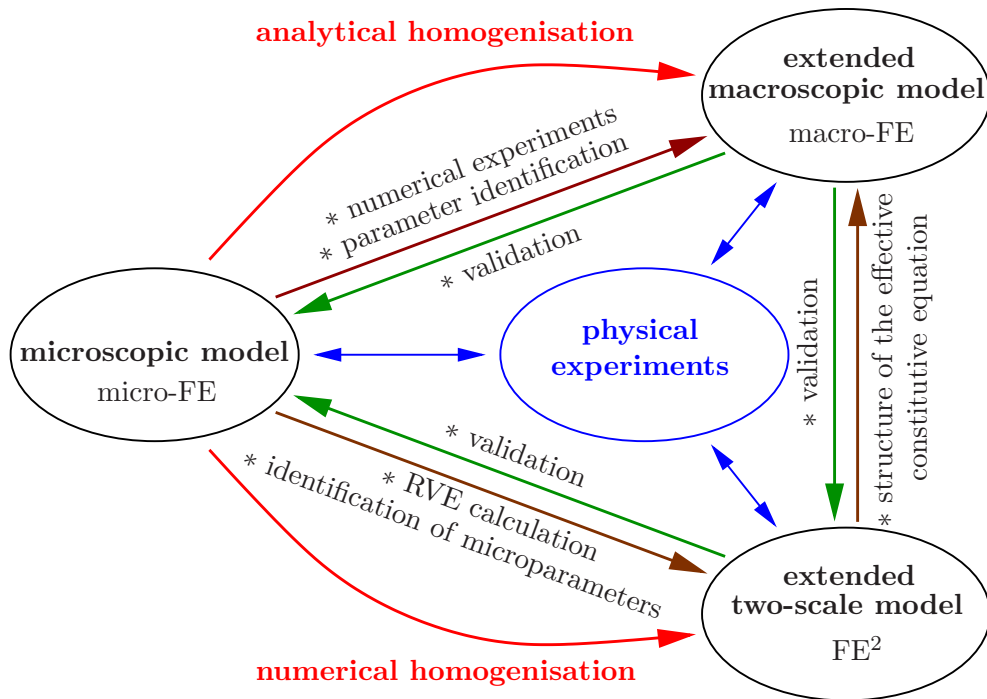


Figure 1.3: Schematic sketch of the three approaches for the material modelling of heterogeneous materials.

In fig. 1.3, the interactions of the three proposed approaches, the microscopic, the macroscopic as well as the mixed one are indicated. From the numerical point of view, the microstructure fully resolved using Finite Elements and applying for a microscopic resolution, i. e. the microscopic model, can be treated as the numerical reference model. Consequently, this model is useful to validate the results achieved by the two homogenisation techniques. With a view to the purely macroscopic model, the results of the numerical reference

experiments can be incorporated e. g. in a genetic parameter identification algorithm. By contrast, the two-scale model requires the solution of a number of microscopic boundary value problems on the level of the Representative Volume Element (RVE) with microscopic resolution. The insights acquired by the numerical homogenisation may be helpful to adjust the structure of the effective constitutive equations within the macroscopic model. Nevertheless, for a material modelling of realistic structures, it is common to all proposed approaches to be verified with respect to physical experiments.

1.2 Scope of this work

The present contribution focuses on a numerical homogenisation technique based on the underlying concept of scale separation [61, 99], also known as the *MMM-principle*. For this purpose, one may distinguish between three different scales of interest: the macro-, the meso- and the microscale. Whereas the macroscale covers the entire sample, the mesoscale represents the level of the microtopology, e. g. the cellular network. If one continues zooming into one arbitrarily chosen strut of the cellular network, one reaches the microscale, which can be e. g. interpreted as the level of atomistic interactions. In the cases, which will be discussed in the latter, this second step can be assumed to be very large. Thus, on the mesoscale, the application of a standard continuum theory is meaningful from the physical point of view. By contrast, the scale separation between the macro- and the mesoscale can not be guaranteed, especially if one is interested in effects depending on a microstructural length scale. Those effects come into play, if the characteristic length scale of the mesolevel becomes comparable to that one of the macrolevel. In the sequel, the present contribution will focus on the scale transition between the macro- and the mesoscale. In order to simplify matters, no considerations concerning the atomistic microscale will be included. By consequence, let us change the above mentioned denotation and let us define the microscale the level of the cellular network in the following investigations.

In order to investigate the micro-to-macro scale transition, a consistent numerical homogenisation scheme will be elaborated replacing a heterogeneous Cauchy microcontinuum by a homogeneous micromorphic macrocontinuum. Introducing this two-scale approach, the following questions are of special interest:

1. What is the physical meaning and the geometrical interpretation of the micromorphic degrees of freedom in terms of deformation modes applied on the boundary of the attached microvolume?
2. Is it possible to observe the predicted deformation modes within the real deformation behaviour of the investigated heterogeneous materials and
3. how does an appropriate formulation of the attached microvolume look like?
4. How can be homogenised the microscopic stress fields resulting in effective stresses and higher order stresses on the effective level?
5. Finally, does the found homogenisation methodology compare favourably with appropriate validation tests and which limits can be detected?

1.3 Outline

In order to answer the raised questions, the present contribution is separated into two parts. The first one comprises the theoretical aspects, starting with the fundamental concepts of classical continuum mechanics in chapter 2. The physical picture of the Cauchy continuum theory will be reviewed paying special attention to the axiomatic introduction of balance laws. Replacing the constitutive model on the macroscopic level applying a numerical homogenisation methodology, chapter 3 is concerned with the formulation of the micro-to-macro transitions within the context of the Cauchy continuum theory. By contrast, chapters 4 and 5 extend the considerations of the previous chapters in a systematical manner and in strict analogy to the classical theory. Thus, the physical picture of the micromorphic continuum theory will be considered as well as the extended balance laws. An appropriate homogenisation algorithm will be derived assigning the micromorphic degrees of freedom a clear geometrical interpretation.

The second part of this work is dedicated to the application of the introduced homogenisation technique within various numerical investigations. Whereas chapters 6 and 7 study the basic features of the method, chapters 8 – 11 on the one hand demonstrate the power of the proposed two-scale approach

and on the other hand try to detect the limits of the method. For that purpose, various microstructures will be subject to appropriate numerical experiments.

Finally, the found results will be summarised and discussed in chapter 12. An outlook to ongoing projects will be given.

1.4 Notations

In the sequel, differential operators will be defined as follows:

$$\operatorname{div} \mathbf{T} = \frac{\partial T_{kl}}{\partial x_l} \mathbf{e}_k, \quad \operatorname{GRAD} \mathbf{P} = \frac{\partial P_{kK}}{\partial X_L} \mathbf{e}_k \otimes \mathbf{e}_K \otimes \mathbf{e}_L,$$

where small operators and indices refer to the spatial, capital operators and indices to the material frame. Without loss of generality, the \mathbf{e}_k are the vectors of an orthonormal basis of space making use of the associated Cartesian coordinates. Tensor products read

$$\begin{aligned} \mathbf{A} \cdot \mathbf{B} &= A_{kl} B_{lm} \mathbf{e}_k \otimes \mathbf{e}_m, & \mathbf{A} : \mathbf{B} &= A_{kl} B_{kl}, \\ \underline{\mathbf{E}} &= \varepsilon_{klm} C_{klm}, & \mathbf{C}^{\underline{\mathbf{3}}} : (\mathbf{A}, \mathbf{B}) &= C_{klm} A_{ln} B_{mo} \mathbf{e}_k \otimes \mathbf{e}_n \otimes \mathbf{e}_o. \end{aligned}$$

Furthermore the following permutation and identity tensors will be used:

$$\begin{aligned} \mathbf{I} &= \delta_{kl} \mathbf{e}_k \otimes \mathbf{e}_l, & \text{where } \delta_{kl} &= \begin{cases} 1, & k = l, \\ 0, & \text{else.} \end{cases} \\ \underline{\mathbf{E}} &= \varepsilon_{klm} \mathbf{e}_k \otimes \mathbf{e}_l \otimes \mathbf{e}_m, & \text{where } \varepsilon_{klm} &= \begin{cases} 1, & klm = 123, 231, 312, \\ -1, & klm = 321, 213, 132, \\ 0, & \text{else.} \end{cases} \\ \underline{\mathbf{I}} &= \delta_{klmn} \mathbf{e}_k \otimes \mathbf{e}_l \otimes \mathbf{e}_m \otimes \mathbf{e}_n, & \text{where } \delta_{klmn} &= \begin{cases} 1, & k = l = m = n, \\ 0, & \text{else.} \end{cases} \end{aligned}$$

Besides the permutation tensors, tensors of grade 3 and higher are denoted with underlined indices, e. g. $\underline{\mathbf{C}}^{\underline{\mathbf{3}}}$. Further notations follow the system to be found in [11].



Theoretical aspects

2

Classical continuum mechanics

Without going too much into detail, the following chapter is devoted to a review of the classical continuum mechanics, i. e. for the so-called Cauchy continuum, how it may be found, beyond various other publications, in [1, 8, 58, 123]. In general, the idea of continuum mechanics is up to the description of the motion and the deformation of a physical body \mathcal{B} , consisting of an infinite set of material points P , which convey the physical properties of the body, e. g. the mass density, stresses and so on. At first, the kinematic quantities of the Cauchy continuum theory will be motivated.

2.1 Kinematics

2.1.1 The physical picture

In order to describe a motion and/or deformation of the physical body \mathcal{B} within the Cauchy continuum theory, one introduces the motion function

$\hat{\mathbf{x}}$ which carries an arbitrary chosen material point X from the reference configuration (undeformed state, $t = t_0$, material frame) to the current configuration (deformed state, $t > t_0$, spatial frame). The material point is defined by its position vector \mathbf{X} or \mathbf{x} , respectively, cf. fig. 2.1.

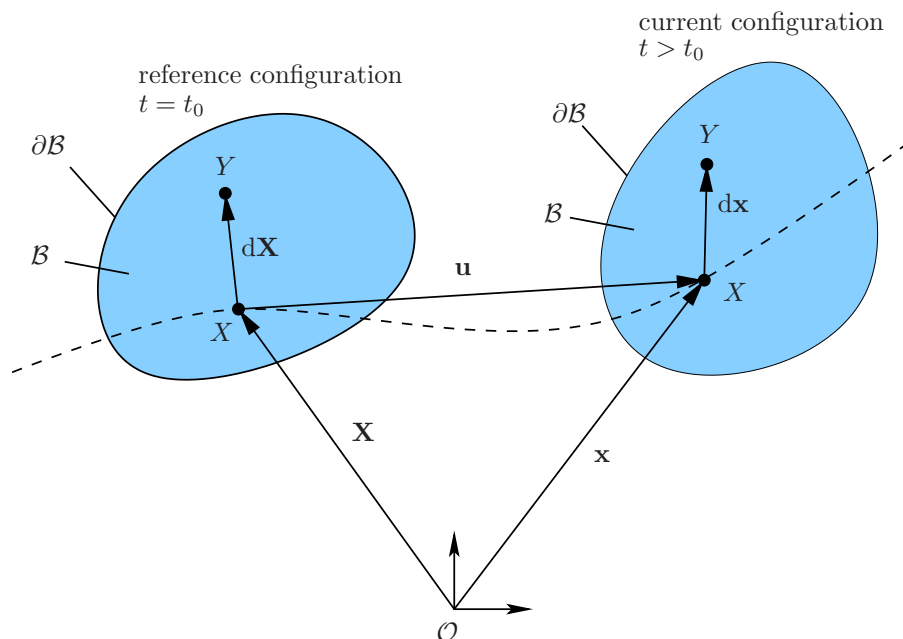


Figure 2.1: The physical picture of the Cauchy continuum: reference and current configuration.

The motion function of the material point X may be written as

$$\mathbf{x} = \hat{\mathbf{x}}(\mathbf{X}, t), \quad \mathbf{X} = \hat{\mathbf{x}}^{-1}(\mathbf{x}, t). \quad (2.1)$$

By derivation with respect to the time t , one obtains the velocity vector in the material frame,

$$\mathbf{v} = \mathbf{x}' = \frac{d\hat{\mathbf{x}}(\mathbf{X}, t)}{dt}. \quad (2.2)$$

In the spatial frame, one finds

$$\mathbf{v} = \mathbf{x}'(\hat{\mathbf{x}}^{-1}(\mathbf{x}, t), t). \quad (2.3)$$

The displacement vector \mathbf{u} points from the reference position of the material

point to its current position and, therefore, it is defined as¹

$$\mathbf{u}(\mathbf{X}, t) = \hat{\mathbf{x}}(\mathbf{X}, t) - \mathbf{X} = \mathbf{x} - \mathbf{X}. \quad (2.4)$$

2.1.2 Deformation and strain quantities

The derivative of the motion function $\hat{\mathbf{x}}$ with respect to the reference position \mathbf{X} results in the definition of the deformation gradient

$$\mathbf{F} = \frac{\partial \hat{\mathbf{x}}(\mathbf{X}, t)}{\partial \mathbf{X}} = \frac{\partial \mathbf{x}}{\partial \mathbf{X}} = \text{GRAD } \mathbf{x} = \text{GRAD } \mathbf{u} + \mathbf{I}. \quad (2.5)$$

It projects the line element between two proximate material points from the material to the spatial frame, i. e.

$$d\mathbf{x} = \mathbf{F} \cdot d\mathbf{X}. \quad (2.6)$$

Moreover, one may identify the transport rules for surface and volume elements as

$$da = (\det \mathbf{F}) \mathbf{F}^{T-1} \cdot d\mathbf{A}, \quad dv = \det \mathbf{F} dV. \quad (2.7)$$

The deformation gradient can be decomposed multiplicatively as the product of a proper orthogonal and a symmetric tensor,

$$\mathbf{F} = \mathbf{R} \cdot \mathbf{U} = \mathbf{V} \cdot \mathbf{R}, \quad (2.8)$$

where

$$\mathbf{R}^T = \mathbf{R}^{-1}, \quad \det \mathbf{R} = +1, \quad \mathbf{U} = \mathbf{U}^T, \quad \mathbf{V} = \mathbf{V}^T. \quad (2.9)$$

In practise, the calculation of the stretch tensors \mathbf{U} and \mathbf{V} requires the solution of an eigenvalue problem which is quite complex. However, computing the squares of the line elements, it is possible to define more manageable

¹No distinction between the function and its value.

deformation quantities,

$$dS^2 = d\mathbf{X} \cdot d\mathbf{X}, \quad ds^2 = d\mathbf{x} \cdot d\mathbf{x}. \quad (2.10)$$

Making use of the transport theorem eq. (2.6), one finds

$$ds^2 = (\mathbf{F}^T \cdot \mathbf{F}) : (d\mathbf{X} \otimes d\mathbf{X}), \quad (2.11)$$

$$dS^2 = (\mathbf{F}^{T-1} \cdot \mathbf{F}^{-1}) : (d\mathbf{x} \otimes d\mathbf{x}) \quad (2.12)$$

and one may define

$$\mathbf{C} = \mathbf{F}^T \cdot \mathbf{F} = \mathbf{U}^2 \quad \text{and} \quad \mathbf{B} = \mathbf{F} \cdot \mathbf{F}^T = \mathbf{V}^2 \quad (2.13)$$

the right and the left Cauchy-Green deformation tensor. By definition, they do not involve any rigid body rotation, i. e. the right as well as the left Cauchy-Green deformation tensor can be expressed solely by the stretch tensors \mathbf{U} and \mathbf{V} , respectively.

Finally, calculating the differences of squares of line elements, the definitions of the Green-Lagrange and the Euler-Almansi strain tensors read

$$\mathbf{E} = \frac{1}{2}(\mathbf{C} - \mathbf{I}) \quad \text{and} \quad \mathbf{A} = \frac{1}{2}(\mathbf{I} - \mathbf{B}^{-1}). \quad (2.14)$$

2.1.3 Material time derivatives

So far, no variations of the deformation quantities in time have been taken into account. To do so, the material or the total time derivative of the expression $(\diamond)(\mathbf{x}, t)$ is defined as

$$(\diamond)' = \frac{d(\diamond)}{dt} = \frac{\partial(\diamond)}{\partial t} + \text{grad}(\diamond) \cdot \mathbf{x}'. \quad (2.15)$$

The material time derivative of the transport theorem eq. (2.6) reads

$$(d\mathbf{x})' = \frac{d}{dt}(\mathbf{F} \cdot d\mathbf{X}) = \mathbf{F}' \cdot d\mathbf{X} = \mathbf{F}' \cdot \mathbf{F}^{-1} \cdot d\mathbf{x}. \quad (2.16)$$

One distinguishes between the material velocity gradient

$$\mathbf{F}' = \text{GRAD } \mathbf{v} \quad (2.17)$$

and the spatial velocity gradient

$$\mathbf{L} = \text{grad } \mathbf{v} = \mathbf{F}' \cdot \mathbf{F}^{-1}. \quad (2.18)$$

2.2 Balance equations

Besides the kinematic expressions, describing the motion or deformation of a physical body \mathcal{B} , the concept of continuum mechanics requires every physical system to equilibrate itself with respect to its environment. I. e., one has to introduce balance equations in an axiomatic way, cf. [21, 58]. In the following, the method of virtual power will be applied to generate the underlying balance equations for the Cauchy continuum theory. The method has been described in detail e. g. in [48, 51, 56].

The forces acting on the body \mathcal{B} can be distinguished into external forces, representing the interaction with other bodies, and internal forces, involving all effects within the body \mathcal{B} . The principle of virtual power says:

“For any arbitrary virtual motion, the virtual power of all the internal and external forces acting on the body \mathcal{B} equals zero” [48].

Thus, one may write

$$\delta P_i + \delta P_e = 0, \quad (2.19)$$

where δP_i and δP_e describe the virtual power of the internal and the external forces. For the Cauchy continuum, the power of the internal forces is assumed to be a linear form of the gradient of the virtual velocity,

$$\delta P_i = - \int_{\mathcal{B}} \delta p_i \, dv \quad (2.20)$$

with

$$\delta p_i = \mathbf{T} : \text{grad } \delta \mathbf{v}, \quad (2.21)$$

\mathbf{T} is called the Cauchy stress tensor. The principle furthermore demands the power of the internal forces to stay constant even if the observer changes its position, i. e. the power of the internal forces has to be invariant with respect to a superimposed rigid body transformation within the manifold of the Euclidean transformations. Consequently, the virtual velocity $\delta \mathbf{v}$ may be replaced by $\delta \mathbf{v} + \bar{\mathbf{v}} + \bar{\boldsymbol{\Omega}} \cdot \mathbf{x}$, where $\bar{\mathbf{v}}$ is representing a rigid body translation and $\bar{\boldsymbol{\Omega}}$ a rigid body rotation, both constant within \mathcal{B} . Furthermore, for $\bar{\boldsymbol{\Omega}}$, the orthogonality condition holds. Inserting these expressions into eq. (2.21) and taking into account the invariance postulate, one finds

$$\delta p_i - \delta \bar{p}_i = \mathbf{T} : \text{grad } \delta \mathbf{v} - (\mathbf{T} : \text{grad } \delta \mathbf{v} + \mathbf{T} : \bar{\boldsymbol{\Omega}}) \stackrel{!}{=} 0. \quad (2.22)$$

For an arbitrary rigid body rotation $\bar{\boldsymbol{\Omega}}$ and considering its orthogonality, this condition is fulfilled for the setting

$$\mathbf{T} = \mathbf{T}^T, \quad (2.23)$$

i. e. the Cauchy stress tensor \mathbf{T} is symmetric in the spatial framework.

For the virtual power of the external forces, one may assume

$$\delta P_e = \int_{\mathcal{B}} \rho \mathbf{b} \cdot \delta \mathbf{v} \, dv + \int_{\partial \mathcal{B}} \mathbf{t} \cdot \delta \mathbf{v} \, da \quad (2.24)$$

with the mass density ρ , the volume force density \mathbf{b} and the surface traction \mathbf{t} . After an integration in parts and after having applied the divergence theorem, the principle of virtual power eq. (2.19) reads

$$\int_{\mathcal{B}} \delta \mathbf{v} \cdot (\text{div } \mathbf{T} + \rho \mathbf{b}) \, dv + \int_{\partial \mathcal{B}} \delta \mathbf{v} \cdot (\mathbf{t} - \mathbf{T} \cdot \mathbf{n}) \, da = 0, \quad (2.25)$$

which must be satisfied for any virtual motion $\delta \mathbf{v}$. The principle of virtual

power is satisfied, if one chooses the equilibrium condition

$$\operatorname{div} \mathbf{T} + \rho \mathbf{b} = \mathbf{0} \text{ in } \mathcal{B}, \quad (2.26)$$

identical to the **balance of momentum**, and the boundary condition

$$\mathbf{T} \cdot \mathbf{n} = \mathbf{t} \text{ on } \partial \mathcal{B} \quad (2.27)$$

with the outer normal vector \mathbf{n} on the surface $\partial \mathcal{B}$ in the spatial description.

The symmetry condition for the Cauchy stress \mathbf{T} , eq. (2.23), can be transformed into the so-called **balance of moment of momentum** of the Cauchy continuum theory and reads in the notation following [11]

$$\mathbf{I} \times \mathbf{T} = \overset{3}{\mathbf{E}} : \mathbf{T}^T = \mathbf{0}. \quad (2.28)$$

Up to now, the method of virtual power has been formulated in the spatial frame. Following the concept of dual variables [59] and assuming the virtual power of the internal forces to be an objective quantity, cf. [48], the balance laws can be written for the material frame in an analogous way. The transport from the spatial into the material frame is making use of the transport theorems eqs. (2.6–2.7). Thus, the material form of the balance of momentum reads

$$\operatorname{Div} \mathbf{P} + \rho_0 \mathbf{b} = \mathbf{0} \quad (2.29)$$

and the material form of the balance of moment of momentum

$$\mathbf{F} \times \mathbf{P} = \overset{3}{\mathbf{E}} : (\mathbf{F} \cdot \mathbf{P}^T) = \mathbf{0}. \quad (2.30)$$

Via the concept of dual quantities, one obtains

$$\int_{\mathcal{B}} \mathbf{T} : \mathbf{L} \, dv = \int_{\mathcal{B}} ((\det \mathbf{F}) \mathbf{T} \cdot \mathbf{F}^{T-1}) : \mathbf{F}' \, dV. \quad (2.31)$$

The dual stress quantity can be identified as the 1st Piola-Kirchhoff stress

tensor

$$\mathbf{P} = (\det \mathbf{F}) \mathbf{T} \cdot \mathbf{F}^{T-1}. \quad (2.32)$$

Note that, in general, the 1st Piola-Kirchhoff stress tensor is not symmetric.

If one replaces the virtual by real deformations, one may balance the change of the energy stored within the body \mathcal{B} . If one furthermore neglects accelerations, heat production and thermal radiation effects, i. e. one assumes the static and isothermal case, the balance of internal energy equals the balance of strain energy. In the spatial frame, one writes

$$\frac{d}{dt} \int_{\mathcal{B}} \rho \varepsilon \, dv = \int_{\mathcal{B}} \rho \mathbf{b} \cdot \mathbf{v} \, dv + \int_{\partial \mathcal{B}} \mathbf{t} \cdot \mathbf{v} \, da \quad (2.33)$$

and after some conversions, using the divergence theorem and the balance equations eqs. (2.26) and (2.28), one finds the balance of strain energy in the local form

$$\rho \varepsilon' = \mathbf{T} : \text{grad } \mathbf{v}. \quad (2.34)$$

The transformation into the material frame results in

$$\rho_0 \varepsilon' = \mathbf{P} : \mathbf{F}', \quad (2.35)$$

where ε defines the internal energy density of the system. Further balance laws exist for the conservation of mass and the balance of entropy, i. e. the second law of thermodynamics. The numerical experiments within the present work are restricted to the static case and to elastic material properties, a potential character for the free energy of the system is assumed. Neither the mass inertia nor entropic effects will be furthermore discussed. Details concerning these balances may be found in the above cited literature.

3

Homogenisation of Cauchy media

3.1 Two-scale modelling

As it has been emphasised in the very beginning, it is the aim of the present work to find an efficient methodology to describe the material behaviour of heterogeneous media, especially that one of cellular materials such as open-cell foams. Let us start our investigations reviewing the so-called first order FE^2 approach, which has been initially introduced in the late 1990s by Feyel et al. [37, 38], whereas the basic principles concerning the homogenisation technique may be found earlier, e. g. [61, 87, 99]. During the past decade, the FE^2 methodology has found its way into the modelling of microstructured materials for various applications, cf. e. g. [55, 66, 88, 90, 91, 94, 114, 115, 122]. The algorithm is based on the insight that the effective mechanical behaviour of heterogeneous materials, i. e. the behaviour one observes on the macroscopic level, is strictly dominated by the underlying microtopology. Thus, the material modelling must take into account the inherent microscale. Whereas purely macroscopic models are based on constitutive assumptions on the effective level, the two-scale approach substitutes the constitutive equations with a set of microscale calculations. In other words, the first order

FE² scheme replaces a heterogeneous microcontinuum by a homogeneous macrocontinuum.¹ The algorithm is sketched in fig. 3.1 in a schematic way. A microscopic volume element comprising the characteristic length l is attached to every macroscopic material point. From the numerical point of view, the microvolume is attached to every macroscopic integration point. Within a first order FE² scheme, the microscopic volume element is assumed to be very small compared to the macroscopic length scale ($l \ll L$) and it has to be representative for the microheterogeneity.²

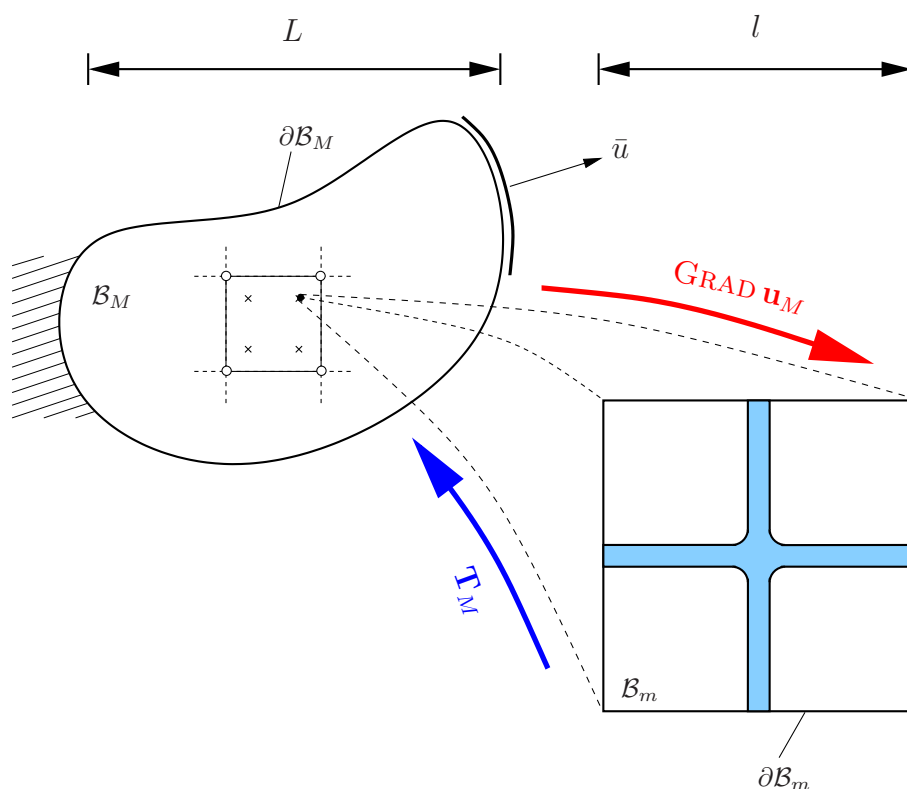


Figure 3.1: The basic principle of the FE² method.

Considering fig. 3.1, a macroscopic boundary value problem is given and the deformation quantities, for the Cauchy continuum theory only the displacement gradient, have to be projected to the boundary of the attached microvolume. Therewith, a microscopic Dirichlet boundary value problem has been generated which can be solved. By formulation of an appropriate homogenisation rule, the microscopic stress quantities have to be transferred

¹By contrast, FE² techniques using a higher order macroscopic continuum theory are called higher order.

²One may allude that, in general, it is not a trivial task at all to determine the appropriate size of the microscopic volume element.

back to the macroscale, resulting e. g. in the macroscopic Cauchy stress tensor \mathbf{T}_M .³ Hence, instead of computing the heterogeneous material with a microscopical resolution, the microscale calculations are restricted to the solution of a number of microscopic boundary value problems. Depending on the size and the complexity of the macroscopic boundary value problem, the method may be still expensive in a numerical sense. But otherwise, it may become very efficient if making use of parallel computing techniques, cf. [81, 111].

The following chapter intends to give a general overview of the well-known first order FE² method, i. e. the heterogeneous Cauchy microcontinuum will be replaced by a homogeneous Cauchy macrocontinuum before the methodology will undergo a consistent extension towards a micromorphic macrotheory in chapter 5. At first, let us derive appropriate projection and homogenisation rules for the transition between the different scales.

To do so, one has to identify the macroscopic kinematic quantities, i. e. the macroscopic displacement field and the macroscopic deformation gradient, in terms of a polynomial mean field and a periodic fluctuation of the heterogeneous Cauchy microvolume attached to the macroscopic material point. To simplify matters, the methodology is restricted to the two-dimensional case. The microvolume attached to the macroscopic material point is assumed to be a rectangular unit cell with the edge lengths a and b and capturing the space \mathcal{B}_m comprising the volume $V_m = ab$. Let \mathbf{X}_M be the volume centroid of \mathcal{B}_m , cf. fig. 3.2.

3.2 Averaging theorems

Let us investigate at first the scale transition properties of the microscopic and the macroscopic displacement fields. In the sequel, quantities depicted with $(\diamond)_m$ refer to the microscale whereas quantities depicted with $(\diamond)_M$ refer to the macroscale. One may postulate the displacement field \mathbf{u}_M to characterise the macrostate that best fits the microscopic displacement field \mathbf{u}_m

³Vice versa, it is also possible to project the macroscopic stresses in order to generate a microscopic Neumann boundary value problem, cf. [99]. It is very interesting to notice this choice to influence the micro-to-macro transition of conservation laws such as the mass conservation, cf. [121]. In order to circumvent these problems, the present work is restricted to microscopic Dirichlet boundary value problems.

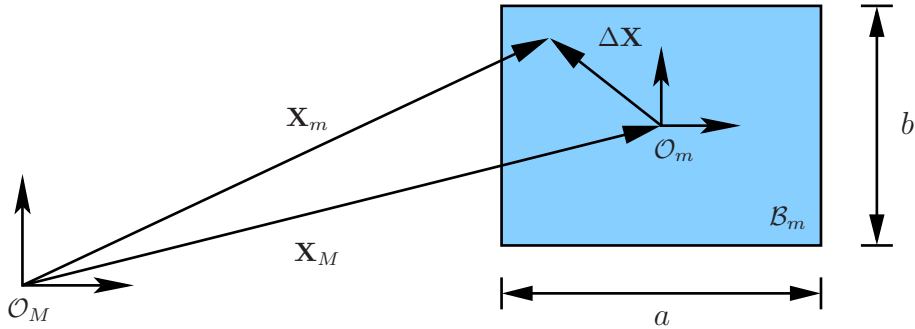


Figure 3.2: The microvolume of the size $V_m = a b$ attached to the macroscopic material point at the position \mathbf{X}_M (material frame).

in the volume average over \mathcal{B}_m , i. e. the real displacement field observed on the heterogeneous microscale has to be replaced by an appropriate, effective displacement field on the homogeneous macroscale. Thus, the minimum of the functional

$$\mathcal{F}(\mathbf{u}_M) = \langle (\mathbf{u}_m - \mathbf{u}_M)^2 \rangle \quad (3.1)$$

has to be computed, where

$$\langle \diamond \rangle = \frac{1}{V_m} \int_{\mathcal{B}_m} (\diamond) dV \quad (3.2)$$

denotes the volume average of the quantity $\langle \diamond \rangle$. By formal derivation of the functional, one finds

$$d\mathcal{F} = -2 \langle \mathbf{u}_m - \mathbf{u}_M \rangle \stackrel{!}{=} \mathbf{0}. \quad (3.3)$$

Equivalently, using the identity $\Delta \mathbf{u} = \mathbf{u}_m - \mathbf{u}_M$, one may write

$$\langle \Delta \mathbf{u} \rangle = \mathbf{0}. \quad (3.4)$$

From the physical point of view, eq. (3.4) emphasises the microscopic displacement field, besides the rigid body displacement \mathbf{u}_M , to vanish in the average over the microvolume. The microscopic displacement field can be interpreted as a microscale fluctuation of a wave length, which is infinitesimally short compared to the characteristic wave length of the macroscopic deforma-

tion field. Thus, in the average over the microvolume, the microfluctuation does not result in an effective displacement visible on the macroscale.

Applying the gradient operator on the particular scales, one finally may identify the expression

$$\frac{d\mathbf{u}_M}{d\mathbf{X}_M} = \left\langle \frac{d\mathbf{u}_m}{d\mathbf{X}_m} \right\rangle \quad (3.5)$$

or equivalently

$$\text{GRAD } \mathbf{u}_M = \langle \text{GRAD } \mathbf{u}_m \rangle. \quad (3.6)$$

3.3 Microscopic deformation modes

So far, the relations between the macroscopic and the microscopic kinematic quantities have been identified. Keeping in mind the FE² algorithm depicted above, one now has to derive a projection rule, which is admissible with respect to the averaging rules eqs. (3.4) and (3.6).

To do so, let us assume the microscopic displacement field to be a polynomial of grade one, i. e.

$$\Delta \mathbf{u} = \mathbf{A}_M^1(\mathbf{X}_M, t) + \mathbf{B}_M^2(\mathbf{X}_M, t) \cdot \Delta \mathbf{X} + \Delta \tilde{\mathbf{u}}, \quad (3.7)$$

where the displacement $\Delta \tilde{\mathbf{u}}$ is representing a fluctuation field due to microstructural periodicity. The coefficients \mathbf{A}_M^1 and \mathbf{B}_M^2 solely depend on the macroscopic position \mathbf{X}_M and the time t . Hence, these quantities are constant within the microvolume.

One now may compute \mathbf{u}_M and $\text{GRAD } \mathbf{u}_M$ inserting eq. (3.7) into eqs. (3.4) and (3.6) and one obtains the macroscopic kinematic quantities in terms of the coefficient tensors. Solving the resulting equation system, this procedure allows vice versa to express the coefficient tensors in terms of the macroscopic

quantities. Doing so, one finds

$$\mathbf{A}_M^1 = \mathbf{0}, \quad (3.8)$$

$$\mathbf{B}_M^2 = \text{GRAD } \mathbf{u}_M. \quad (3.9)$$

From the physical point of view, eq. (3.8) ensures rigid body translations to be excluded. Applying the canonical decomposition of the displacement gradient,

$$\text{GRAD } \mathbf{u}_M = \text{GRAD}^{\text{sym}} \mathbf{u}_M + \text{GRAD}^{\text{skw}} \mathbf{u}_M, \quad (3.10)$$

one finds the skew-symmetric part of the displacement gradient to cause a rigid body rotation, cf. fig. 3.3 c), i. e. the skew-symmetric mode is deformation and therefore stress free. Thus, it is admissible to restrict the identity eq. (3.9) to the symmetric part and one writes

$$\mathbf{B}_M^2 = \text{GRAD } \mathbf{u}_M^{\text{sym}}. \quad (3.11)$$

Finally, the projection rule for the first order FE² methodology reads

$$\Delta \mathbf{u} = \text{GRAD}^{\text{sym}} \mathbf{u}_M \cdot \Delta \mathbf{X} + \Delta \tilde{\mathbf{u}}. \quad (3.12)$$

Consequently, one distinguishes three independent deformation modes, depending on the three components of the symmetric displacement gradient in the two-dimensional case, which are, besides the skew-symmetric deformation mode, depicted in fig. 3.3 a), b) and d).

3.4 Hill-Mandel condition

After the projection of the macroscopic deformation quantities to the boundary of the microvolume, the microscopic boundary value problem can be solved. Now, the microstructural stress response has to be transferred back to the macroscale. Again, appropriate averaging rules have to be determined. In the sequel, the fundamental assumption to derive the so-called homogenisation procedure is the equivalence of the macroscopic and the microscopic

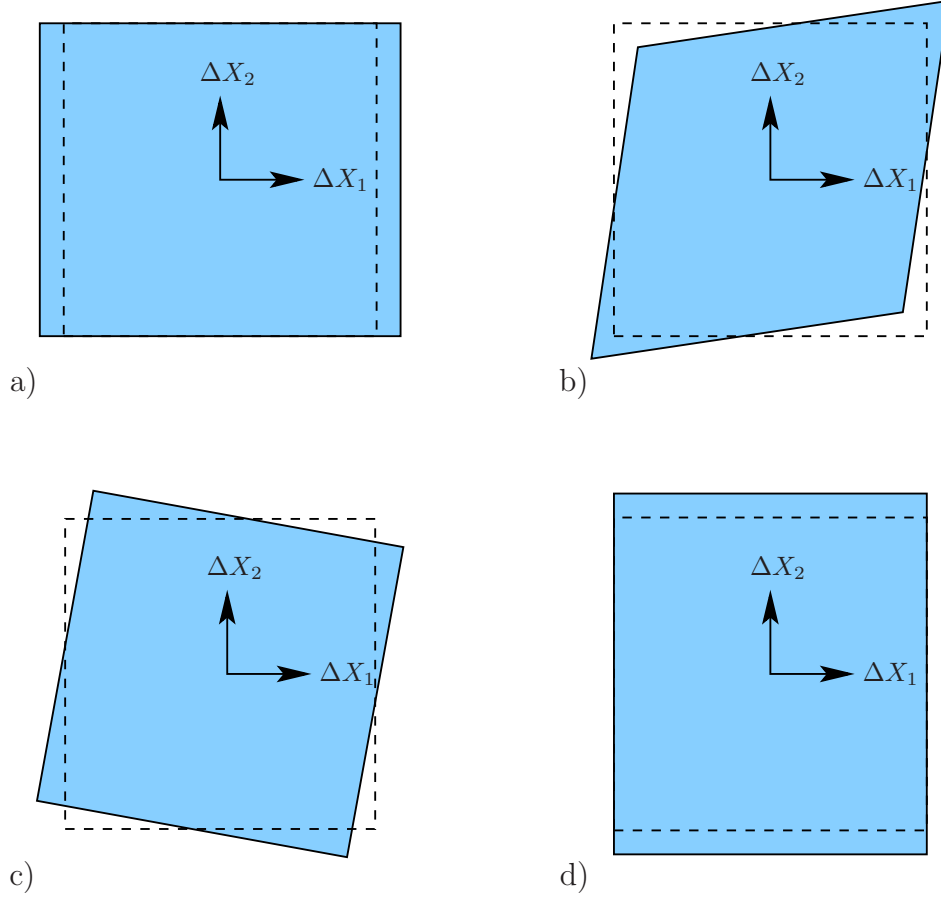


Figure 3.3: The linear deformation modes for the first order FE² approach, depending on a) $u_{M1,1}$, b) $\frac{1}{2}(u_{M1,2} - u_{M2,1})$, c) $\frac{1}{2}(u_{M1,2} + u_{M2,1})$ and d) $Tu_{M2,2}$ for a quadratic microvolume. The skew-symmetric shear mode c) describes a rigid body rotation and is not taken into account within the first order FE² scheme.

strain energy rate, i. e. the rate of the strain energy in the average over the microvolume must equal the strain energy rate in the macroscopic material point the microvolume is attached to. This correlation is commonly called Hill-Mandel condition, cf. e. g. [61, 62, 87, 99] and reads for the static and isothermal case and in the material frame

$$\langle \mathbf{P}_m : \text{GRAD } \Delta \mathbf{u}' \rangle = \mathbf{P}_M : \text{GRAD } \mathbf{u}'_M. \quad (3.13)$$

Integrating the left-hand side of eq. (3.13) by parts, inserting the material form of the balance of momentum eq. (2.29) and furthermore applying the boundary condition in the material framework, $\mathbf{p}_m = \mathbf{P}_m \cdot \mathbf{N}$, where \mathbf{p}_m denotes the traction vector on the referential surface and \mathbf{N} the referential surface normal vector, one finds

$$\begin{aligned} \langle \mathbf{P}_m : \text{GRAD } \Delta \mathbf{u}' \rangle &= \frac{1}{V_m} \int_{\mathcal{B}_m} \mathbf{P}_m : \text{GRAD } \Delta \mathbf{u}' \, dV \\ &= \frac{1}{V_m} \int_{\mathcal{B}_m} \text{DIV} (\mathbf{P}_m^T \cdot \Delta \mathbf{u}') \, dV \\ &= \frac{1}{V_m} \int_{\partial \mathcal{B}_m} \mathbf{p}_m \cdot \Delta \mathbf{u}' \, dA. \end{aligned} \quad (3.14)$$

Calculating the time derivative of eq. (3.12), one obtains the microscopic velocity field to be a function of the time derivatives of the polynomial coefficients,

$$\Delta \mathbf{u}' = \text{GRAD } \mathbf{u}'_M(\mathbf{X}_M, t) \cdot \Delta \mathbf{X} + \Delta \tilde{\mathbf{u}}'. \quad (3.15)$$

Note that according to eq. (3.14), the projection rule only has to be applied on the boundary of the microvolume. Inserting eq. (3.15) into eq. (3.14), one finds

$$\langle \mathbf{P}_m : \text{GRAD } \Delta \mathbf{u}' \rangle = \frac{1}{V_m} \int_{\partial \mathcal{B}_m} \mathbf{p}_m \cdot (\text{GRAD } \mathbf{u}'_M \cdot \Delta \mathbf{X} + \Delta \tilde{\mathbf{u}}') \, dA. \quad (3.16)$$

By further transformations, it follows

$$\begin{aligned} \langle \mathbf{P}_m : \text{GRAD } \Delta \mathbf{u}' \rangle &= \frac{1}{V_m} \int_{\partial \mathcal{B}_m} (\mathbf{p}_m \otimes \Delta \mathbf{X}) \, dA : \text{GRAD } \mathbf{u}'_M \\ &\quad + \frac{1}{V_m} \int_{\partial \mathcal{B}_m} \mathbf{p}_m \cdot \Delta \tilde{\mathbf{u}}' \, dA. \end{aligned} \quad (3.17)$$

Comparing this result to the Hill-Mandel condition eq. (3.13), one finds

$$\mathbf{P}_M = \frac{1}{V_m} \int_{\partial\mathcal{B}_m} (\mathbf{p}_m \otimes \Delta\mathbf{X}) \, dA. \quad (3.18)$$

Concerning the periodic fluctuations $\Delta\tilde{\mathbf{u}}$, one may establish opposite parts of the microvolume boundary $\partial\mathcal{B}_m^{0+}$ and $\partial\mathcal{B}_m^{0-}$ in a way that the correlation $\mathbf{N}^+ = -\mathbf{N}^-$ holds for the outer normal vectors of corresponding points on $\partial\mathcal{B}_m^{0+}$ and $\partial\mathcal{B}_m^{0-}$. The periodic fluctuations do not account for the strain energy for periodic displacements and anti-periodic tractions on opposite parts of the boundary,

$$\Delta\mathbf{u}^+ = \Delta\mathbf{u}^- \quad \text{and} \quad \mathbf{p}_m^+ = -\mathbf{p}_m^-, \quad (3.19)$$

cf. e. g. [87].

3.5 Discussion of the method

Finally, the first order FE² algorithm is complete and the effective macroscopic material law has successfully been substituted by a microscale calculation in combination with appropriate projection and homogenisation rules. Thus, this approach allows for a straight-forward calculation of the effective material behaviour.

Nevertheless, one should mention that the first order FE² approach does not bring into action any correlation between the size of the microvolume and the stiffness of the effective material properties.⁴ I. e. the method exhibits a strictly local character including a perfect scale separation between the macro- and the microscale. From the physical point of view, the characteristic microstructural length scale has to be very small compared to the macroscopic length scale ($l \ll L$). For the case that both length scales become comparable, the microscopic length scale governs the effective material

⁴In fact, a too restrictive choice of the boundary conditions may pretend a size sensitivity. But in that case it is not sensitive to the internal length scale, e. g. the size of the microheterogeneities, but to the size of the too stiff boundary layer within the attached microvolume.

behaviour and the first order methodology will fail. This case will be investigated in detail within the numerical part of the present work.

For further discussions concerning the size of the so-called representative microvolume, the choice of the microscopic boundary conditions etc., it may be referred to the literature. A humble survey may be found in the above cited publications.

4

Theory of micromorphic media

In order to enable the homogeneous macrocontinuum to exhibit the information of a characteristic microscopic length scale in an inherent way, the micromorphic continuum theory extends the physical understanding of the material points. Whereas the classical continuum theory is considering the material points to feature an infinite character, i. e. they are local, the micromorphic continuum theory affords the material points to capture a small but finite space, i. e. it loses its strictly local character.

The following chapter is organised as a straightforward extension of the classical Cauchy continuum theory presented earlier in chapter 2. At the beginning, the kinematics of the micromorphic continuum theory will be reviewed with respect to the physical picture of the theory, the deformation measures and their time derivatives. Afterwards, the particular balance equations will be derived.

4.1 Kinematics

The basic ideas of the so-called micromorphic continuum theory go back to the seminal work of the brothers Cosserat in the early 20th century, cf. [18]. They associated a triad of orthogonal directors to the material point. Thus, the material transformation of the material point comprises, besides the translational degrees of freedom, additional rotational degrees of freedom. In the 1960s, this concept has been generalised to the so-called micromorphic continuum theory by Eringen [32, 33, 34]. The description of the kinematics within this chapter is adopting the system introduced in [35].

4.1.1 Physical picture

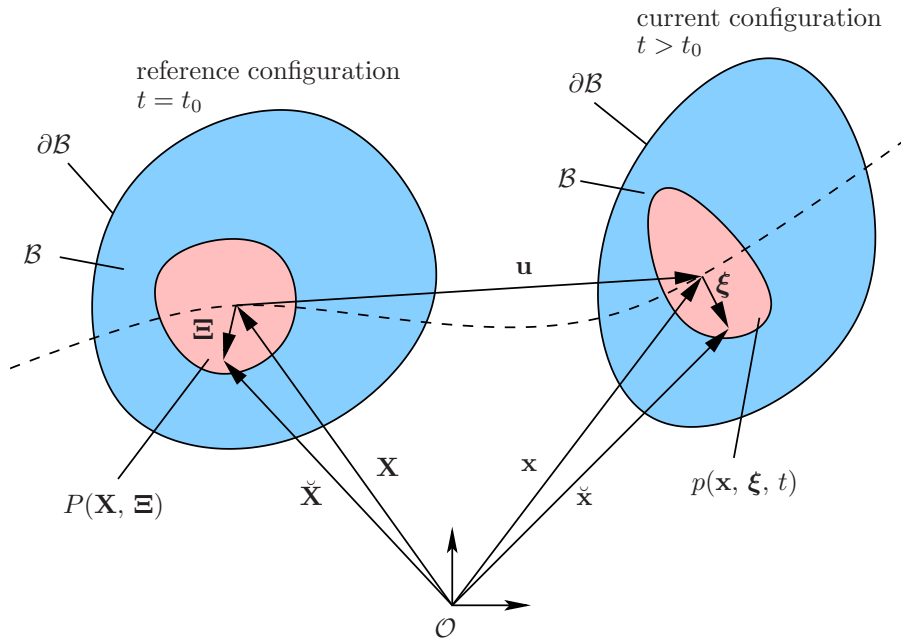


Figure 4.1: The physical picture of the micromorphic continuum: reference and current configuration.

In analogy to the classical continuum theory, the physical body \mathcal{B} , which we are interested in, is consisting of a set of material points. But, as it has been emphasised before, the material points are considered to be deformable

and to capture a small but finite space. This is in contrast to the classical Cauchy theory, where the material points are assumed to be points in the strict mathematical meaning. In order to dissolve the ostensible contradiction of the infinitesimal character of the material point on the one hand and its finite dimension on the other hand, each deformable material point is replaced by a geometrical point P and an attached triad (Ξ_1, Ξ_2, Ξ_3) . This triad represents, in addition to the usual physical properties such as mass density etc., the degrees of freedom arising from the deformation of the material points. Thus, the physical picture of a micromorphic material point may be described via its position vector \mathbf{X} of its volume centroid and by the attached director Ξ , cf. fig. 4.1.

An arbitrary deformation carries the system from the material to the spatial frame and the appropriate mappings may be expressed as

$$\mathbf{x} = \hat{\mathbf{x}}(\mathbf{X}, t) \quad \text{and} \quad \boldsymbol{\xi} = \hat{\boldsymbol{\xi}}(\mathbf{X}, \Xi, t). \quad (4.1)$$

Following Eringen [35], the definition for the micromorphic continuum of grade one reads:

“A material body \mathcal{B} is called a micromorphic continuum of grade one, if its motions are described by

$$\mathbf{x} = \hat{\mathbf{x}}(\mathbf{X}, t) \quad \text{and} \quad \boldsymbol{\xi} = \hat{\boldsymbol{\xi}}(\mathbf{X}, \Xi, t), \quad (4.2)$$

which possess continuous partial derivatives with respect to \mathbf{X} as well as t , and if they are invertible uniquely, i. e.

$$\mathbf{X} = \hat{\mathbf{x}}^{-1}(\mathbf{x}, t) \quad \text{and} \quad \Xi = \hat{\boldsymbol{\xi}}^{-1}(\mathbf{x}, \boldsymbol{\xi}, t) \quad [35]. \quad (4.3)$$

4.1.2 Deformation and strain quantities

Besides the well-known deformation gradient \mathbf{F} , which transports line elements from the material to the spatial frame,

$$d\mathbf{x} = \mathbf{F} \cdot d\mathbf{X}, \quad (4.4)$$

one has to introduce a second transport theorem for the microdeformation. For the case of a micromorphic continuum of grade one, one assumes an affine, i. e. a linear mapping for the microdeformation and one writes

$$\boldsymbol{\xi} = \bar{\boldsymbol{\chi}} \cdot \boldsymbol{\Xi}, \quad (4.5)$$

where $\bar{\boldsymbol{\chi}}$ is called the microdeformation tensor. The transport theorems for surface and volume elements are valid in the common form

$$d\mathbf{a} = (\det \mathbf{F}) \mathbf{F}^{T-1} \cdot d\mathbf{A}, \quad dv = \det \mathbf{F} dV. \quad (4.6)$$

Similar to the polar decomposition of the deformation gradient into a proper orthogonal and a symmetric tensor,

$$\mathbf{F} = \mathbf{R} \cdot \mathbf{U} = \mathbf{V} \cdot \mathbf{R}, \quad (4.7)$$

where

$$\mathbf{R}^T = \mathbf{R}^{-1}, \quad \det \mathbf{R} = +1, \quad \mathbf{U} = \mathbf{U}^T, \quad \mathbf{V} = \mathbf{V}^T, \quad (4.8)$$

one may introduce a polar decomposition of the microdeformation

$$\bar{\boldsymbol{\chi}} = \bar{\mathbf{R}} \cdot \bar{\mathbf{U}} = \bar{\mathbf{V}} \cdot \bar{\mathbf{R}}, \quad (4.9)$$

where

$$\bar{\mathbf{R}}^T = \bar{\mathbf{R}}^{-1}, \quad \det \bar{\mathbf{R}} = +1, \quad \bar{\mathbf{U}} = \bar{\mathbf{U}}^T, \quad \bar{\mathbf{V}} = \bar{\mathbf{V}}^T. \quad (4.10)$$

Subjecting the microdeformation $\bar{\boldsymbol{\chi}}$ to some restrictions allows for the identification of various micromorphic subcontinua.

- The most common restriction is the setting $\bar{\mathbf{U}} = \mathbf{I}$ and $\bar{\boldsymbol{\chi}} = \bar{\mathbf{R}}$. Thus, only rigid body rotations of the material points can be displayed. This case is called the micropolar or Cosserat continuum.
- Suppressing the microrotations, one may restrict the microdeformation to a volumetrically dilatant deformation. One writes $\bar{\mathbf{R}} = \mathbf{I}$ and $\bar{\boldsymbol{\chi}} = \bar{j}\mathbf{I}$ with the scalar microdilatancy \bar{j} . This case is called the microdilatant

continuum.

- Allowing for any symmetric microdeformation, one obtains the microstrain continuum, which is defined via the identities $\bar{\mathbf{R}} = \mathbf{I}$ and $\bar{\boldsymbol{\chi}} = \bar{\boldsymbol{\chi}}^T$.
- Combining the microdilant and the micropolar continuum, one finds the microstretch continuum, where $\bar{\boldsymbol{\chi}} = \bar{j}\bar{\mathbf{R}}$.

A general review of the various subcontinua of the micromorphic theory has been given by Forest et al. in [41].

Again, it is not always convenient to calculate the rotation tensor $\bar{\mathbf{R}}$ and the stretch tensors $\bar{\mathbf{U}}$ and $\bar{\mathbf{V}}$. Thus, one may take into account the position vector, cf. fig. 4.1,

$$\check{\mathbf{x}} = \mathbf{x}(\mathbf{X}, t) + \boldsymbol{\xi}(\mathbf{X}, \boldsymbol{\Xi}, t) \quad (4.11)$$

and its arc length

$$d\check{\mathbf{x}} = \mathbf{F} \cdot d\mathbf{X} + \bar{\boldsymbol{\chi}} \cdot d\boldsymbol{\Xi} + \left(\text{GRAD}^{\text{23}} \bar{\boldsymbol{\chi}} \cdot \boldsymbol{\Xi} \right) \cdot d\mathbf{X}. \quad (4.12)$$

The calculation of the square of the arc length is pointing out the necessity of introducing a set of three independent deformation measures. The most simple choice is the set $(\mathbf{F}, \bar{\boldsymbol{\chi}}, \text{GRAD} \bar{\boldsymbol{\chi}})$. These quantities represent in fact a set of two-field quantities which are, in general, not objective. A form-invariant set of deformation measures can be found as

$$\bar{\mathbf{F}} = \bar{\boldsymbol{\chi}}^{-1} \cdot \mathbf{F}, \text{ the microdeformation tensor,} \quad (4.13)$$

$$\bar{\mathbf{C}} = \bar{\boldsymbol{\chi}}^T \cdot \bar{\boldsymbol{\chi}}, \text{ the right Cauchy-Green} \quad (4.14)$$

microdeformation tensor, and

$$\bar{\mathbf{\Gamma}}^{\text{3}} = \bar{\boldsymbol{\chi}}^{-1} \cdot \text{GRAD} \bar{\boldsymbol{\chi}}, \text{ the wryness or curvature tensor.} \quad (4.15)$$

Considering the differences of squares of arc lengths, one furthermore may identify the microstrain tensor

$$\tilde{\mathbf{E}} = \bar{\mathbf{F}} - \mathbf{I} \quad (4.16)$$

and the Green-Lagrange microstrain tensor

$$\bar{\mathbf{E}} = \bar{\mathbf{C}} - \mathbf{I}. \quad (4.17)$$

Note that all deformation and strain measures given above are completely defined as quantities of the reference configuration. The definitions of the appropriate quantities with respect to the current configuration may be found in [35]. The definition of further deformation and strain tensors is possible.

4.1.3 Material time derivatives

Taking into account the time derivatives in the sequel, one may find at first the definition of the velocity gradient analogous to eq. (2.16)

$$(\mathrm{d}\mathbf{x})' = \frac{\mathrm{d}}{\mathrm{d}t}(\mathbf{F} \cdot \mathrm{d}\mathbf{X}) = \mathbf{F}' \cdot \mathrm{d}\mathbf{X} = \mathbf{F}' \cdot \mathbf{F}^{-1} \cdot \mathrm{d}\mathbf{x}, \quad (4.18)$$

with $\mathbf{v} = \mathbf{x}'$ defining the material velocity gradient

$$\mathbf{F}' = \mathrm{GRAD} \mathbf{v} \quad (4.19)$$

and the spatial velocity gradient

$$\mathbf{L} = \mathrm{grad} \mathbf{v} = \mathbf{F}' \cdot \mathbf{F}^{-1}. \quad (4.20)$$

Similarly, calculating the time derivative of the director $\boldsymbol{\xi}$, one finds

$$\boldsymbol{\xi}' = \bar{\boldsymbol{\chi}}' \cdot \boldsymbol{\Xi} = \bar{\boldsymbol{\chi}}' \cdot \bar{\boldsymbol{\chi}}^{-1} \cdot \boldsymbol{\xi}, \quad (4.21)$$

where the microgyration tensor

$$\bar{\boldsymbol{\nu}} = \bar{\boldsymbol{\chi}}' \cdot \bar{\boldsymbol{\chi}}^{-1} \quad (4.22)$$

has been introduced as the microscopic counterpart to the spatial velocity gradient.

4.2 Balance equations

After having defined the underlying kinematic quantities, the balance equations for the micromorphic continuum theory have to be determined. Again, the method of virtual power comes into play which has been described in detail in [49] for the micromorphic case. Further comments may be found in [48, 86, 104, 118]. Thus, one assumes the sum of all internal and external forces on the body \mathcal{B} due to a virtual motion to vanish and one writes

$$\delta P_i + \delta P_e = 0. \quad (4.23)$$

Without loss of generality, one assumes for the micromorphic continuum the power of the internal forces to be a linear form of the gradient of the virtual velocity, the virtual microgyration and the gradient of the virtual microgyration,

$$\delta P_i = - \int_{\mathcal{B}} \delta p_i \, dv \quad (4.24)$$

with

$$\delta p_i = \mathbf{T} : \text{grad } \delta \mathbf{v} + (\check{\mathbf{S}} - \mathbf{T}) : \delta \bar{\mathbf{v}} + \check{\mathbf{Q}}^3 : \text{grad } \delta \bar{\mathbf{v}} \quad (4.25)$$

and introducing two second order stress quantities \mathbf{T} and $\check{\mathbf{S}}$ as well as one third order stress quantity $\check{\mathbf{Q}}^3$. Following the principle of virtual power, the power of the internal forces has to be constant if computed in a different frame. That means the power of the internal forces has to be invariant with respect to a superimposed rigid body transformation within the framework of the Euclidean transformations. Thus, $\delta \mathbf{v}$ has to be replaced by the expression $\delta \mathbf{v} + \bar{\mathbf{v}} + \bar{\mathbf{\Omega}} \cdot \mathbf{x}$ and analogously $\delta \bar{\mathbf{v}}$ by $\delta \bar{\mathbf{v}} + \bar{\mathbf{\Omega}}$, where $\bar{\mathbf{v}}$ represents a rigid body translation and $\bar{\mathbf{\Omega}}$ a rigid body rotation, i. e. both are constant within \mathcal{B} and, furthermore, $\bar{\mathbf{\Omega}}$ is orthogonal. Inserting these expressions into eq. (4.25) and evaluating the invariance condition, one finds the identity

$$\delta \bar{p}_i - \delta p_i = \check{\mathbf{S}} : \bar{\mathbf{\Omega}} \stackrel{!}{=} \mathbf{0}. \quad (4.26)$$

For an arbitrary rigid body rotation $\bar{\mathbf{\Omega}}$, considering its orthogonality, this condition is fulfilled for the setting

$$\check{\mathbf{S}}^T = \check{\mathbf{S}}, \quad (4.27)$$

i. e. the stress $\check{\mathbf{S}}$ has to be symmetric in the spatial framework. Thus, the virtual power of the internal forces within the whole body \mathcal{B} reads

$$\begin{aligned} \delta P_i = & - \int_{\mathcal{B}} \left(\mathbf{T} : \text{grad } \delta \mathbf{v} + (\check{\mathbf{S}} - \mathbf{T}) : \delta \bar{\boldsymbol{\nu}} \right. \\ & \left. + \check{\mathbf{Q}}^3 : \text{grad } \delta \bar{\boldsymbol{\nu}} \right) dv. \end{aligned} \quad (4.28)$$

For the virtual power of the external forces, a long range volumic force \mathbf{b} and a volumic double force \mathbf{c} are taken into account as well as the surface traction \mathbf{t} and the double surface traction $\check{\mathbf{q}}$. One writes

$$\begin{aligned} \delta P_e = & \int_{\mathcal{B}} (\rho \mathbf{b} \cdot \delta \mathbf{v} + \rho \mathbf{c} : \delta \bar{\boldsymbol{\nu}}) dv \\ & + \int_{\partial \mathcal{B}} (\mathbf{t} \cdot \delta \mathbf{v} + \check{\mathbf{q}} : \delta \bar{\boldsymbol{\nu}}) \cdot d\mathbf{a}. \end{aligned} \quad (4.29)$$

From the physical point of view, the necessity of introducing, besides the surface traction \mathbf{t} , a double surface traction $\check{\mathbf{q}}$, commonly called the surface couple stress, can be illustrated having regard to fig. 4.2.

The physical body \mathcal{B} is consisting of a set of small but finite material points. A detail of its boundary is given on the left-hand side of fig. 4.2. We find the microscopical surface stresses $\mathbf{t}_m^{(i)}$ fluctuating within the material points. Nevertheless, the macroscopic continuum requires stress quantities, which are homogenised over the material point, i. e. which are constant for every particular macroscopic point. In fig. 4.2, the material points are denoted with the index j . If one interprets the material points as deformable particles, it is essential to define the surface traction \mathbf{t}^j as the resultant stress of the microscopic surface tractions within the material point j . Analogously, the double surface traction $\check{\mathbf{q}}^j$ can be understood as the first resultant moment of the microscopic surface stresses, cf. [30, 56].

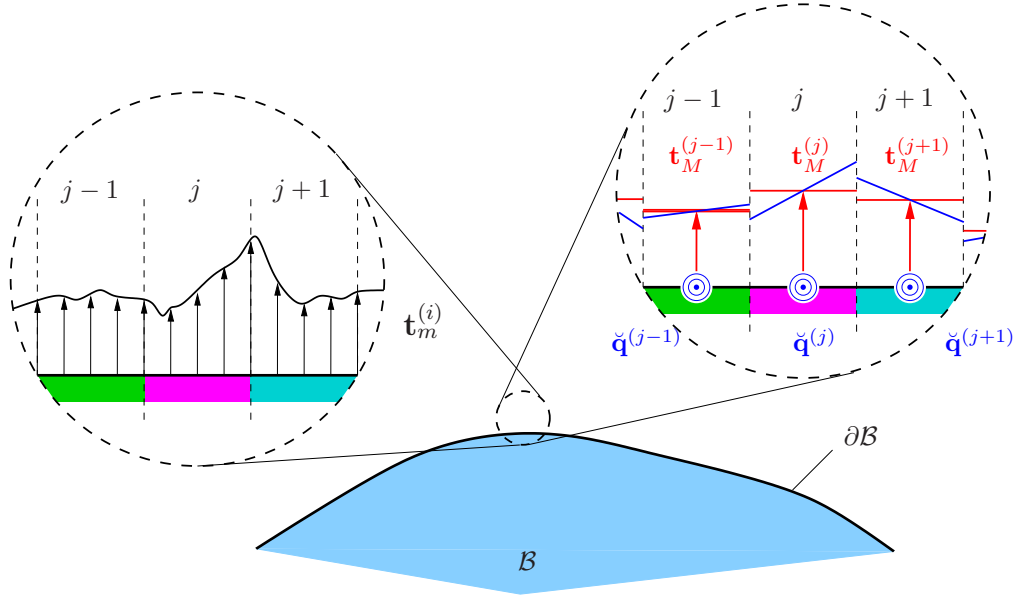


Figure 4.2: Geometrical interpretation of the surface tractions \mathbf{t}^j and the double surface tractions $\check{\mathbf{q}}^j$, where j denotes the particular material point.

After integration by parts and after the application of the divergence theorem, one obtains

$$\begin{aligned} & \int_{\mathcal{B}} \left(\delta \mathbf{v} \cdot (\operatorname{div} \mathbf{T} + \rho \mathbf{b}) + \delta \bar{\nu} : (\operatorname{div} \check{\mathbf{Q}}^3 + \mathbf{T} - \check{\mathbf{S}} + \rho \mathbf{c}) \right) dv \\ & + \int_{\partial \mathcal{B}} \left(\delta \mathbf{v} \cdot (\mathbf{t} - \mathbf{T} \cdot \mathbf{n}) + \delta \bar{\nu} : (\check{\mathbf{q}} - \check{\mathbf{Q}}^3 \cdot \mathbf{n}) \right) da = 0. \end{aligned} \quad (4.30)$$

In the case of equilibrium, the identity (4.30) must hold for any virtual motion $(\delta \mathbf{v}, \delta \bar{\nu})$ and for any subset of \mathcal{B} . Thus, one may identify the local form of the **balance of momentum**

$$\operatorname{div} \mathbf{T} + \rho \mathbf{b} = \mathbf{0} \quad (4.31)$$

and that one of the **balance of moment of momentum**

$$\operatorname{div} \check{\mathbf{Q}}^3 + \mathbf{T} - \check{\mathbf{S}} + \rho \mathbf{c} = \mathbf{0}, \quad (4.32)$$

both formulated in the spatial frame. In the latter, the stress quantities are called

$$\begin{aligned} \mathbf{T}, & \quad \text{the Cauchy stress tensor,} \\ \check{\mathbf{S}}, & \quad \text{the Cauchy-type hyper stress tensor and} \\ \check{\mathbf{Q}}^{\mathfrak{z}}, & \quad \text{the Cauchy-type couple stress tensor.} \end{aligned}$$

Note that, in general, the choice $\mathbf{T} \neq \mathbf{T}^T$ is possible. Furthermore, one finds the coupling between the stresses and the surface tractions,

$$\mathbf{t} = \mathbf{T} \cdot \mathbf{n}, \quad \check{\mathbf{q}} = \check{\mathbf{Q}}^{\mathfrak{z}} \cdot \mathbf{n}, \quad (4.33)$$

both valid on $\partial\mathcal{B}$. Using the transport theorems eqs. (4.4) – (4.6), one finds the appropriate balance equations in the material description. The **balance of momentum** then reads

$$\text{Div } \mathbf{P} + \rho \mathbf{b} = \mathbf{0} \quad (4.34)$$

and the **balance of moment of momentum**

$$\text{Div } \mathbf{Q}^{\mathfrak{z}} + (\mathbf{P} - \mathbf{S}) \cdot \mathbf{F}^T + \rho_0 \mathbf{c} = \mathbf{0}. \quad (4.35)$$

For that purpose, the 1st Piola-Kirchhoff stress tensor

$$\mathbf{P} = (\det \mathbf{F}) \mathbf{T} \cdot \mathbf{F}^{T-1}, \quad (4.36)$$

the appropriate form of the second order hyper stress tensor

$$\mathbf{S} = (\det \mathbf{F}) \check{\mathbf{S}} \cdot \mathbf{F}^{T-1} \quad (4.37)$$

and of the couple stress tensor

$$\mathbf{Q}^{\mathfrak{z}} = (\det \mathbf{F}) \check{\mathbf{Q}}^{\mathfrak{z}} \cdot \mathbf{F}^{T-1} \quad (4.38)$$

have been introduced. In analogy to the 1st Piola-Kirchhoff stress tensor \mathbf{P} , the material form of the hyper stress tensor \mathbf{S} and of the couple stress tensor $\mathbf{Q}^{\mathfrak{z}}$ are two-field quantities, i. e. the first base system(s) refers to the spatial

frame whereas the last base system refers to the material frame.

If one now considers a system under real deformations, one may balance the change in time of the energy stored within the body \mathcal{B} . Neglecting accelerations and thermal effects, the **balance of the internal energy** in the spatial frame reads

$$\begin{aligned} \frac{d}{dt} \int_{\mathcal{B}} \rho \varepsilon \, dv &= \int_{\mathcal{B}} (\rho \mathbf{b} \cdot \mathbf{v} + \rho \mathbf{c} : \bar{\boldsymbol{\nu}}) \, dv \\ &+ \int_{\partial \mathcal{B}} (\mathbf{t} \cdot \mathbf{v} + \check{\mathbf{q}} : \check{\boldsymbol{\nu}}) \, da. \end{aligned} \quad (4.39)$$

Inserting the balance of momentum eq. (4.31) and the balance of moment of momentum eq. (4.32), applying the divergence theorem and assuming the resulting condition to hold for any subset of \mathcal{B} , one obtains the local form of the balance of internal energy in the spatial frame,

$$\rho \varepsilon' = \mathbf{T} : \text{grad } \mathbf{v} + (\check{\mathbf{S}} - \mathbf{T}) : \bar{\boldsymbol{\nu}} + \check{\mathbf{Q}}^{\mathfrak{z}} : \text{grad } \bar{\boldsymbol{\nu}}. \quad (4.40)$$

By transformation back to the reference configuration and after some further calculations, one finally finds the material form of the balance of internal energy,

$$\rho_0 \varepsilon' = \mathbf{P} : \mathbf{F}' + \bar{\mathbf{S}} : \bar{\boldsymbol{\chi}}' + \bar{\mathbf{Q}}^{\mathfrak{z}} : \text{GRAD } \bar{\boldsymbol{\chi}}', \quad (4.41)$$

where $\mathbf{F}' = \text{GRAD } \mathbf{u}'$ and

$$\bar{\mathbf{S}} = (\mathbf{S} - \mathbf{P}) \cdot \bar{\mathbf{F}}^T \text{ and} \quad (4.42)$$

$$\bar{\mathbf{Q}}^{\mathfrak{z}} = \mathbf{Q}^{\mathfrak{z}} \hat{=} (\bar{\boldsymbol{\chi}}^{T-1}, \mathbf{I}). \quad (4.43)$$

For the sake of completeness, one should state that, similar to the Cauchy continuum theory, there exists a further balance law concerning the conservation of mass. But, due to the finite dimension of the material point, its microinertia has to be balanced separately. Finally, the set of balance laws may be completed introducing the entropy principle.

In the latter, the present work will focus on static analyses within an elastic regime. Thus, no inertia or entropic effects will be taken into account. These additional balances are discussed in detail in the literature, e. g. [35, 49].

5

Homogenisation of micromorphic media

After having reviewed the fundamental concept of the micromorphic continuum theory, it is the aim of the following chapter to derive a two-scale approach analogous to that one presented in chapter 3. Thus, one has to identify appropriate homogenisation rules to replace a heterogeneous Cauchy microcontinuum, representing e. g. the underlying cellular network, by a homogeneous micromorphic macrocontinuum, involving the information of the inherent microscopic length scale. The scheme to be applied in the present chapter has been initially proposed by Forest et al. [39, 45] for a micropolar macrocontinuum and has been later on worked out in detail for the more general case of the micromorphic macrocontinuum [40, 68, 69, 71]. In the latter, the described methodology will be subject to a further enhancement which allows for a unique geometrical interpretation of the extended degrees of freedom.

5.1 Averaging theorems

The basic idea of the approach introduced in the sequel can be understood as a straightforward extension of the first order methodology presented in chapter 3. The kinematic quantities of the micromorphic macrocontinuum, i. e. the displacement field and the deformation quantities introduced earlier, have to be expressed in terms of a polynomial mean field and a periodic fluctuation of the heterogeneous Cauchy microvolume attached to the micromorphic material point. To simplify matters, the methodology will be formulated for the two-dimensional case. The attached microvolume is assumed to be a rectangular unit cell with the edge lengths a and b , capturing the microscopic body \mathcal{B}_m with the volume $V_m = ab$. Let \mathbf{X}_M denote the volume centroid of \mathcal{B}_m , cf. fig. 3.2. Again, quantities depicted with $\langle \diamond \rangle_m$ refer to the microscale whereas quantities depicted with $\langle \diamond \rangle_M$ refer to the macroscale.

At first, let us investigate the relations between the microscopic and the macroscopic displacement fields. Following [45, 71], one may postulate the kinematic set $(\mathbf{u}_M, \bar{\boldsymbol{\chi}}_M)$ to characterise the macrostate that best fits the microscopic displacement field \mathbf{u}_m in the average over the microvolume V_m . Whereas the microscopic displacement field of the heterogeneous microcontinuum is uniquely represented by \mathbf{u}_m , the macroscopic displacement field has to take into account the material points to be of small but finite extent. Following the argumentation of Germain [49], it is a natural choice to apply a Taylor series extension of the macroscopic displacement field with respect to $\Delta \mathbf{X}$ and, due to the small extent, to stop this expansion with the terms of degree one. Consequently, the effective displacement field reads $\mathbf{u}_M + (\bar{\boldsymbol{\chi}}_M - \mathbf{I}) \cdot \Delta \mathbf{X}$. Introducing the quadratic functional

$$\mathcal{F}(\mathbf{u}_M, \bar{\boldsymbol{\chi}}_M) = \langle (\mathbf{u}_m - \mathbf{u}_M - (\bar{\boldsymbol{\chi}}_M - \mathbf{I}) \cdot \Delta \mathbf{X})^2 \rangle. \quad (5.1)$$

and minimising \mathcal{F} , one calculates

$$d\mathcal{F} = \frac{\partial \mathcal{F}}{\partial \mathbf{u}_M} \cdot d\mathbf{u}_M + \frac{\partial \mathcal{F}}{\partial \bar{\boldsymbol{\chi}}_M} : d\bar{\boldsymbol{\chi}}_M \stackrel{!}{=} 0. \quad (5.2)$$

This condition is fulfilled for the (restrictive) choice

$$\frac{\partial \mathcal{F}}{\partial \mathbf{u}_M} \stackrel{!}{=} \mathbf{0} \quad \text{and} \quad \frac{\partial \mathcal{F}}{\partial \bar{\chi}_M} \stackrel{!}{=} \mathbf{0}. \quad (5.3)$$

After some calculations, one obtains

$$\mathbf{u}_M = \langle \mathbf{u}_m \rangle \Leftrightarrow \langle \Delta \mathbf{u} \rangle = \mathbf{0} \quad \text{and} \quad (5.4)$$

$$\bar{\chi}_M - \mathbf{I} = \langle \Delta \mathbf{u} \otimes \Delta \mathbf{X} \rangle \cdot \mathbf{G}^{-1}, \quad (5.5)$$

where $\Delta \mathbf{u} = \mathbf{u}_m - \mathbf{u}_M$. The second order geometry tensor $\mathbf{G} = \langle \Delta \mathbf{X} \otimes \Delta \mathbf{X} \rangle$ only depends on the microvolume's shape. For the rectangular case, the coefficient scheme of \mathbf{G} in the orthonormal base system reads

$$G_{ij} \hat{=} \frac{1}{12} \begin{bmatrix} a^2 & 0 \\ 0 & b^2 \end{bmatrix}. \quad (5.6)$$

Eq. (5.4) corresponds to eq. (3.4) of the first order scheme. Thus, taking into account the microdeformation to equal the identity, the averaging procedure is downwards compatible. Again, the short wave length fluctuations of the microscale have to vanish in the average over the microvolume and therefore they are not visible on the effective, i. e. the macroscopic level. By contrast, the microdeformation is representing the first moment of the microdisplacements in the volume average.

By further calculations, one may find the volume averages for the gradient quantities by

$$\text{GRAD } \mathbf{u}_M = \langle \text{GRAD } \mathbf{u}_m \rangle \quad \text{and} \quad (5.7)$$

$$\text{GRAD } \bar{\chi}_M = \langle \text{GRAD } (\Delta \mathbf{u} \otimes \Delta \mathbf{X}) \rangle \hat{:} (\mathbf{G}^{-1}, \mathbf{I}). \quad (5.8)$$

5.2 Microscopic deformation modes

After having derived the averaging relations between the kinematic quantities of the micro- and the macroscale, the projection rule comes into play. For

that purpose, one may assume the microscopic displacement field to be a polynomial of grade three,

$$\begin{aligned} \Delta \mathbf{u} &= \mathbf{A}_M^1(\mathbf{X}_M, t) + \mathbf{B}_M^2(\mathbf{X}_M, t) \cdot \Delta \mathbf{X} + \frac{1}{2} \mathbf{C}_M^3(\mathbf{X}_M, t) : (\Delta \mathbf{X} \otimes \Delta \mathbf{X}) \\ &\quad + \frac{1}{6} \mathbf{D}_M^4(\mathbf{X}_M, t) : (\Delta \mathbf{X} \otimes \Delta \mathbf{X} \otimes \Delta \mathbf{X}) + \Delta \tilde{\mathbf{u}}. \end{aligned} \quad (5.9)$$

The coefficient tensors \mathbf{A}_M^1 , \mathbf{B}_M^2 , \mathbf{C}_M^3 and \mathbf{D}_M^4 depend on the macroscopic position vector \mathbf{X}_M and the current time t . Hence, these quantities are constant within the attached microvolume. By assumption, the cubic polynomial link is not complete but contains only the periodic deformation modes, i. e. the higher order forms of the linear deformation modes. This is in contrast to Forest et al. [45], where the cubic polynomial link has assumed to be complete. This second choice will be discussed in the appendix A.

Written in coefficients, the cubic link reads

$$\Delta u_1^{\text{cub}} = \frac{1}{6} (D_{M1111} \Delta X_1^3 + D_{M1222} \Delta X_2^3), \quad (5.10)$$

$$\Delta u_2^{\text{cub}} = \frac{1}{6} (D_{M2111} \Delta X_1^3 + D_{M2222} \Delta X_2^3). \quad (5.11)$$

The additional displacements $\Delta \tilde{\mathbf{u}}$ represent a higher order fluctuation field due to the microstructural periodicity. In this context, the term *higher order fluctuations* means that they have to be of a order higher than the cubic one.

Following the procedure of [45], let us now compute \mathbf{u}_M , $\bar{\boldsymbol{\chi}}_M$ and their gradients inserting the polynomial ansatz function eq. (5.9) into eqs. (5.4) – (5.8). Doing so, it is vice versa possible to find the coefficient tensors of the ansatz polynomial in terms of the macroscopic quantities by backwards identification:

$$\mathbf{A}_M^1 = -\frac{1}{2} \text{GRAD } \bar{\boldsymbol{\chi}}_M : \mathbf{G}, \quad (5.12)$$

$$\mathbf{B}_M^2 = \frac{1}{2} (5 (\bar{\boldsymbol{\chi}}_M - \mathbf{I}) - 3 \text{GRAD } \mathbf{u}_M), \quad (5.13)$$

$$\mathbf{C}_M^3 = \text{GRAD } \bar{\boldsymbol{\chi}}_M, \quad (5.14)$$

$$\mathbf{D}_M^4 = -5 ((\bar{\boldsymbol{\chi}}_M - \mathbf{I}) - \text{GRAD } \mathbf{u}_M) \cdot \mathbf{I} \cdot \mathbf{G}^{-1}. \quad (5.15)$$

Note the clear distinction between deformation modes of odd and even order. Whilst the constant and the quadratic coefficient tensors depend on the gradient of the microdeformation only, the linear and the cubic ones depend on the displacement gradient and the microdeformation. Eq. (5.12) describes the rigid body translation of the volume centroid. Obviously, the quadratic deformation modes, depending on the gradient of the microdeformation, move the volume centroid. But this motion would be in contradiction to eq. (5.4). Hence, the constant part of the projection polynomial eliminates the translation of the volume centroid.

Having regard to the odd polynomial links, it is remarkable the linear as well as the cubic deformation modes to scale with both, the displacement gradient *AND* the microdeformation. Due to the higher order character of the polynomial ansatz function eq. (5.9), the downwards compatibility to the first order choice eq. (3.9) is not obvious but it is ensured via the averaging rules eqs. (5.4) and (3.4).

Finally, the complete projection rule reads

$$\begin{aligned} \Delta \mathbf{u} = & \frac{1}{2} \left(-\text{GRAD } \bar{\chi}_M : \mathbf{G} + (5(\bar{\chi}_M - \mathbf{I}) - 3 \text{GRAD } \mathbf{u}_M) \cdot \Delta \mathbf{X} \right. \\ & \left. + \text{GRAD } \bar{\chi}_M : (\Delta \mathbf{X} \otimes \Delta \mathbf{X}) \right) \\ & - \frac{5}{6} \left(((\bar{\chi}_M - \mathbf{I}) - \text{GRAD } \mathbf{u}_M) \cdot \mathbf{I} \cdot \mathbf{G}^{-1} \right) : (\Delta \mathbf{X} \otimes \Delta \mathbf{X} \otimes \Delta \mathbf{X}). \end{aligned} \quad (5.16)$$

The various deformation modes are depicted in figs. 5.1 and 5.2 for a square microvolume. For the sake of a clear arrangement, only the deformation modes in ΔX_1 -direction are plotted. Furthermore, the microcoordinates attached to the constant volume centroid have not been visualised. The black box including the dotted lines represents the undeformed state of the microvolume.

Let us concentrate at first on the odd deformation modes depending on $\text{GRAD } \mathbf{u}_M$, cf. fig. 5.1. Compared to the (linear) first order deformation modes, cf. fig. 3.3, the superposition of linear and cubic effects is obvious. But it is important to note that the effective deformation, i. e. the relative motion of the left and the right boundary for the stretch mode or the relative

motion of the top and the bottom boundary for the shear mode, accord to this one of the first order deformation modes. To make this effect apparent, let us insert the given macroscopic shear deformation $u_{M1,2} = \bar{u}$ into the first order projection rule eq. (3.12) for the top boundary, i. e. at the position $\Delta X_2 = b/2$. One obtains

$$\Delta u_1^{1^{\text{st}} \text{ order}} \left(\Delta X_2 = \frac{b}{2} \right) = \bar{u} \frac{b}{2}, \quad (5.17)$$

$$\Delta u_2^{1^{\text{st}} \text{ order}} \left(\Delta X_2 = \frac{b}{2} \right) = 0. \quad (5.18)$$

Inserting the identical macroscopic deformation at the same position into the micromorphic projection rule eq. (5.16), one finds

$$\Delta u_1^{2^{\text{nd}} \text{ order}} \left(\Delta X_2 = \frac{b}{2} \right) = -\frac{3}{2} \bar{u} \frac{b}{2} + \frac{5}{6} \bar{u} \frac{12}{b^2} \frac{b^3}{8} = \bar{u} \frac{b}{2}, \quad (5.19)$$

$$\Delta u_2^{2^{\text{nd}} \text{ order}} \left(\Delta X_2 = \frac{b}{2} \right) = 0. \quad (5.20)$$

Analogously, the same check may be accomplished for the stretching deformation modes. Thus, the consistency of the higher-order projection rule with the first order projection rule can be guaranteed.

By contrast, the deformation modes depending on the microdeformation $\bar{\chi}_M$ do not contribute to any effective deformation state. In fact, they enable the microstructure to exhibit *inner* deformations, cf. fig. 5.1 c) and d). Thus, the microdeformation allows the system to regularise its deformation state providing a set of periodic deformations of grade three. But unlike the usual periodic boundary conditions, the microdeformation, representing a set of independent degrees of freedom within the extended continuum theory, can be controlled systematically, e. g. by the formulation of appropriate boundary conditions for $\bar{\chi}_M$.

Let us now attend to the deformation modes depending on the microdeformation gradient $\text{GRAD } \bar{\chi}_M$. Different from all other deformation modes, the size of the microvolume comes into play, on the one hand for the rigid body motion via the geometry tensor \mathbf{G} and on the other hand for the quadratic polynomial link via the expression $\Delta \mathbf{X} \otimes \Delta \mathbf{X}$, cf. eq. (5.16). Consequently both, the constant as well as the quadratic polynomial link, are of the order

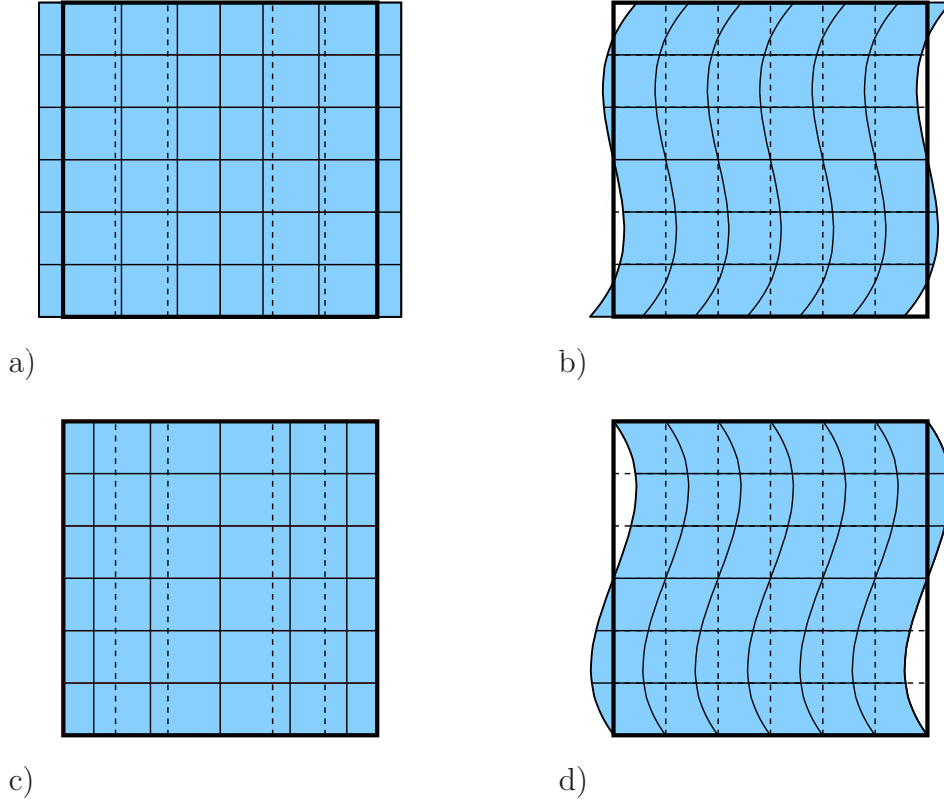


Figure 5.1: The odd deformation modes for the extended FE^2 approach, depending on a) u_{M11} , b) u_{M12} , c) $\bar{\chi}_{M11} - 1$ and d) $\bar{\chi}_{M12}$ for a quadratic microvolume.

$\mathcal{O}(a^2)$, $\mathcal{O}(ab)$ or $\mathcal{O}(b^2)$, respectively. This is in contrast to the cubic polynomial link, where the inverse of the geometry tensor \mathbf{G}^{-1} normalises the microdisplacement and in contrast to the linear polynomial link, both of the order $\mathcal{O}(a)$ or $\mathcal{O}(b)$, respectively. From the physical point of view, this size sensibility indicates the quadratic deformation modes to describe bending effects. This interpretation will be investigated in detail later on. In fig. 5.2, the different deformation modes depending on $\text{GRAD } \bar{\chi}_M$ are depicted. Apparently, the rigid body displacement is adjusting the shifting of the volume centroid. Thus, it remains fix during the deformation.¹

At the end of this section, let us conclude with a brief review over the found

¹This correction of the rigid body translation may be neglected within a quasi-static regime without inertia effects.

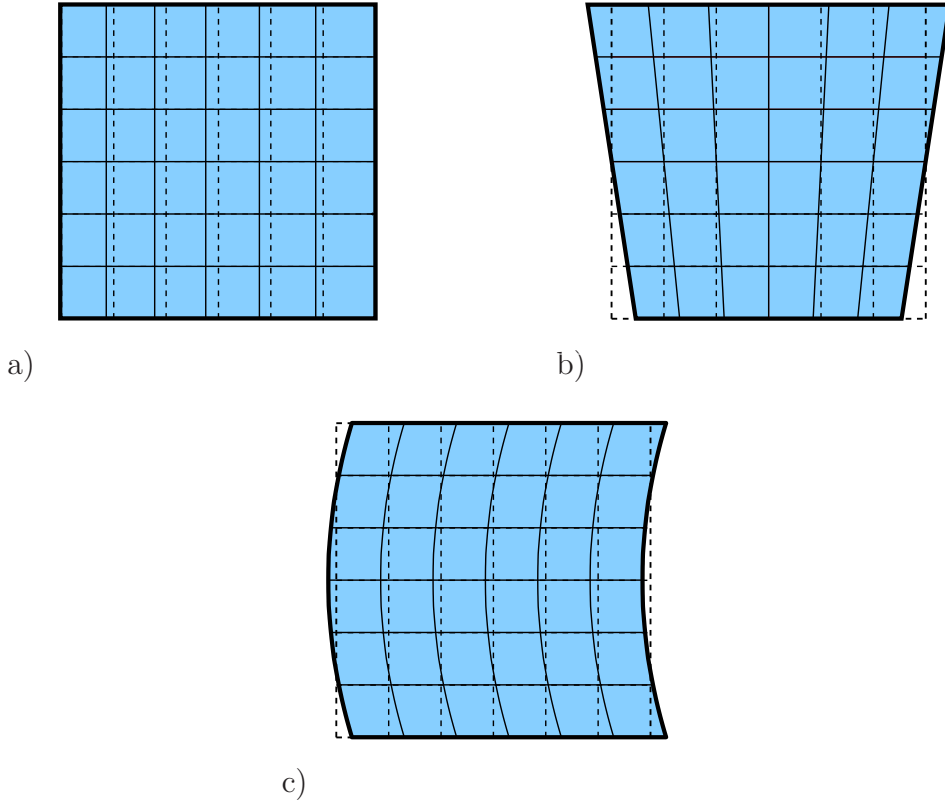


Figure 5.2: The even deformation modes for the extended FE^2 approach, depending on a) $\bar{\chi}_{M11,1}$, b) $\bar{\chi}_{M12,1}$, c) $\bar{\chi}_{M12,2}$ for a quadratic microvolume.

results and interpretations. Firstly, by derivation and evaluation of appropriate averaging theorems, the consistency and the backward compatibility of the method have been demonstrated. Secondly, it has been determined a clear geometrical interpretation for the higher order degrees of freedom. Whereas the microdeformation gradient has been assigned to describe bending effects on the microscale, the microdeformation itself regularises the microstructure's deformation independently from the macroscopic displacement gradient. Consequently, within a macroscopic experiment, one may expect the microdeformation gradient to dominate the regions close to boundaries of the macroscopic sample restricted by appropriate boundary conditions, whereas the microdeformation is supposed to emerge in the volume of the sample, i. e. in more or less homogeneous regions with smoothly varying deformation fields.

5.3 Extension of the Hill-Mandel condition

Proceeding in the algorithm applied in chapter 3, one now has to motivate homogenisation rules for the stress quantities applying an extended form of the Hill-Mandel condition. Assuming static and isothermal conditions, the Hill-Mandel condition for a homogeneous micromorphic macrocontinuum replacing a heterogeneous Cauchy microcontinuum reads in the material frame

$$\langle \mathbf{P}_m : \text{GRAD } \Delta \mathbf{u}' \rangle = \mathbf{P}_M : \mathbf{F}'_M + \bar{\bar{\mathbf{S}}}_M : \bar{\chi}'_M + \bar{\mathbf{Q}}_M^3 : \text{GRAD } \bar{\chi}'_M, \quad (5.21)$$

making use of the balance of internal energy eq. (4.41). By further transformations, one finds

$$\begin{aligned} \langle \mathbf{P}_m : \text{GRAD } \Delta \mathbf{u}' \rangle &= \bar{\mathbf{P}}_M : \left(\frac{5}{2} \bar{\chi}'_M - \frac{3}{2} \mathbf{F}'_M \right) + \bar{\mathbf{S}}_M : (\bar{\chi}'_M - \mathbf{F}'_M) \\ &\quad + \bar{\mathbf{Q}}_M^3 : \text{GRAD } \bar{\chi}'_M, \end{aligned} \quad (5.22)$$

where

$$\bar{\mathbf{P}}_M = \mathbf{P}_M + \bar{\bar{\mathbf{S}}}_M \quad \text{and} \quad (5.23)$$

$$\bar{\mathbf{S}}_M = -\frac{5}{2} \mathbf{P}_M - \frac{3}{2} \bar{\bar{\mathbf{S}}}_M. \quad (5.24)$$

Calculating now the time derivative of eq. (5.9), one finds the microscopic velocity field to be a function of the time derivatives of the coefficients tensors,

$$\begin{aligned} \Delta \mathbf{u}' &= \left(\mathbf{B}_M^2(\mathbf{X}_M, t) \right)' \cdot \Delta \mathbf{X} + \frac{1}{2} \left(\mathbf{C}_M^3(\mathbf{X}_M, t) \right)' : (\Delta \mathbf{X} \otimes \Delta \mathbf{X}) \\ &\quad + \frac{1}{6} \left(\mathbf{D}_M^4(\mathbf{X}_M, t) \right)' : (\Delta \mathbf{X} \otimes \Delta \mathbf{X} \otimes \Delta \mathbf{X}) + \Delta \tilde{\mathbf{u}}'. \end{aligned} \quad (5.25)$$

In accordance to the transformation eq. (3.14), one may insert eq. (5.25) into eq. (5.22) and one finds

$$\begin{aligned}
\langle \mathbf{P}_m : \text{GRAD } \Delta \mathbf{u}' \rangle &= \frac{1}{V_m} \int_{\partial \mathcal{B}_m} (\mathbf{p}_m \otimes \Delta \mathbf{X}) \, dA : \left(\mathbf{B}_M^2 \right)' \\
&+ \frac{1}{2V_m} \int_{\partial \mathcal{B}_m} (\mathbf{p}_m \otimes \Delta \mathbf{X} \otimes \Delta \mathbf{X}) \, dA : \left(\mathbf{C}_M^3 \right)' \\
&+ \frac{1}{6V_m} \int_{\partial \mathcal{B}_m} (\mathbf{p}_m \otimes \Delta \mathbf{X} \otimes \Delta \mathbf{X} \otimes \Delta \mathbf{X}) \, dA :: \left(\mathbf{D}_M^4 \right)'.
\end{aligned} \tag{5.26}$$

By comparison of coefficients (if $\Delta \tilde{\mathbf{u}}' = \mathbf{0}$), it is possible to identify

$$\bar{\mathbf{P}}_M = \frac{1}{V_m} \int_{\partial \mathcal{B}_m} (\mathbf{p}_m \otimes \Delta \mathbf{X}) \, dA, \tag{5.27}$$

$$\bar{\mathbf{Q}}_M^3 = \frac{1}{2V_m} \int_{\partial \mathcal{B}_m} (\mathbf{p}_m \otimes \Delta \mathbf{X} \otimes \Delta \mathbf{X}) \, dA, \tag{5.28}$$

$$\bar{\mathbf{S}}_M^4 = \frac{1}{6V_m} \int_{\partial \mathcal{B}_m} (\mathbf{p}_m \otimes \Delta \mathbf{X} \otimes \Delta \mathbf{X} \otimes \Delta \mathbf{X}) \, dA. \tag{5.29}$$

For the rectangular microvolume, it can easily be shown the fourth order hyper stress tensor to be reduced to the second order hyperstress tensor via the transformation

$$\bar{\mathbf{S}}_M^2 = -5 \bar{\mathbf{S}}_M^4 : \left(\mathbf{I} \cdot \mathbf{G}^{-1} \right). \tag{5.30}$$

That means that the fourth order hyper stress contributes to the internal energy if and only if it performs the same symmetry condition as its conjugated deformation quantity \mathbf{D}_M^4 . Concerning the higher order periodic fluctuations $\Delta \tilde{\mathbf{u}}$, one has to note that their consistent formulation is much more complex than it is for the first order case. E. g. Kouznetsova et al. have introduced additional constraints which enforce the shape of the boundary to approximate the kinematically fully prescribed boundary in an integral sense, cf. [77, 79]. In the numerical part of the present contribution it will be shown that the equality $\Delta \tilde{\mathbf{u}} = \mathbf{0}$, which actually corresponds exactly to the state of fully prescribed boundary conditions, leads to reasonable results

for the given cellular microstructures. Consequently, higher order periodic fluctuations will not be subject to further considerations within the proposed micromorphic homogenisation approach.

5.4 Discussion of the method

Let us conclude this chapter with a brief discussion of the extended homogenisation methodology. The algorithmic approach has been strictly orientated on that one for the classical theory and has been carefully generalised applying the extended macroscopic continuum theory:

Starting with the assumption to replace a heterogeneous Cauchy microcontinuum, representing the cellular network, by a homogeneous micromorphic macrocontinuum, appropriate averaging theorems for the kinematic quantities have been derived. Afterwards, the kinematic quantities of the macroscale have been identified in terms of a polynomial mean field and a periodic fluctuation of the attached microvolume. Consequently, the extended deformation quantities could be connected to a clear geometrical interpretation. Finally, evaluating the extended form of the Hill-Mandel condition, homogenisation rules for the stress quantities have been derived.

Comparing these theoretical investigations to the first order approach, one should mention the following remarks:

1. The higher order approach deals with a cubic projection polynomial. Consequently, it is a priori less restrictive as the linear one, used by the first order theory.
2. By the polynomial extension, the microdeformation can be interpreted as the cubic order of the periodic fluctuations and therefore offers an intrinsic regularisation of the microstructural deformation field.
3. Beyond these effects, the proposed scheme is sensitive to the microstructural length scale in terms of the quadratic deformation modes depending on the microdeformation gradient. Consequently, it can be expected the method to describe size dependent boundary layer effects.

At the end of these theoretical considerations the question about the soundness of the micromorphic two-scale approach arises. Therefore, the methodology will be subject to various numerical experiments, performed in the second part of the present contribution.



Numerical investigations

Based on the exact knowledge of the extended kinematics of the micromorphic continuum theory and based on the geometric interpretation of the microstructural degrees of freedom, the second part of the present work intends to investigate in detail the properties of the given two-scale methodology by appropriate numerical experiments. In doing so, the subsequent chapters focus on several main issues:

1. The relevance of the higher-order deformation modes.

Does the higher order projection polynomial provide a higher accuracy displaying the real displacement fields within microstructured materials than it does the first order approach accounting only for linear deformation modes? I. e. do the higher order deformation modes bear any relevance for the description of deformation mechanisms observed in reference experiments?

2. The scale transition properties.

How does the scale transition of the microstructural length scale take place? Which are the basic mechanisms?

3. The validation of the extended two-level approach.

For that purpose, numerical reference calculations with microscopical resolution will be presented, i. e. the underlying structure has been discretised including all relevant microtopological details. Does the two-scale methodology yield to reliable results compared to those reference solutions? Which are the limits of the homogenisation technique?

In order to understand on the one hand the underlying micromechanical processes in their complexity and on the other hand the peculiar effects on the effective level, the following investigations are addressed to some of the simplest possible microtopologies. Throughout this work, the numerical experiments are subject to the following, very strong restrictions:

1. Two-dimensionality.
2. Perfect periodicity and regularity.
3. Geometrical as well as material linearity.

The complete FE² methodology, i. e. the macroscale as well as the microscale calculations, have been implemented within the finite element toolbox COMSOL Multiphysics[®]², allowing for the coupling of an optional number of balance equations, their weak forms, respectively, in a very comfortable way. Throughout all numerical investigations, the microscopic material properties are following Hooke's law using the arbitrary chosen Lamé parameters of steel $\lambda = 153.2$ GPa and $\mu = 78.95$ GPa. The arbitrariness of this choice can be easily justified having regard to the following argumentation:

It is evident the effective mechanical behaviour of a microstructured material to be dominated by both, the material properties of the microstructural elements as well as by the microtopology itself, i. e. the geometrical arrangement of the structural elements. The present contribution will focus on the influence of the microtopology.

From the numerical point of view, the microstructural struts have been discretised by triangular volume elements with quartic Lagrange ansatz functions. The identical discretisation has been chosen for the microscale calculations within the FE² scheme as well as for the reference calculations. On the macrolevel, quadrilateral volume elements with quartic Lagrange ansatz functions have been chosen for the discretisation of the displacement field whereas the microdeformations have been discretised with cubic Lagrange ansatz functions. To ensure an appropriate accuracy of the numerical computations, the convergence of the particular discretisations in combination with the chosen order of the ansatz functions has been checked and adapted carefully. Further evaluations concerning the choice of the ansatz functions have not been included in the examples presented in the sequel.

²<http://www.comsol.com>

6

Relevance of the higher order deformation modes

The substitution of a heterogeneous microcontinuum by a micromorphic macrocontinuum requires the additional degrees of freedom, provided by the extended theory, to display the real deformation mechanisms of a particular microstructure in an adequate way. Based on the investigations accomplished in [70], a set of four perfectly periodic microstructures is subject to several numerical experiments with microscopic resolution, whereas the analysed periodic unit cells are depicted in fig. 6.1. The structures are considered as lattices of struts which are rigidly connected in vertices. The interaction between two vertices only depends on the geometry and the material properties of the connecting struts.

Note the analogy to systems consisting of discrete particles interacting via their boundary. Thus, one may interpret the vertices as particles and the given microstructures as n -particle systems, cf. [107], where n describes the number of particles included in the investigated microvolume. Hence, microstructure a) represents an 1-particle system, whereas the microstructures b) and c) involve 2 particles, microstructure d) even 4 particles, respectively.

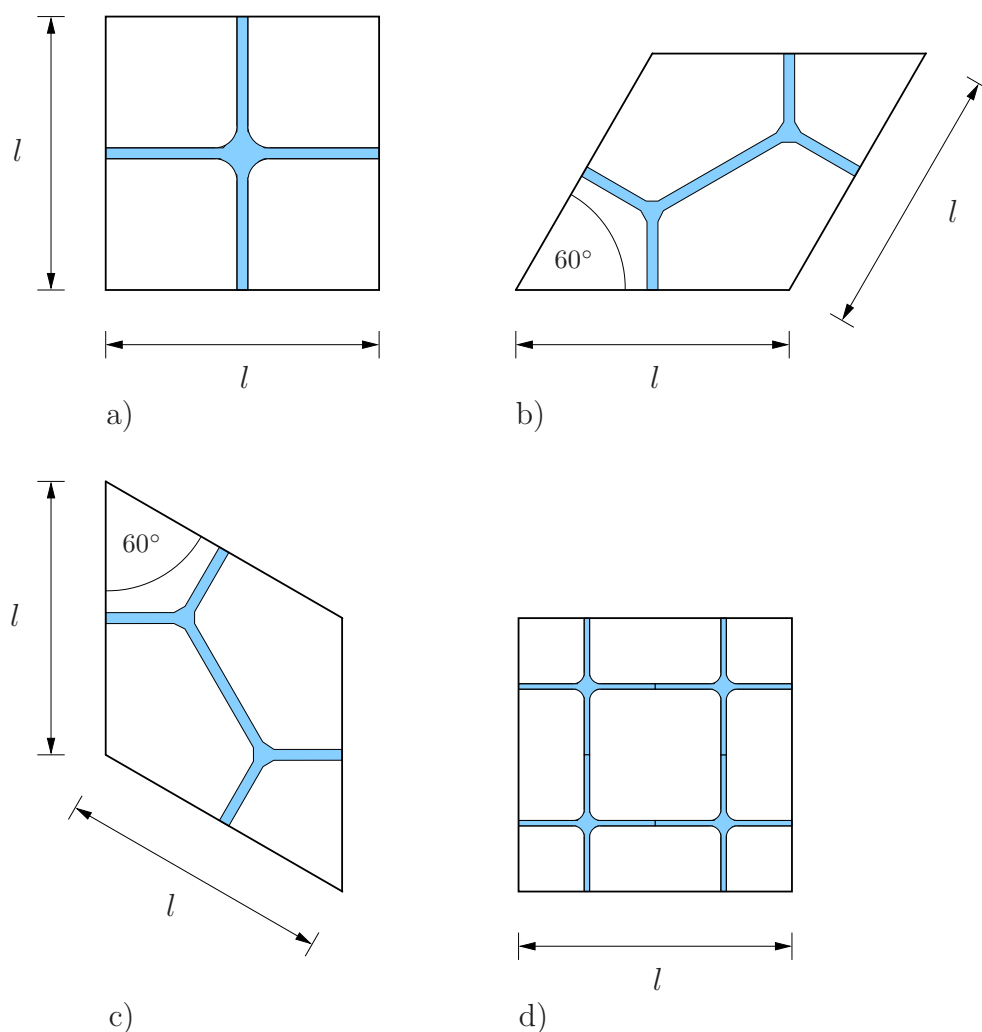


Figure 6.1: The periodic unit cells of the investigated cellular microstructures. The struts feature an aspect ratio $r \approx 1/20$ for a) and d), $r \approx 1/12$ for b) and c), respectively, cf. [70].

The given microstructures have been subject to several numerical experiments, which are depicted in a schematic way for the single-cross microstructure a) in fig. 6.2 and which have been accomplished for the microstructures b) – d) in an analogous way.

The displacement field at the boundary of the mentioned unit cells, embedded in the microscopically resolved cellular structure, is observed at four different positions ① – ④. In order to determine the sensitivity of higher order projection polynomials for the underlying microscopic processes, sev-

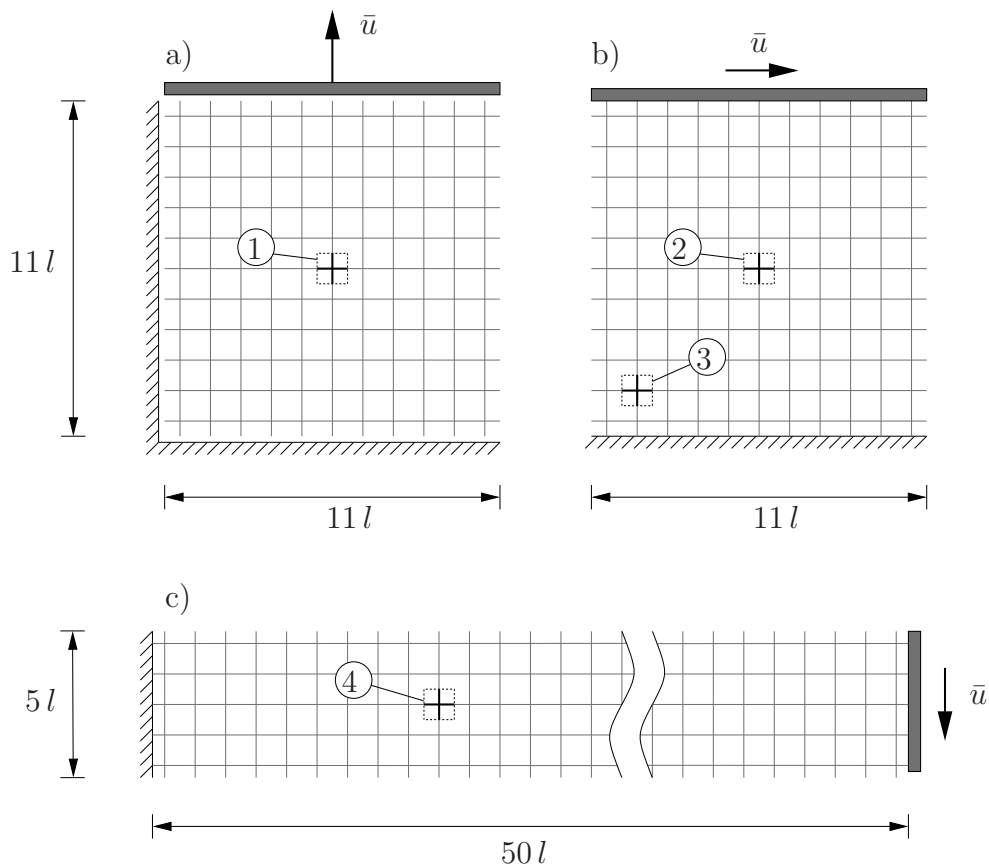


Figure 6.2: Setup of the numerical experiments: a) tension test, b) inhomogeneous shear test, c) three-point bending test, exemplary displayed for microstructure a), microstructures b) – d) analogously. The embedded unit cells subject to the further investigations are denoted with ① – ④, cf. [70].

eral polynomials with increasing order have been fitted to the really observed displacement fields applying the method of least squares. More precisely, the study comprises a linear polynomial, representing the first order projection rule, a quadratic polynomial in analogy to a second order FE² scheme using a second-gradient continuum on the macroscale, e. g. [76, 77], the micromorphic projection polynomial and finally an unrestricted cubic polynomial as well as its quartic and quintic counterparts. Afterwards, the resulting least-error squares have been plotted versus the number of independent deformation modes of the particular polynomial order, where the least-error squares have been normalised with respect to the least-error square of the linear projection polynomial in the particular case, cf. fig. 6.3. The relation between the fitting polynomials and the number of independent deformation

polynomial order	0	1	2	3	4	5	sum
linear	2	3					5
quadratic	2	4	6				12
micromorphic	2	4	6	4			16
cubic	2	4	6	8			20
quartic	2	4	6	8	10		30
quintic	2	4	6	8	10	12	42

Table 6.1: Number of independent deformation modes of the different projection rules depending of their polynomial order.

modes is given in tab. 6.1.

Note that for the fitting procedure, no periodic fluctuations have been taken into account for any projection polynomial. Consequently, the present study only draws a kinematical comparison and does not indicate the absolute accuracy of FE² schemes based on the chosen polynomials.

Considering the results displayed in fig. 6.3, one may assert an increasing exactness in the fitting quality for all microstructures at all investigated positions. But the characteristics of this increase seem strongly to depend on the particular microstructure:

- Let us concentrate at first on the single-cross microstructure fig. 6.1 a). For the more or less homogeneous stretching and shear deformation at position ① and ②, one observes an abrupt error decay of up to six orders of magnitude between the quadratic and the micromorphic polynomials whereas a further increase in the polynomial order keeps the error constant. At position ③ and ④, the decay of the error accounts for about three to four orders of magnitude. But a further increase in polynomial order causes an even higher fitting accuracy.

It is remarkable that, at any investigated position, the quadratic deformation modes do not come into play at all. According to their interpretation as bending modes and supposing the bending effects to be the more dominant the closer to the boundary, cf. e. g. [22], the results indicate that, due to the slender shape of the struts, the bending stiffness of the microstructure is very low. Thus, any bending effect decays within one unit cell and can not be detected at the chosen positions. Further attention should be paid to the high accuracy of the

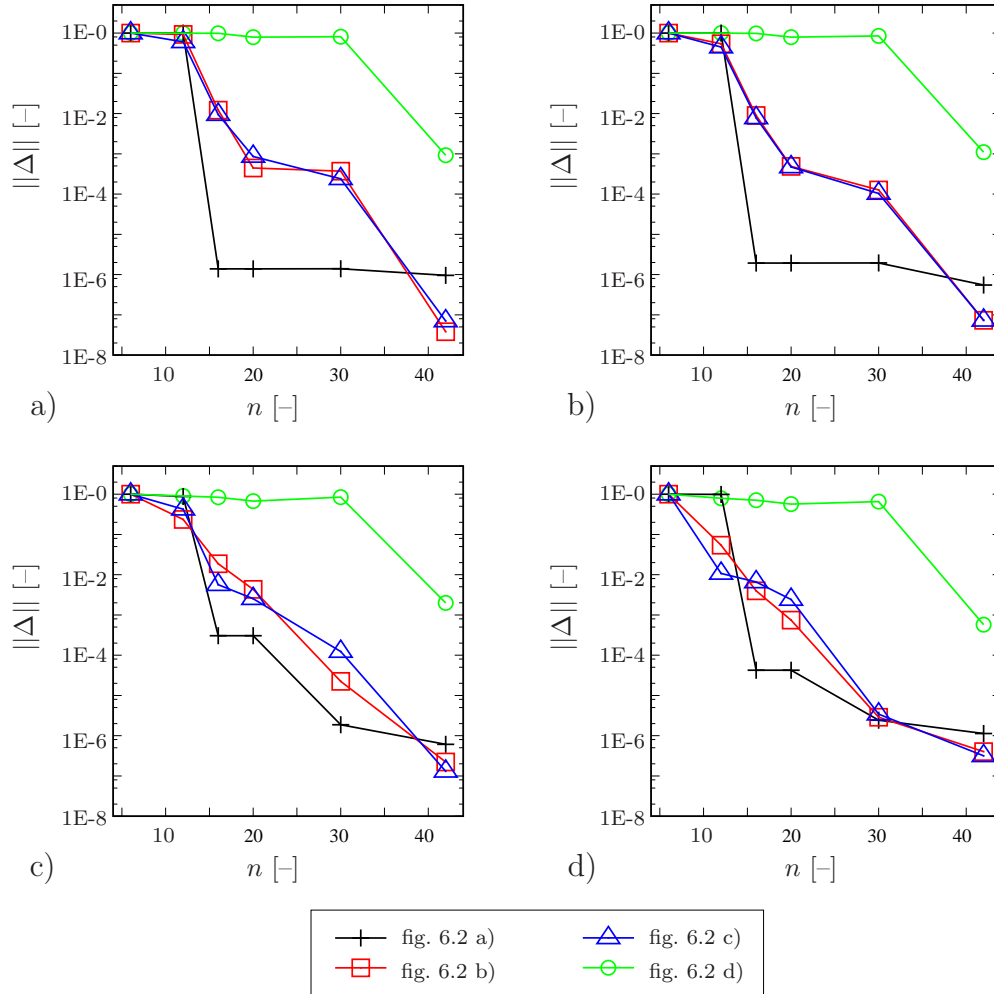


Figure 6.3: Normalised least error square $\|\Delta\|$ for the different fitting polynomials at the positions a) ①, b) ②, c) ③ and d) ④, where n represents the particular number of independent deformation modes.

micromorphic fitting. Having regard to eq. (5.9), only the periodic cubic expansion is included. As the full cubic polynomial does not offer a significantly higher fitting accuracy, this result indicates the cubic modes to describe deformations due to the microstructural periodicity. From the physical point of view, one could interpret the action of the cubic deformation modes as a rotation of the struts at the boundary of the unit cell similar to the Bernoulli hypothesis of planar cross sections. By contrast, having in mind the situation at the positions ③ and ④, the quartic and the quintic deformation modes seem to be activated. But remark again the qualitative character of this first study.

- Secondly, considering the related four-cross microstructure 6.1 d), the results diverge strongly. The increase in the polynomial order from linear to quartic does not bear any significant advantage. Only a further increase to the quintic order causes the normalised least-error square to decay by about three orders of magnitude at all observed positions.

Again, the result may be interpreted making use of the Bernoulli hypothesis. Due to the chosen unit cell involving four vertices, i. e. two connecting struts per boundary, it is not surprising that the cubic polynomial is not able to feature free rotations for each strut. In this case, the quintic polynomial is necessary to meet the same conditions as the Bernoulli hypothesis. Having in mind the bending effects, one may state that, obviously, no bending effects can be detected at the chosen positions due to the low bending stiffness of the basic single-cross unit cell.

- Finally, let us concentrate on the honeycomb unit cells. At first one may state that there is no significant deviation visible between the two different orientations. For both, one observes a more or less continuous decay in the normalised least-error square with increasing polynomial order, similar at all investigated positions.

In contrast to the single-cross microstructure, the micromorphic projection polynomial only reduces the normalised least-error square by about 2 orders of magnitude. Furthermore, the bending effects seem to be more dominant, especially at the rather inhomogeneous positions ③ and ④. Following the common consideration of the honeycomb structure to be the most realistic two-dimensional counterpart of three-dimensional cellular structures, this result may seem somewhat discouraging for the micromorphic projection rule. However, we will see later on in chapter 10 that it is possible to produce reliable results by modifying the choice of the honeycomb unit cell.

Altogether, let us state that the advantage of using the higher order projection rules seem strongly to depend on the underlying microtopology within the investigated unit cell. In order to return to the analogy of vertices and particles, the present study indicates that for $(n > 1)$ -particle systems, the microstructural degrees of freedom within the micromorphic continuum theory lose their physical meaning. Similar conclusions have been drawn by [107, 119] identifying an effective Cosserat medium. Nevertheless, the micromorphic kinematics is able to reproduce the periodic 1-particle microstructures in a rather exact way, i. e. the deformation modes activated by the

extended projection rule seem to cover all essential deformation mechanisms of this particular microstructure.

Remark again that all results within this study have taken into account only the pure projection polynomials excluding any additional periodic fluctuations. In contrast to the linear and the quadratic polynomials, the micro-morphic as well as the cubic ones involve a priori the cubic order periodicity. Consequently, one may conclude that for large sample sizes, i. e. perturbances close to the macroscopic boundary can be neglected, even the first order FE² method and its linear projection rule should be able to predict the characteristic deformation mechanisms within the real microstructure, if enriched by periodic boundary conditions on the microscale or if the micro-volume is chosen large enough. Concerning this correlation, a huge amount of publications exists in literature.

At the end of this chapter, one may outline this first study to confirm the interpretation of the microdeformation $\bar{\chi}_M$ as the cubic periodic fluctuation which is able to regularise the microscopic deformation field. But, due to the particular choice of the examined positions ① – ④, this study is not able to predict the relevance of the bending modes, i. e. the even deformation modes. For that purpose, the following chapter focuses on the transition of the microscopical length scale to the macrolevel.

Finally, this study, comparing the exactness of the higher-order deformation field relative to the linear one, does not allow for a quantitative estimate of the exactness of a comparable FE² calculation. Thus, the question for the definite quality of the introduced two-scale algorithm arises and if it does match the reference calculations.

The subsequent chapters will try to answer those questions.

7

Scale-transition by the higher order deformation modes

The second study within the present work is up to the transition of the microscopic length scale to the macroscale. As it has already been emphasised in chapter 5, the cubic expansion of the projection rule eq. (5.16) may be interpreted as a prescribed periodic fluctuation, regularising the microscopic deformation field. Furthermore, it has been supposed the quadratic deformation modes to be sensitive for the size of the microscopic volume element.

In the sequel, the influence of the microstructural length scale on the effective material behaviour will be investigated in detail. Similar investigations can be found in literature, cf. [71, 74, 76, 84].

For that purpose, the strain energy density induced by the various deformation modes will be examined in dependence of the size l of an attached square microvolume, i. e. the left hand side of the Hill-Mandel condition eq. (5.21) has to be calculated and one writes

$$\langle \mathbf{P}_m : \text{GRAD } \Delta \mathbf{u} \rangle = E. \quad (7.1)$$

The underlying microstructures are depicted in fig. 7.1, a) a cellular and b) a homogeneous one comprising a circular hole. For both unit cells, the edge length l has been varied over several decades.

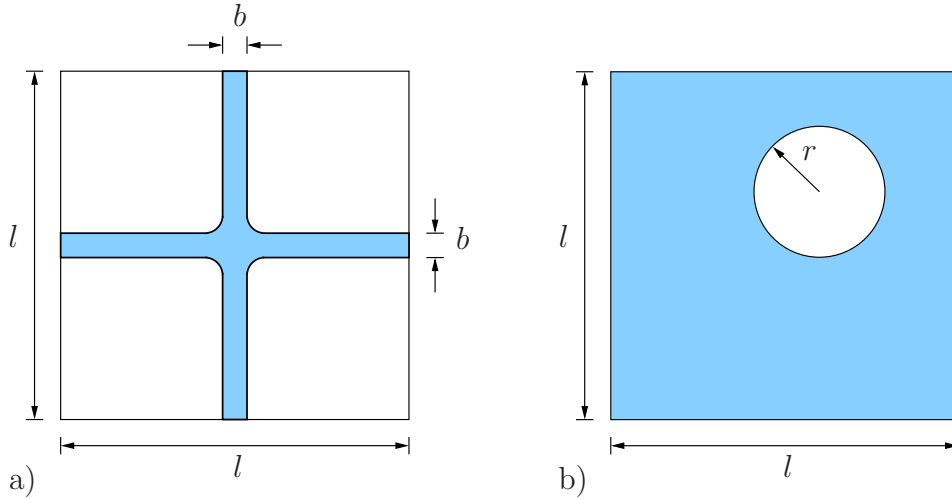


Figure 7.1: The underlying square microvolumina with the variable edge length l , a) a cellular microstructure whereas, $b/l = 1/15$, b) a homogeneous microstructure with an embedded hole, $r/l = 1/5$.

It has emerged that, for any deformation mode, the principle characteristics of the particular strain energy density are strictly independent from the underlying microtopology. Thus, the cellular unit cell as well as the continuous one feature the same relation between the strain energy density and the size of the microvolume l . The results of this study are depicted in fig. 7.2.

On the left hand side of fig 7.2, one finds the schematic relation between the strain energy density and the microlength for the odd deformation modes depending on $\text{GRAD } \mathbf{u}_M$ and $\bar{\chi}_M$. Apparently, the strain energy density E/l^2 is constant for all investigated values of l . Thus, these deformation modes are not sensitive for the size of the microvolume, a change in the microvolume size leads to a proportional change of the internal energy stored within the microvolume. This property is characteristic for first order approaches.

By contrast, the even deformation modes depending on the microdeformation gradient $\text{GRAD } \bar{\chi}_M$ bring the size of the microvolume to the fore. On the right hand side of fig. 7.2, the strain energy density scales with $1/l^2$. This is exactly the point where the transition of the microscopic length scale to the macrolevel comes into play. Due to bending effects, a very large microstructure stores disproportionately more of strain energy than a small one

does. In consequence, the stimulation of the particular quadratic deformation modes is not convenient from the energetic point of view, if the microvolume is chosen too large. Hence, balancing the system and minimising the strain energy within the system, the microdeformation gradient, i. e. the curvature, governing the bending modes, will be adequately small. In the limiting case of an infinitely large microvolume, the solution is free of curvature. However, if the attached microvolume is chosen adequately small, the microscopic and the macroscopic length scales may become comparable to each other. This comparability is the precondition for size depending higher order effects such as boundary layer effects.

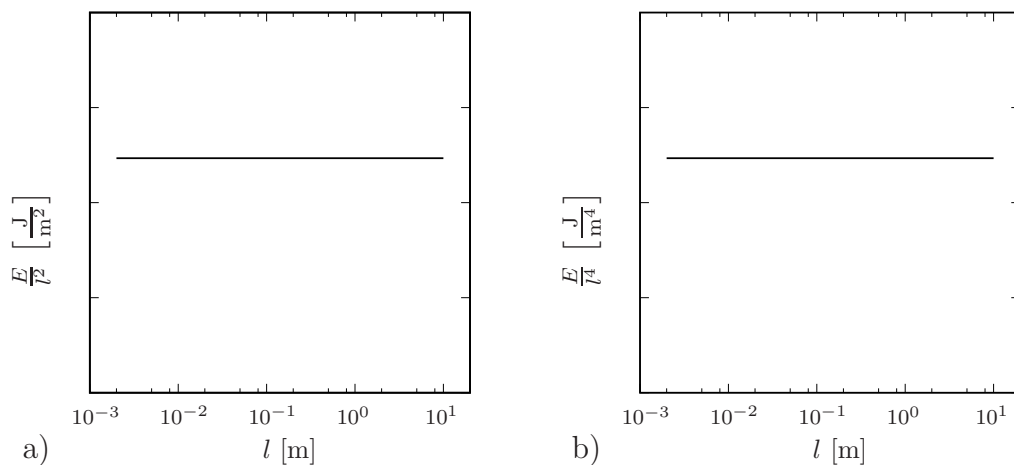


Figure 7.2: The schematic dependence of the strain energy density E/l^2 stored in the attached microvolume of the size l^2 and induced by a) the components of the displacement gradient $\text{GRAD } \mathbf{u}_M$ as well as of the microdeformation $\bar{\chi}_M$ or by b) the microdeformation gradient $\text{GRAD } \bar{\chi}_M$.

Furthermore, this correlation clarifies the question how the characteristic microlength is defined. Within the context of a FE^2 methodology, the microstructural length scale is uniquely defined by the size of the attached volume element. For the single-cross microstructure, the size l of the microvolume equals the length of the connecting struts. Apparently, the interpretation is sound. If one assumes however the four-cross microvolume, cf. fig. 6.1 d), or even a larger unit cell, the interpretation of the microvolume size l as the characteristic length scale is losing its physical meaning. Consequently, we have met a further indication for the necessity of formulating 1-particle microvolumina, if we want to find a geometrical interpretation of the micromorphic kinematics.

A priori, this characteristic transition of length scales depending on curva-

ture quantities cannot be performed by first order approaches and therefore requires the application of an appropriate extended methodology.

Note that for the present study, the size of the microvolume has been varied whilst the absolute number of unit cells within the macroscopic sample has been kept constant. Analogously, it is possible to perform an alternative size effect analysis keeping the size of the microvolume constant but varying the number of unit cells included in the investigated microvolume. An according study has been carried out e. g. in [68] and leads to the identical conclusions.

8

Single-cross microstructures

After having verified the relevance of the higher order deformation modes and their scale transition properties in a qualitative way, the following chapters will apply the extended two-scale technique for several different microstructures. Whereas the material behaviour predicted by the methodology will be characterised carefully, the results will be evaluated in comparison to appropriate reference computations with microscopic resolution.

8.1 Microtopology

Let us start our studies with the most simple case of the perfectly regular and periodic single-cross microstructure, which has already been used earlier. In fig. 8.1, three different unit cells are depicted, which differ in the aspect ratio of the particular microstructural struts, i. e. the quotient of the thickness and the length of the struts. From microstructure fig. 8.1 a) to c), the aspect ratio increases from $1/15$ to $1/10$ and $1/5$.

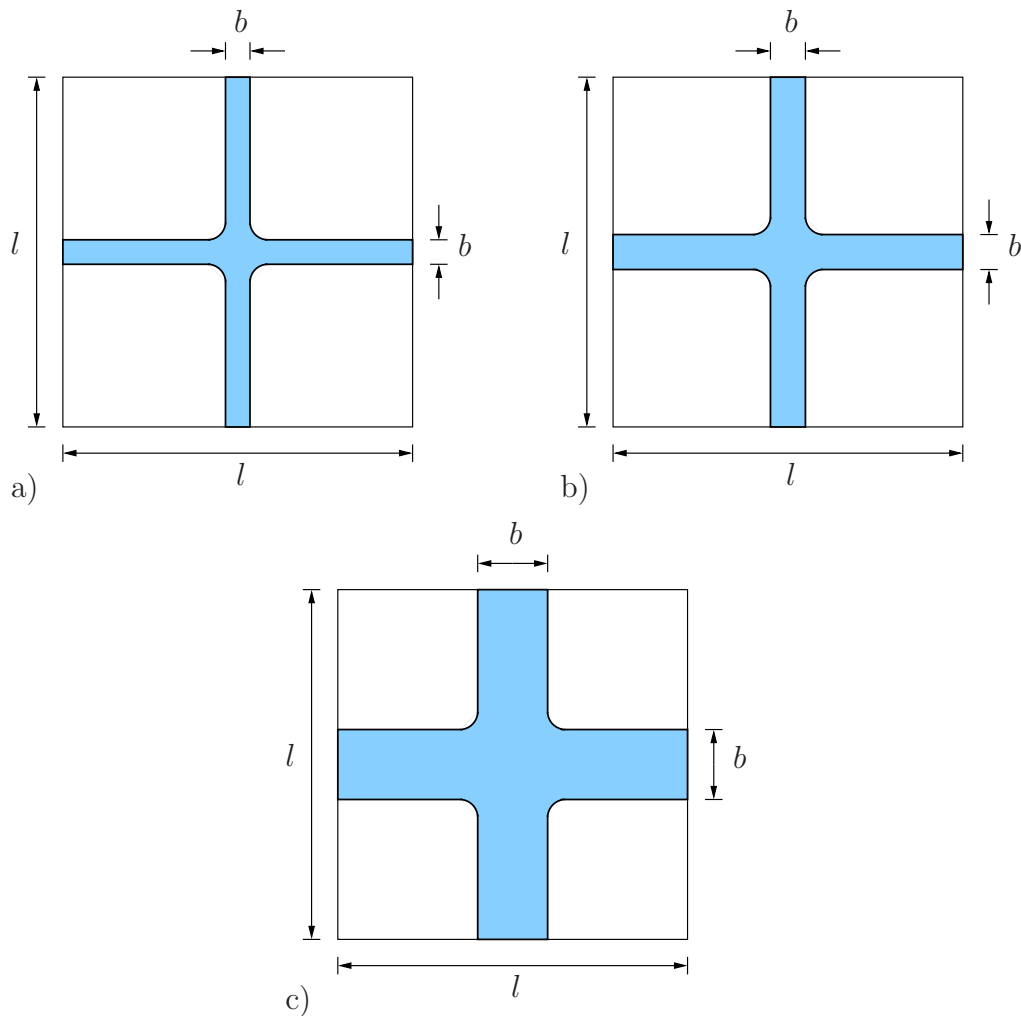


Figure 8.1: The unit cells of the investigated regular cross-like microstructures with the constant size l^2 . The aspect ratio b/l of the struts increases from a) $1/15$ and b) $1/10$ to c) $1/5$.

8.2 Experimental setup

In order to investigate the properties of the single-cross microstructure and its influence on the effective material behaviour, several numerical experiments have been accomplished. In fig. 8.2, a basic geometry is sketched including the sample size and the assignment of the boundaries.

For all the following experimental setups, the question arises, which could be,

from the physical point of view, the appropriate formulation of the boundary conditions for the microdeformation $\bar{\chi}_M$.

To answer this question, one may recall the interpretation of the deformation modes depending on $\bar{\chi}_M$, cf. fig. 5.1. It has been shown the microdeformation not to account for any effective deformation of the microvolume. By contrast, it has been pointed out the induced cubic fluctuation of the boundary to regularise the microscopic deformation state by rotation of the struts. In the case of the single-cross microstructures, the struts connected to the boundary must stay fixed. In terms of boundary conditions, the assumption of an unrotated boundary for every single strut connected to the boundary should be meaningful from the physical point of view.¹ Consequently, the microdeformation is chosen

$$\bar{\chi}_{M12} = \bar{\chi}_{M21} = 0 \quad \text{on} \quad \partial\mathcal{B}_D. \quad (8.1)$$

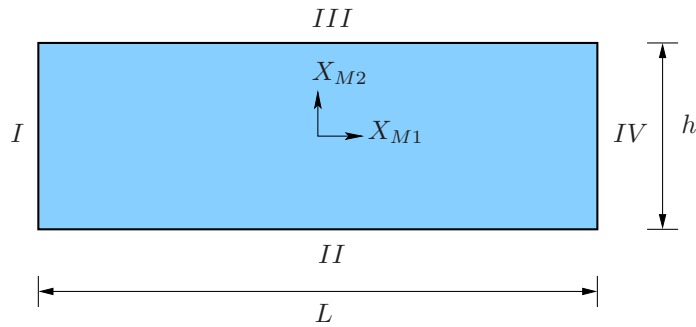


Figure 8.2: Sketch of the macroscopic geometry and assignment of the boundaries.

The first numerical experiment assumes an infinite domain of the width $L \rightarrow \infty$ and of the variable height h under shear conditions. Introducing periodicity conditions for the boundaries *I* and *IV*, we may restrict the numerical calculations to a very slender domain ($L \rightarrow 0$). Thus, one may introduce the shear test defining the Dirichlet boundary conditions

$$\begin{aligned} \bar{u}_{M1}^{II} &= 0, & \bar{\chi}_{M12}^{II} &= 0, \\ \bar{u}_{M2}^{II} &= 0, & \bar{\chi}_{M21}^{II} &= 0, \end{aligned} \quad (8.2)$$

¹Throughout the numerical experiments, it has figured out that prescribing boundary conditions for the microstrain components $\bar{\chi}_{M11}$ and $\bar{\chi}_{M22}$ does not influence the effective material response, i. e. the lateral stretching of the struts is of subordinate significance for the analysed cellular structures.

at boundary *II* and

$$\begin{aligned}\bar{u}_{M1}^{III} &= 0.01 \cdot h, & \bar{\chi}_{M12}^{III} &= 0, \\ \bar{u}_{M2}^{III} &= 0, & \bar{\chi}_{M21}^{III} &= 0,\end{aligned}\tag{8.3}$$

at boundary *III*, i. e. the overall shear deformation accounts for 1%.

The numerical tension experiment assumes again an infinite domain in X_{M1} -direction and a variable height h . Thus, the boundaries *I* and *IV* are kept periodic and one defines the Dirichlet boundary value problem by

$$\begin{aligned}\bar{u}_{M1}^{II} &= 0, & \bar{\chi}_{M12}^{II} &= 0, \\ \bar{u}_{M2}^{II} &= 0, & \bar{\chi}_{M21}^{II} &= 0,\end{aligned}\tag{8.4}$$

at boundary *II* and

$$\begin{aligned}\bar{u}_{M1}^{III} &= 0, & \bar{\chi}_{M12}^{III} &= 0, \\ \bar{u}_{M2}^{III} &= 0.01 \cdot h, & \bar{\chi}_{M21}^{III} &= 0,\end{aligned}\tag{8.5}$$

at boundary *III*, i. e. the overall stretching accounts for 1%.

To circumvent the, at least in the X_{M1} -direction, homogeneous boundary conditions of the preliminary numerical experiments, a three point bending test has been investigated for several sample sizes. Introducing a symmetry condition for boundary *IV*, the Dirichlet boundary conditions for the boundary *I* read

$$\begin{aligned}\bar{u}_{M1}^I &= 0, & \bar{\chi}_{M12}^I &= 0, \\ \bar{u}_{M2}^I &= 0, & \bar{\chi}_{M21}^I &= 0,\end{aligned}\tag{8.6}$$

and for boundary *IV*

$$\begin{aligned}\bar{u}_{M1}^{IV} &= 0, & \bar{\chi}_{M12}^{IV} &= 0, \\ \bar{u}_{M2}^{IV} &= 0.01 \cdot L, & \bar{\chi}_{M21}^{IV} &= 0.\end{aligned}\tag{8.7}$$

At the boundaries *II* and *III*, Neumann boundary conditions are assumed in such a way that all fluxes equal zero, i. e. these boundaries are not loaded.

8.3 Shear test

Let us begin the numerical investigations with the above mentioned shear experiment. In classical continuum mechanics, the given set would be called a homogeneous shear experiment. Nevertheless, this denotation does not hold in our case due to boundary effects. This can be clearly observed in fig. 8.3 a), where the symmetric and the skew-symmetric parts of the microshear deformation are plotted over the sample height ($n = 15$), both not constant and therefore not homogeneous in X_{M2} -direction.

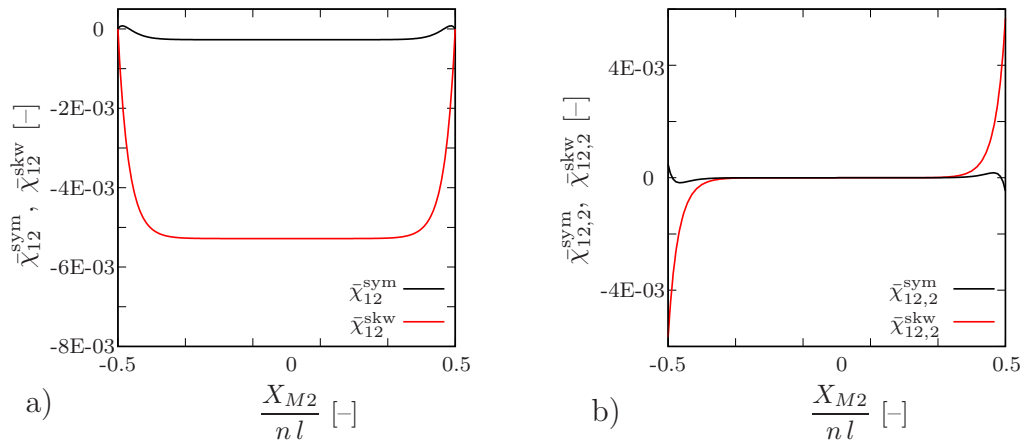


Figure 8.3: a) Symmetric and skew-symmetric microshear deformation over the height of the sample within a FE² calculation of the shear test for $n = 15$ and $b/l = 1/15$. b) The particular symmetric and skew-symmetric curvatures.

By contrast, the skew-symmetric microshear deformation exhibits a plateau of about $5.2E-03$ which collapses close to the boundary, following the boundary condition. This may be found reflected in the microdeformation gradient on the right hand side of fig. 8.3, where the collapse of the microdeformation leads to a distinct increase close to the boundary involving an alternating sign. Far away from the boundary, the microshear deformation gradient vanishes and describes a plateau at the null level.

Compared to the skew-symmetric microshear deformation, its symmetric counterpart seems to be negligible. Thus, this first plot indicates the chosen microstructure to feature a Cosserat medium, where the microshear deformation is chosen skew-symmetric per definition. This consideration will be subject to further investigations in the latter.

But prior to that, let us study the effect of the detected macroscopic microdeformations on the microstructural unit cell. In fig. 8.4, the single-cross unit cell is displayed, where the micromorphic projection rule has been applied. Fig. 8.4 a) represents the macroscopic deformation state, observed at the top boundary, b) that one observed in the center of the sample, projected on the unit cell.

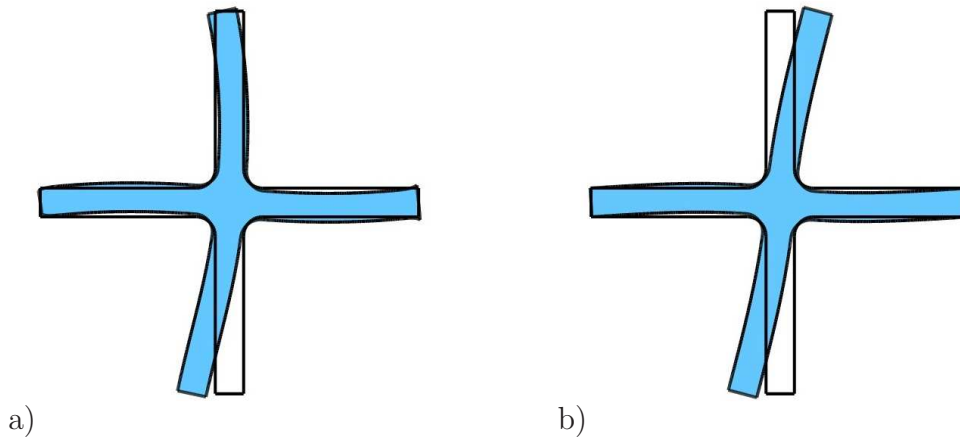


Figure 8.4: Deformation of the microvolume at the positions a) $X_{M1} = 0$, $X_{M2} = h/2$ and b) $X_{M1} = 0$, $X_{M2} = 0$ ($b/l = 1/15$). To generate the sketches, the deformation measures at the given positions of the FE^2 calculations have been projected back to the boundary of the microvolume.

Obviously, the microscopic deformation states differ from a) to b). Whereas at the boundary, the vertical strut is bent, the situation in the center is dominated by the shear deformation. The layer close to the boundary is exactly the place, where the microdeformation gradient becomes active. Thus, the interpretation of the quadratic deformation modes as bending modes raised earlier is backed up by this example. One may furthermore focus on the rotation of the struts in fig. 8.4. In a), the rotation can be explained by the characteristic bending deformation mode, cf. fig. 5.2 b), applied in X_{M2} -direction, and in combination with fig. 5.2 c). By contrast, the rotation of the vertical struts at the central position solely results from the microdeformation component $\bar{\chi}_{M21}$, cf. fig. 5.1 b) and, applied for the X_{M2} -direction, fig. 5.1 d). Hence, the regularising effect of the microdeformation is apparent. Allowing for periodic rearrangements, the microdeformation enables the microstructure to relax.

In fig. 8.5, the skew-symmetric microshear deformation and the associated curvature have been depicted varying the height h of the macroscopic sample

from 5 over 15 to 40. One finds the central plateau to vanish if the sample size is chosen small, the boundary layers are dominating nearly whole the volume, whereas they become very small for the large macroscopic sample size. Taking into account the normalised character of the height within the given plot, one may notice the boundary layer to cover a constant size of about two layers of unit cells, independent of the absolute size of the sample. This is the typical boundary layer effect for cellular materials under shear deformation which is well-documented in literature, e. g., beyond numerous further publications, [3, 13, 22, 77, 100].

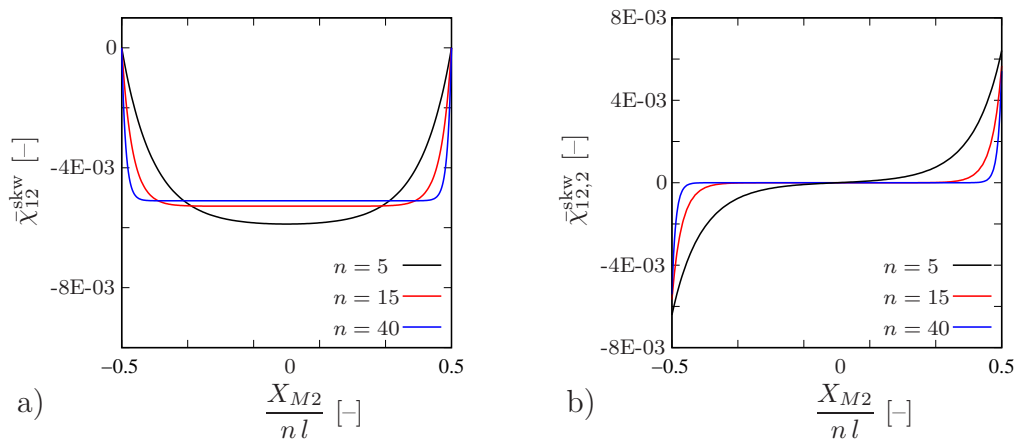


Figure 8.5: a) Skew-symmetric part of the microdeformation over the height of the sample within a FE² calculation of the shear test and its development with increasing sample size n , $b/l = 15$. b) The particular skew-symmetric component of the curvatures and its development.

Let us now proceed to the quantitative comparison of the extended two-scale results to those of first order FE² calculations including periodic boundary conditions on the one hand and to those of reference calculations with microscopic resolution on the other hand. For that purpose, the shear traction observed at the macroscopic boundary III , cf. fig. 8.2, has been normalised to that one of a very large macroscopic sample and has been plotted versus the height of the sample, i. e. the number of unit cells in X_{M2} -direction. In figs. 8.6 – 8.8, the particular results are plotted for the different underlying aspect ratios on the left hand side. On the right hand side, the error relative to the reference solution is depicted. Note the extended FE² algorithm here to be applied without any further periodic boundary condition.

At first, having regard to the reference solutions, the effect of the boundary layer effect becomes apparent. It causes a stiffening effect decaying with increasing sample size and converging versus a limiting value for an infinitely

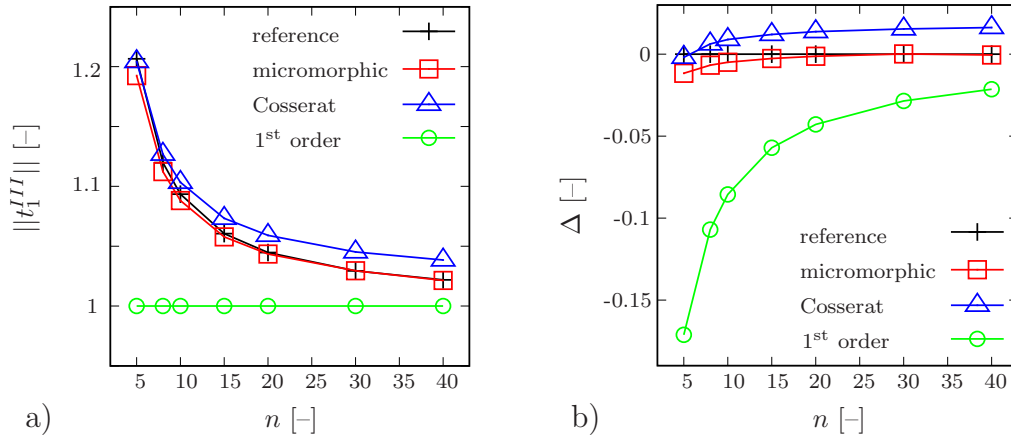


Figure 8.6: a) Normalised traction at surface *III* (aspect ratio $b/l = 1/15$). b) Relative error of the FE² calculations in comparison to the reference solution.

large sample. For all investigated aspect ratios, that stiff boundary effect accounts for about 20%. Let us focus now on the first order approach. As it has been mentioned before, the first order methodology does not involve any transition of the microstructural length scale to the macrolevel. Consequently, the solutions obtained by this technique are absolutely insensitive for the macroscopic sample size. Thus, for small samples, the stiffening effect can not be displayed at all, but the solution converges towards the plateau for infinitely large sample sizes. More precisely, for a perfectly periodic microstructure, the first order results themselves represent the plateau. Analogously, the relative error of the first order results accounts for the stiff boundary layer effect and consequently decays from about 20% to 2% for $n = 40$.

By contrast, now taking into account the micromorphic extension of the two-scale approach, one finds the distinct boundary layer effect to be modelled in an excellent manner by the full micromorphic methodology. Especially for the most slender aspect ratio $b/l = 1/15$, the relative error, even for the smallest investigated sample $n = 5$, does not exceed 2%. With increasing thickness of the microstructural struts, the solution predicted by the micromorphic model becomes slightly softer than that one of the reference calculations. Thus, for $b/l = 1/5$, one finds a maximum relative error of about 6%. But already for $n = 15$, the error is falling below 2% and for even larger samples, the micromorphic result is not distinguishable from the reference result. The decay in the modelling exactness may be interpreted as the limiting case of the given projection procedure. As it has been men-

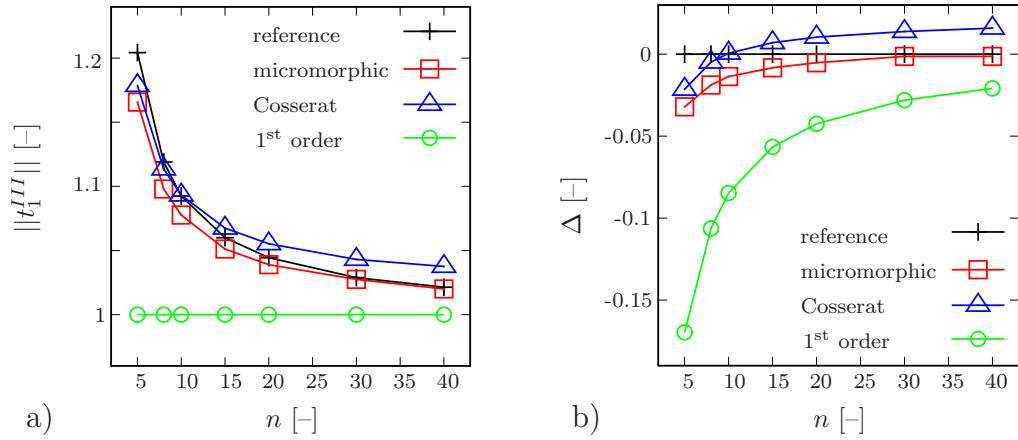


Figure 8.7: a) Normalised traction at surface III (aspect ratio $b/l = 1/10$). b) Relative error of the FE^2 calculations in comparison to the reference solution.

tioned before, the polynomial expansion introduces the assumption, similar to the Bernoulli hypothesis, that the boundary cross-sections should stay planar during rotation. Obviously, this restriction starts to fail for too thick microstructural struts. Analogously, the Bernoulli hypothesis is well-known to fail if the aspect ratio of a beam exceeds $b/l = 1/10$.

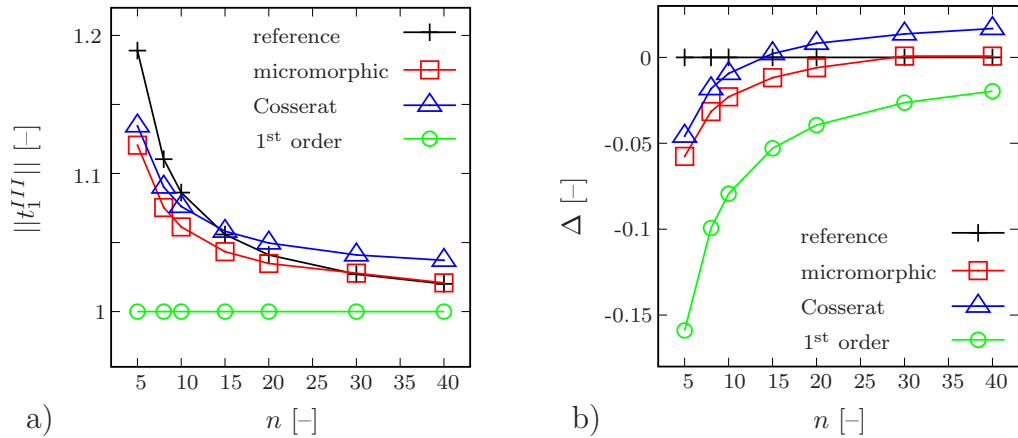


Figure 8.8: a) Normalised traction at surface III (aspect ratio $b/l = 1/5$). b) Relative error of the FE^2 calculations in comparison to the reference solution.

Having regard to the skew-symmetric character of the microshear deformation, one may restrict the macroscopic continuum model to the micropolar case, i. e. to a Cosserat continuum. Reducing the degrees of freedom of the model and restricting the particular microstructural deformation mech-

anisms, one should suppose the micropolar solutions to exhibit a slightly stiffer stress response than the full micromorphic model. That is exactly what one finds depicted in figs. 8.6 – 8.8. For all the investigated unit cells, the micropolar response is about 2% stiffer than the micromorphic ones, in the boundary layer as well as in the volume of the sample. In the case of the third microstructure with $b/l = 1/5$, this leads to the situation that the micropolar model pretends a higher accuracy than the micromorphic model for small sample sizes. But, off course, this effect results from the superposition of two systematic errors. Nevertheless, the micropolar model is still generating much more precise results than it does the first order methodology, especially for small sample sizes.

In fig. 8.9, the relative errors of both extended approaches are displayed for the different investigated unit cells.

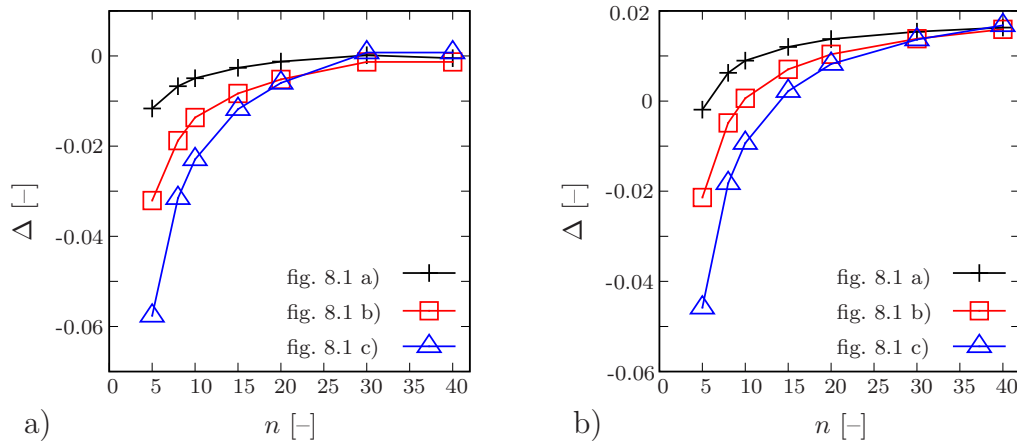


Figure 8.9: Combined relative errors of the FE^2 calculations for the microstructures depicted in fig. 8.1. a) Micromorphic model, b) micropolar (Cosserat) model.

8.4 Tension test

Let us now consider an infinite domain in X_{M1} -direction with the variable height h under stretching deformation. Due to the microtopology, the effective material behaviour is highly compressible so that this experiment does not produce an infinitely large tensile stress. In the previous section, we

have found the boundary stiffening to be associated with bending effects which result from the restricted rotation of the microstructural struts at the macroscopic boundary. For the given regular structure, no rotation must be induced by the stretching deformation state. Consequently, there should occur no boundary stiffening effect. This is exactly the result which can be observed in fig. 8.10.

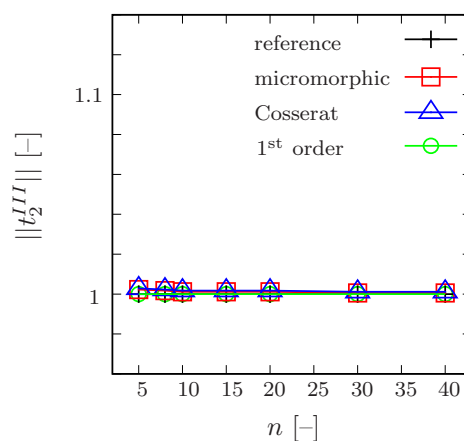


Figure 8.10: Normalised tensile traction at surface *III* ($b/l = 1/15$).

8.5 Bending test

The following section now concentrates on the above described three-point bending test, applied for the slender microstructure fig. 8.1 a). Note that there is a fundamental difference to the previous experimental setups. Whereas so far, the complete boundary has been defined as a Dirichlet boundary $\partial\mathcal{B}_D$, now the boundary is a combination of a Dirichlet boundary and a Neumann boundary, i. e. $\partial\mathcal{B} = \partial\mathcal{B}_D \cup \partial\mathcal{B}_N$, including the unloaded parts. Thus, one has to expect a soft layer close to the unloaded boundary. By contrast, the underlying microscopic boundary value problems have been defined solely implementing Dirichlet boundary conditions. It seems to be obvious the two-scale approach, may it be the first order or the extended one, to predict the boundary layer close to the free boundary in a too stiff manner. In order to circumvent this failure, modified microvolumina have been introduced for the upper and the lower free boundaries. The modification is depicted in fig. 8.11, on the left hand side for the micromorphic, on the right hand side for the linear homogenisation procedure. In both cases, one strut

is left unloaded, depending if the particular microvolume is attached to the top or to the bottom boundary layer. I. e. in analogy to the macroscopic boundary conditions, one strut is loaded with the Neumann condition $\mathbf{f} = \mathbf{0}$, where \mathbf{f} represents a force vector on the boundary. For the micromorphic approach, the remaining boundaries are loaded in the usual way with the aid of the projection rule. In the case of the first order homogenisation, the relaxation of the struts is ensured by the use of periodic boundary conditions. Obviously, the boundary opposite to the free one has no periodic counterpart and the application of periodic boundary conditions is not possible. To avoid a too stiff material response, the particular boundary conditions may be approximated by a pin-point in the center of the opposite boundary, where the boundary conditions can be applied. The rest of the boundary has been left unloaded, cf. fig. 8.11 b).

For the application within the FE² procedures, the introduced modified unit cells have been attached to the integration points within a layer of the width l parallel to the free boundaries. I. e. the layer comprises the size of one unit cell.

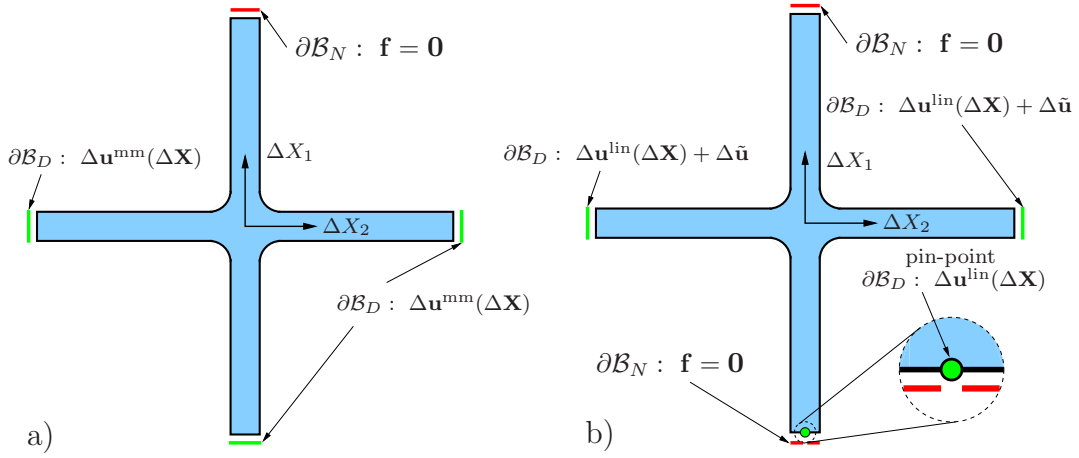


Figure 8.11: Modified microscopic boundary value problem for the macroscopic free Neumann boundary *III* in the bending test, applied a) to the micromorphic, b) to the first order homogenisation scheme involving periodic boundary conditions.

In order to study the superposition on the one hand of the mentioned softening effect induced by the unloaded boundaries and on the other hand of the stiffening effect induced by the restricted microstructural kinematics close to the macroscopic Dirichlet boundaries, two different macroscopic sample geometries have been investigated. Using the notation in analogy to fig. 8.2,

the first case assumes a sample width $L = 10l$, the second one a larger with $L = 32l$. Both geometries deal with a variable sample height $h = ml$, where m defines the number of unit cells in X_{M2} -direction. In both cases, the vertical reaction force RF_2^{IV} integrated over the right hand side boundary IV and normalised to that one of an infinitely large sample has been observed depending on the number m of vertical unit cells. The results are depicted in figs. 8.12 and 8.13. On the right hand side of the plots, one may find the relative error with respect to the particular reference calculations.

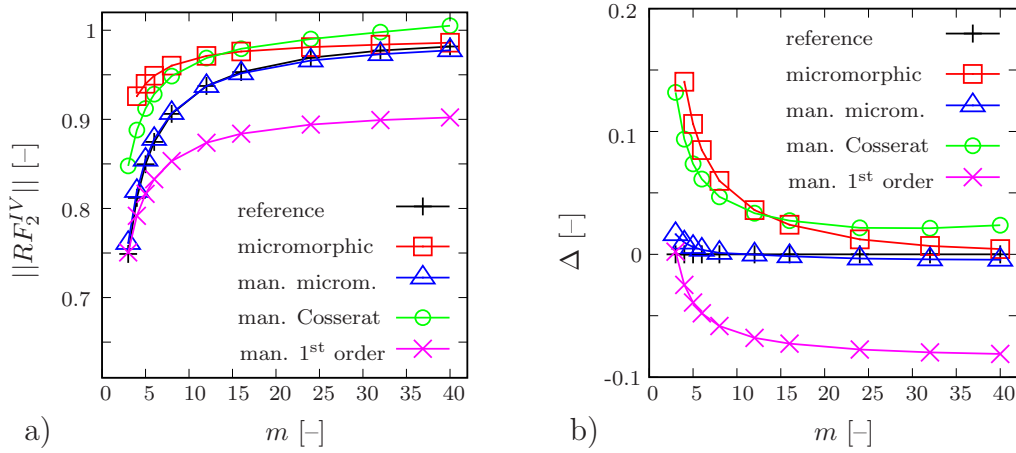


Figure 8.12: Bending experiment $L = 10l$ and $h = ml$ for $b/l = 1/15$. a) Normalised reaction force RF_2^{IV} in X_{M2} -direction, integrated over boundary IV . (man.=manipulated) b) Relative error of the FE^2 calculations in comparison to the reference solution.

Regarding at first fig. 8.12, one finds the reference solution to exhibit the predicted soft boundary layer effect of about 13%, induced by the unloaded boundary. Note that for the given example, even the most slender macroscopic geometry features an aspect ratio of $h/L = 2/5$. Thus, the given example is not subject to a pure bending deformation but to a superposition of bending and shear deformations. Considering the results of the micromorphic methodology, one finds the pure algorithm with full Dirichlet support to result in a soft boundary layer effect. But this one is much less pronounced than it is that one of the reference calculation. For larger m , the result converges towards the limiting case of the infinite domain, cf. fig. 8.6. However, the manipulation of the microvolumina attached to the unloaded boundary layer leads to a highly accurate modelling of the softening effect. Indeed, even for $m = 3$, the relative error accounts for less than 2%. By contrast, the modified methodology does not provide the micropolar (Cosserat) FE^2 scheme to meet the reference results. Besides the systematical error for large

m similar to those discussed for the shear experiment, the soft boundary layer is modelled in a quite stiff manner, resulting in a relative error of about 14 % for $m = 3$. Finally, considering the first order methodology, one observes for large m that this approach is not able to deal with the stiff boundary effect induced by the boundaries *III* and *IV*, cf. fig. 8.6. However, for smaller m , the soft boundary effect seems to be displayed but in a less pronounced way than it does the reference solution. I. e. instead of 14 % softening one finds only about 8 % softening.

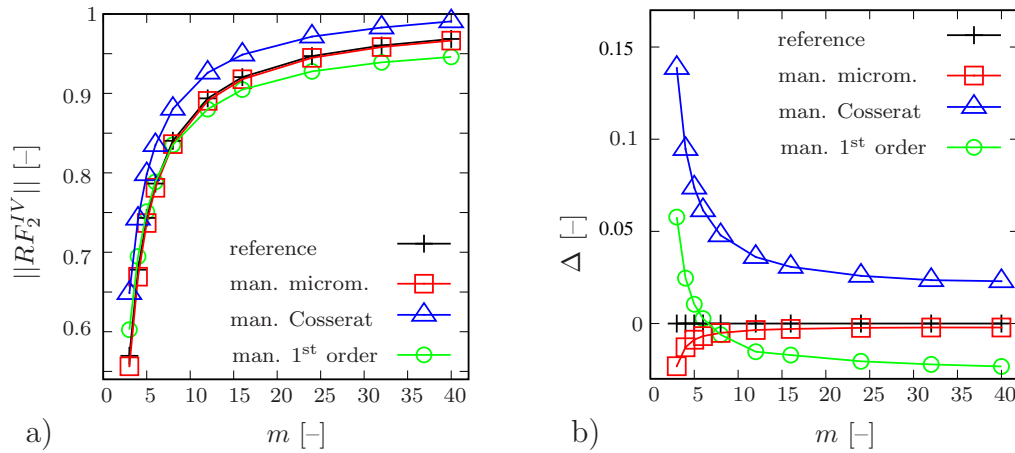


Figure 8.13: Bending experiment $L = 32l$ and $h = ml$ for $b/l = 1/15$. a) Normalised reaction force in X_{M2} -direction, integrated over boundary *IV*. b) Relative error of the FE^2 calculations in comparison to the reference solution.

Focusing now on the second geometry with $L = 32l$, one finds in analogy to fig. 8.6 the stiff boundary effect to be less pronounced. Again, the modified micromorphic approach provides the most exact result with a maximum relative error of less than 3 % for $m = 3$, whereas the micropolar model results in a too stiff modelling of the soft boundary layer. For the linear approach, one finds, besides the systematic error due to the lack of the stiff boundary layer, a too stiff description of the softening effect.

8.6 Size of the microvolume

After having demonstrated the power of the introduced two-scale approach for the smallest possible entity on the microlevel, i. e. the single-cross unit

cell, the question arises, if a different choice would lead to similar results. For that reason, an enlarged unit cell consisting of four crosses ($b/l = 15$), similar to fig. 6.1 d), with the edge length $2l$ has been subject to the above mentioned shear test. I. e. for the FE^2 calculations, the attached microvolume has changed whereas the reference solution has not been touched. The results are given in fig. 8.14.

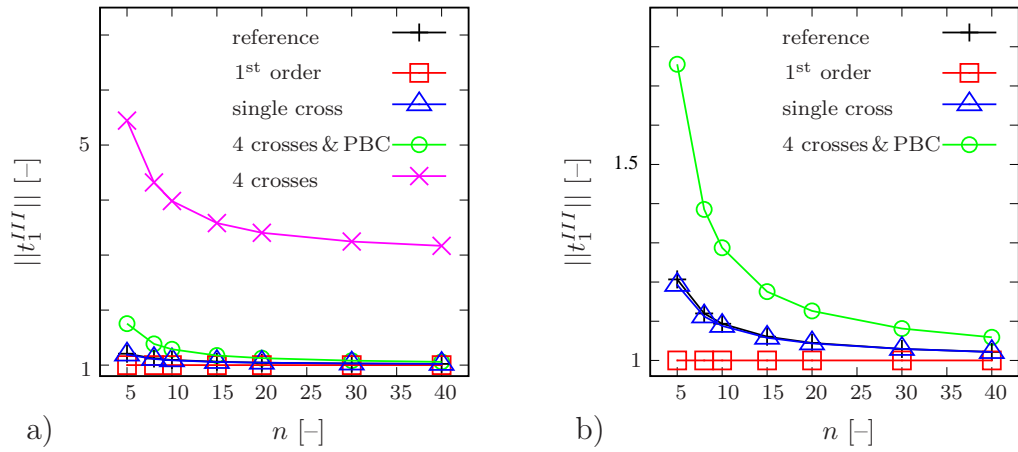


Figure 8.14: Normalised traction at surface III . The square unit cell of the size $(2l)^2$ consists of 4 single crosses (aspect ratio $b/l = 1/15$). The sample height calculates as $h = nl$. Figure b) is depicting a detail of a).

Obviously, the four-cross unit cell predicts an effective shear stiffness which differs more than 300%. The chosen kinematics is neither able to regularise the periodic deformations far away from the boundary nor to describe the bending deformation in an acceptable way. The enrichment of the extended projection rule with higher periodic boundary conditions allows the particular struts to rotate independently. This choice leads at least to a meaningful convergence towards the stiffness of an infinitely large sample. But again, the stiffness of the boundary layer is overestimated by about 50%. By contrast, the first order methodology including periodic fluctuations is absolutely insensitive for the change in the microvolume size.

Hence, the present study accords to the results found in chapter 6. It has been pointed out the cubic expansion of the projection polynomial to describe periodic deformations of an 1-particle system. Furthermore, it has been mentioned, the microdeformation to loose its physical meaning for $(n > 1)$ -particle systems. That is exactly what one observes in the given investigation. Whereas in the center of the sample, i. e. in a region free of disturbances induced by the rigid boundary conditions, the periodic deformations can be

displayed by free periodic fluctuations, the disproportionately high bending stiffness of the enlarged unit cell results in a much too stiff boundary layer.

8.7 Discussion

Let us close the numerical investigations concerning the single-cross microstructure with a brief outline of the found results:

- It has been demonstrated the extended FE²-technique to describe the deformation processes in a rather exact way under shear, stretching and bending loading conditions. The skew-symmetric character of the observed microdeformation, free of microstrain deformations, has indicated to apply the micropolar (Cosserat) subcontinuum on the macroscale. This procedure leads to qualitatively meaningful results but predicts a slightly too stiff effective material behaviour.
- By the introduction and the appropriate attachment of modified microvolumina it has been possible to incorporate unloaded Neumann boundary conditions. Whilst the first order methodology has been able to display the soft boundary layer effect with a certain accuracy, the extended scheme could produce even exacter results.
- Nevertheless, at least two limits of the micromorphic two-scale approach have been detected. The first one concerns the slenderness of the investigated cellular structures. Because the cubic polynomial expansion, similar to the Bernoulli hypothesis of planar intersections, offers only restricted deformations of the Dirichlet boundaries – i. e. a rotation of the boundary – the exactness of the method depends on the slenderness of the cellular struts. The given study indicates an aspect ratio of $b/l \leq 1/10$ to be meaningful from the physical point of view.
- Secondly, the physical interpretation of the microdeformation and its gradient requires the attached microvolume to be an 1-particle system.

Especially this second limitation will be subject to further investigations in the following chapters. At first, the size of the central vertex within an 1-particle system will be discussed. In the latter, an interpretation of the honeycomb structure as a 1-particle system will be given.

9

Modified single-cross microstructures

After having examined the regular single-cross microstructure, let us study the influence of the size of the central vertex in the sequel. To do so, the single-cross structure will be modified by introducing a set of four subordinate vertices. After having defined the microtopology, the resulting microstructures will be subject to a numerical shear test.

9.1 Microtopology and experimental setup

The underlying microtopologies are depicted in figs. 9.1 and 9.2 in a schematic manner. As it has been mentioned before, the central vertex in 9.1 a) has been replaced by a set of four subordinate vertices with increasing distance from 9.1 b) to 9.2 b). Finally, microstructure 9.2 c) represents again a single-cross microstructure with the strut length $l_2 = l/\sqrt{2}$, rotated by 90° .

The experimental setup is identical to that one introduced in chapter 8, cf. fig. 8.2. The height of the sample is scaled using the number n of vertical

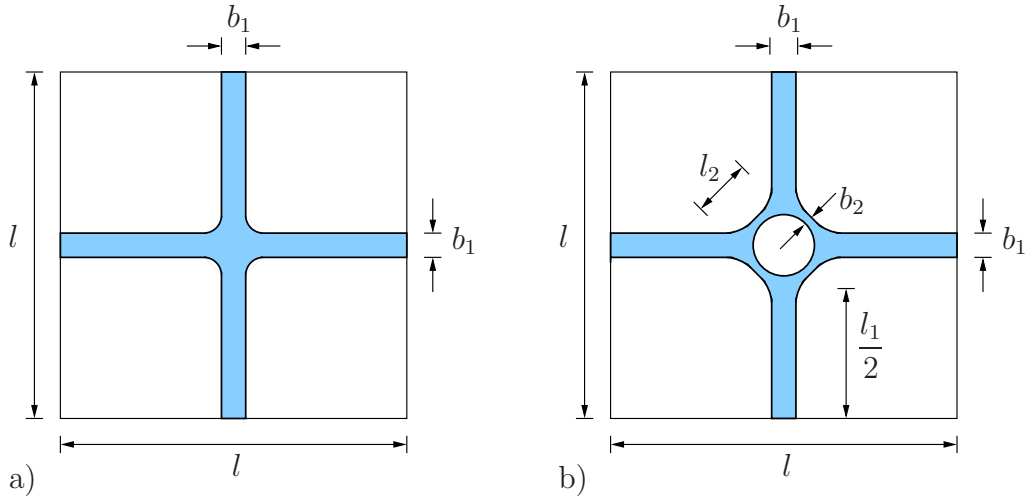


Figure 9.1: The unit cell of the modified single-cross microstructure with the constant size l^2 . a) $b_1/l_1 = 1/12$, $b_2/l_2 = 1/1$, b) $b_1/l_1 = 1/8$, $b_2/l_2 = 1/5$.

unit cells.

9.2 Shear test

To simplify matters, the results of the given shear experiments are not displayed in detail. However, the relative error resulting from the shear stress of the micromorphic FE^2 -methodology with respect to that one of the reference calculations is depicted in fig. 9.3 b). Note that microstructure 9.2 c) features a rotated subsystem of single-crosses. Under shear deformation, the microstructural struts are oriented parallel to the macroscopic shear deformation. I. e. the local shear or bending effects must vanish. Consequently, this particular case does not show any boundary stiffening effect, cf. 9.3 a). Of course, both, the first order as well as the extended methodology, are able to predict this effective material behaviour. By contrast, microstructures 9.1 a) – 9.2 b) feature a distinct boundary layer effect. Regarding the relative error of the calculations, cf. fig. 9.3 b), we find at first, similar to the investigation in chapter 8, the micromorphic model for microstructure 9.1 a) to underestimate the stiffening effect in a very slight manner by about -2%. By contrast, one may observe a tendency to an overestimation of this effect by the following microstructures, the relative error increases from +2% to +10% and +15%. Thus, for microstructures 9.2 a) and b), the relative error

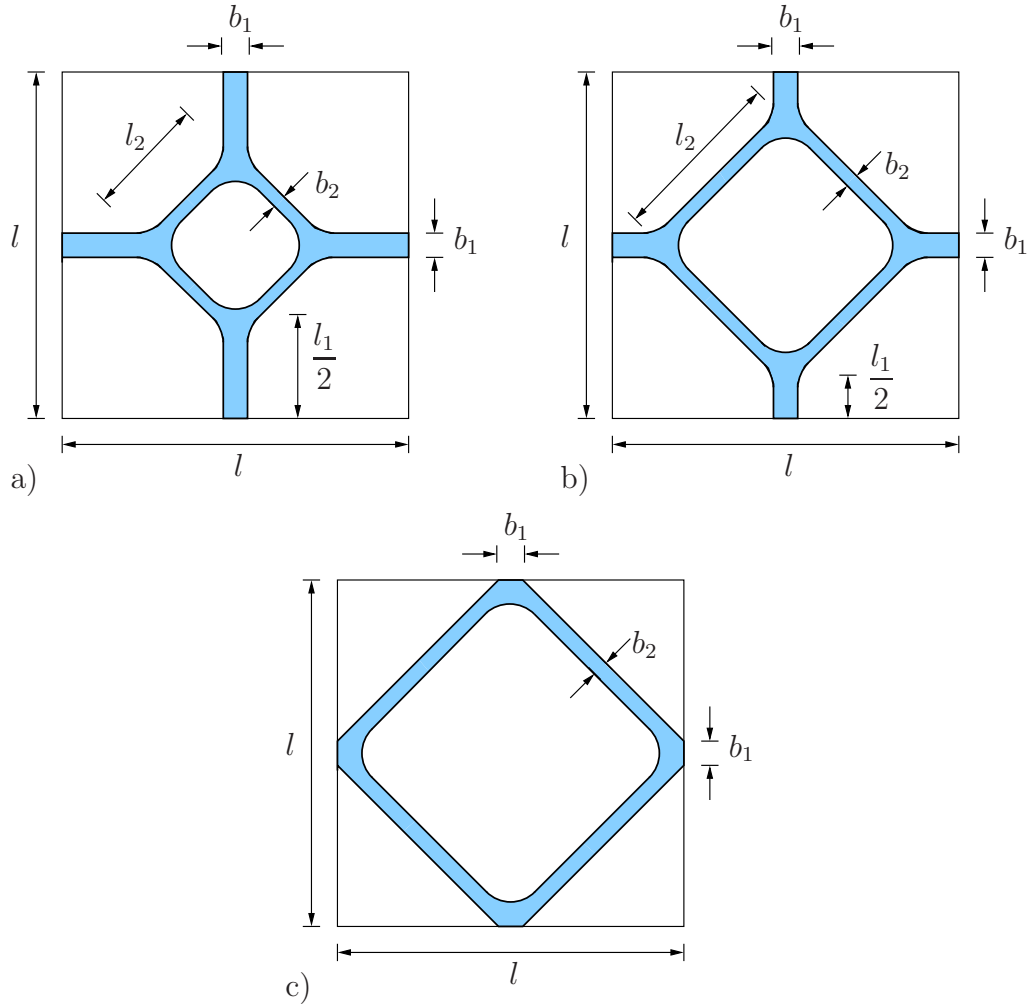


Figure 9.2: The unit cell of the investigated modified single-cross microstructure with the constant size l^2 . a) $b_1/l_1 = 1/20$, $b_2/l_2 = 1/20$, b) $l_1/b_1 = 1/10$, $l_2/b_2 = 1/30$, c) $l_1/b_1 = 1/1$, $b_2/l_2 = 1/30$.

reaches the order of magnitude of the stiffening effect itself.

9.3 Discussion

Consequently, one has detected a further limitation of the extended two-scale algorithm. Talking about cellular structures as systems of vertices connected via slender struts, i. e. the aspect ratio of the struts should be smaller than

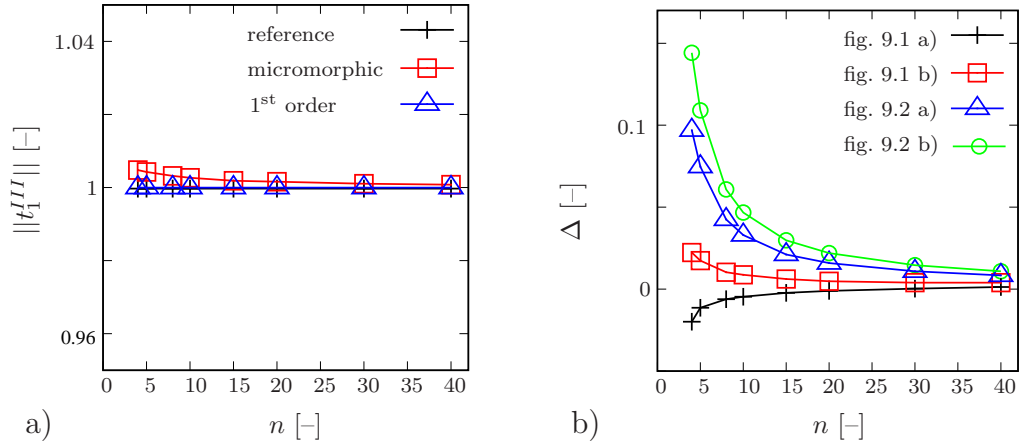


Figure 9.3: a) Microstructure fig. 9.2 c). Normalised traction at surface III . b) Combined relative error of the FE^2 calculations for the microstructures fig. 9.1 a) – 9.2 b).

1/10, one has to take into account the size of the central vertex. Due to the qualitative character of the present study, it is not possible to limit the size of the vertex exactly. But one may notice that the micromorphic methodology requires the deformation behaviour of the microstructure to be dominated by the deformation of the connecting struts and not by the kernel deformation.

From the physical point of view, the deformation should comprise on the one hand the periodic properties provided by the cubic expansion of the projection polynomial. Obviously, this is true for all the investigated unit cells. The convergence for large shear samples shows that the periodic deformation of the slender struts connecting the kernels is displayed by the microscopic deformation modes. On the other hand, the bending properties must be displayed at the same time. And apparently, the larger kernels feature a more complex bending behaviour than it can be described applying the quadratic deformation modes.

Altogether, it is an open question what happens if the kernels are closed, i. e. if they do not perform sets of subordinate vertices but really compact ones. Nevertheless, in the author's opinion, the case of large and compact vertices is not really relevant for the modelling of cellular structures and will not be subject to further investigations here.

10

Honeycomb structure

As already mentioned in chapter 6, a further class of regular two-dimensional foam models is the honeycomb microstructure as it is depicted in fig. 10.1.¹ The deformation behaviour of the natural unit cells, i. e. the rhombic ones displayed in fig. 6.1 b) and c), has turned out not to be covered by the micromorphic polynomial in a very precise way. For that reason, another definition for the unit cell will be discussed in the sequel. Afterwards, the microstructure will be subject to different numerical experiments.

10.1 Microtopology

Following the discussion raised in the preceding chapters, a physically meaningful interpretation of the micromorphic degrees of freedom can be found assuming a system of vertices connected via deformable struts. A further implicit assumption has been the unit cell to be centrosymmetric, i. e. the

¹An analytical homogenisation scheme describing the effective properties of honeycomb structures has been derived in detail by Gibson and Ashby [50].

volume centroid equals the center of mass. Surely, for the honeycomb unit cells depicted in fig. 6.1 b) and c), the volume centroid and the mass centroid are identical. But obviously, the mass is not concentrated in the mass centroid but in the two vertices.

To find a more adequate description for the honeycomb unit cell, let us regard the structure in fig. 10.1. The 2-particle unit cell is replaced by a rectangular one. This geometry change is in order to simplify the definition of the projection polynomial. Furthermore, the unit cell is split up into two identical parts, microvolume 1 and 2, which differ only in their orientation.

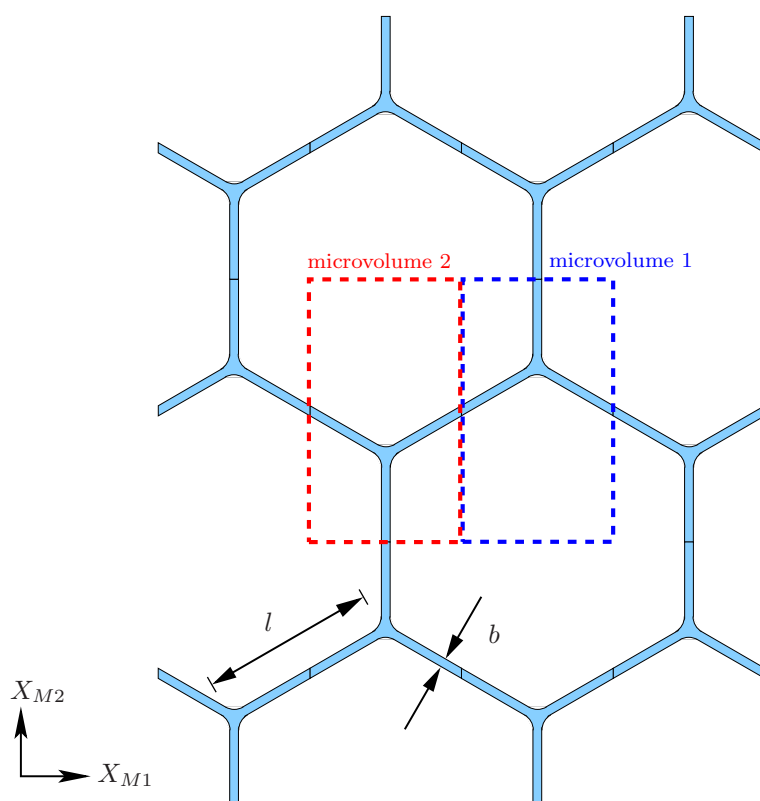


Figure 10.1: The regular, periodic honeycomb structure. Aspect ratio of the struts $b/l \approx 1/15$.

In fig. 10.2, the two parts of the unit cell are depicted in detail. Having in mind the property of the cubic polynomial expansion to rotate the center of the particular boundaries, the microvolumina are constructed in a way that the struts are cut in the center of the boundary. Additionally, the cross-sections at the boundary are located in the center of the particular struts. Examining the honeycomb structure within FE^2 calculations, it has

figured out that the two parts of the unit cell can be superimposed to one microvolume. In other words: At a given macroscopic integration point, the macroscopic deformation quantities are projected to both parts of the unit cell at the same time. The microvolume is assumed to account for the edge lengths $\sqrt{3}l/2$ and $3l/2$. Thus, two microscopic boundary value problems have to be solved for each macroscopic integration point. Afterwards, the macroscopic stress quantities have to be homogenised for each part of the unit cell separately and the effective value of the stresses can be calculated as the arithmetic average of the particular results, cf. [23]. Note that throughout the following examples no higher periodic boundary conditions are taken into account for the micromorphic homogenisation scheme on the microlevel, i. e. free microscopic periodic fluctuations are only considered for the first order FE²-calculations.

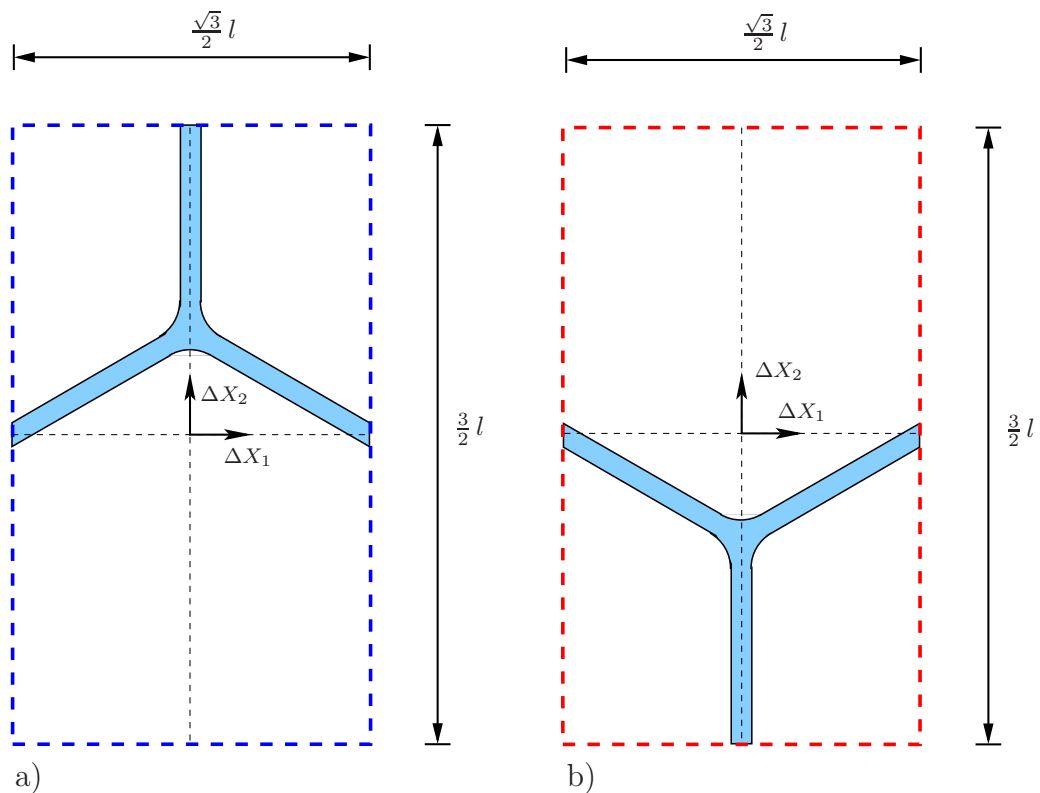


Figure 10.2: Detail from fig. 10.1: One pair of microvolumina featuring one unit cell of the investigated regular honeycomb microstructure.

10.2 Shear test

The experimental setup of the shear test is in accordance to fig. 8.2, where $L \rightarrow \infty$. The loading of the sample takes place in X_{M1} -direction. In the sequel, two orientations of the microstructure will be investigated, at first, the orientation given in fig. 10.1, secondly the same microstructure rotated by 90° . Whereas the shear test for the first orientation deals with $h = n l / 2$, that one for the second orientation uses $h = n \sqrt{3} l$, i. e. $n = 1$ represents one assembly of the microvolumina 1 and 2, cf. fig. 10.2.

Let us begin with a qualitative analysis of the microdeformation observed in a FE² computation. In fig. 10.3, the microshear deformation components $\bar{\chi}_{M12}$ and $\bar{\chi}_{M21}$ are depicted for a shear test in the unrotated configuration.

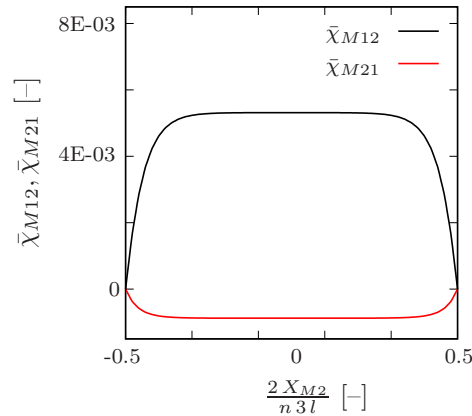


Figure 10.3: Shear test in X_{M1} -direction. Microshear deformation components $\bar{\chi}_{M12}$ and $\bar{\chi}_{M21}$ over the height of the sample ($n = 8$).

Both characteristics exhibit a boundary layer due to the rotations restricted by the Dirichlet boundary condition for the microdeformation $\bar{\chi}_{M12} = \bar{\chi}_{M21} = 0$ on $\partial \mathcal{B}_D^m$. Apparently, the component $\bar{\chi}_{M12}$ is much more pronounced than it is the component $\bar{\chi}_{M21}$. Thus, the micropolar restriction assuming a skew-symmetric microdeformation is not valid and will be skipped in the sequel.

Featuring now a shear test for the rotated microtopology and having in mind to illustrate the micromorphic deformation behaviour, the macroscopic deformation state, i. e. $\text{GRAD } \mathbf{u}_M$, $\bar{\boldsymbol{\chi}}_M$ and $\text{GRAD } \bar{\boldsymbol{\chi}}_M$, predicted by the micromorphic two-scale approach and observed in the bending free center of

the macroscopic sample, has been projected to the boundary of the attached rotated microvolumina cf. fig. 10.2. For fig. 10.4, an assembly of 3 pairs of microvolumina has been merged. Obviously, the particular microvolumina can be connected periodically. The dash-dotted lines indicate the boundaries of the deformed unit cells. On the right hand side, a corresponding detail taken from an analogous reference computation is displayed.²

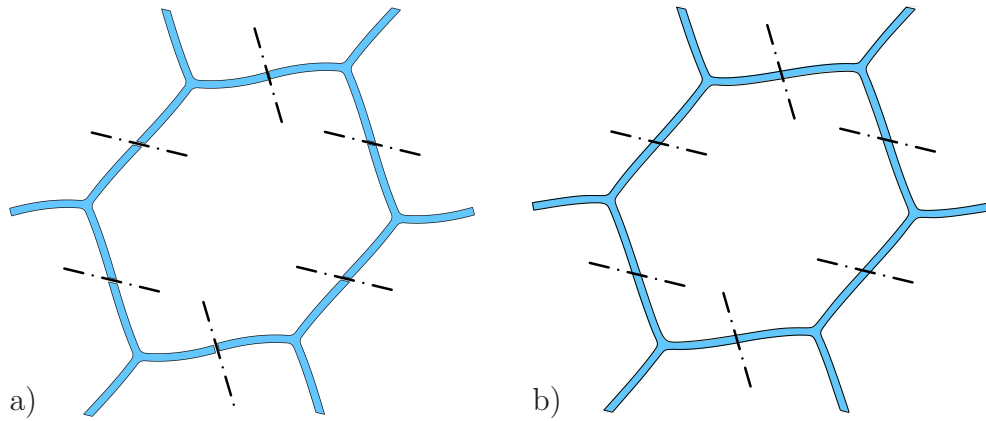


Figure 10.4: Shear test in X_{M1} -direction for the honeycomb microstructure rotated by 90° , deformation state in the bending-free center of the sample ($n = 8$). a) Periodic assembly of 3 pairs of microvolumina (cf. fig. 10.1) loaded with the observed macroscopic deformation state making use of the projection polynomial. b) Detail taken from the corresponding reference calculation.

In the reference solution fig.10.4 b), the main deformation processes take place by a S-shaped bending of the horizontal struts. The same characteristic is predicted by the two-scale approach fig. 10.4 a). Altogether, the high agreement between both deformation pictures may indicate that the micromorphic two-scale methodology, in combination with the modified set of microvolumina, comprises the essential deformation mechanisms due to microstructural periodicity.

So far, only qualitative investigations have been accomplished. In the sequel, the significance of the results predicted by the micromorphic two-scale approach have to be verified. Thus, let us start to examine the shear test in X_{M1} -direction quantitatively. As it has been done for the single-cross microstructure, the normalised surface tractions $\|t_1^{III}\|$, observed at boundary III within the micromorphic two-scale calculations, will be compared to

²A similar deformation behaviour has been predicted by Gibson and Ashby [50].

these ones of the first order approach as well as to those ones of the reference calculations. The microvolumina are furthermore chosen in accordance to fig. 10.2.

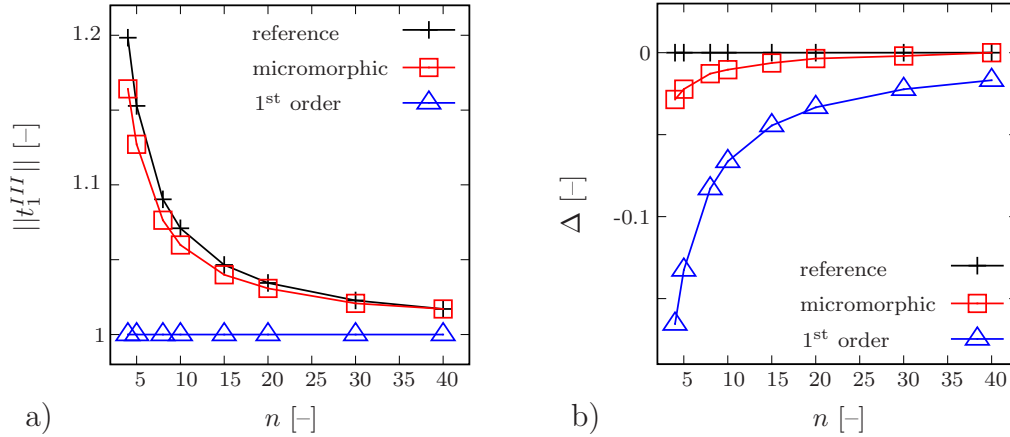


Figure 10.5: Shear test in X_{M1} -direction for the unrotated microstructure. a) Normalised traction at surface III . b) Relative error of the FE^2 calculations in comparison to the reference solution.

Similar to the single-cross structures discussed in chapter 8, the given microstructure exhibits a stiff boundary layer effect due to the rotations of the struts restricted by the Dirichlet boundary conditions. For $n = 4$, the stiffening effect accounts for about 20% and decays with an increasing sample size. Again, the first order model is not able to describe any bending and therewith any stiffening effect, but the first order characteristic converges towards the reference solution with an increasing sample size and reaches an error of about 3% for $n = 40$. By contrast, the micromorphic model is able to reproduce the reference calculation rather exactly. For $n = 4$, it underestimates the exact result by about 3% whereas for larger samples, the error is much smaller than 1%.

Subsequently, performing the shear test for the microstructure rotated by 90° , one finds a very similar situation, cf. fig. 10.6. The reference solution features a stiff boundary layer. For $n = 4$, the stiffening effect accounts for about 30%. Thus, the effect is more pronounced than it is for the unrotated structure. Besides the absolute values of the shear stresses, which are not denoted here, this difference in the boundary layer effect indicates, unsurprisingly, the honeycomb structure to be anisotropic. More precisely, the 90° rotation does not activate the 120° symmetry of the honeycomb structure.³

³The absolute plateau value ($n \rightarrow \infty$) of the shear stress of the unrotated structure is

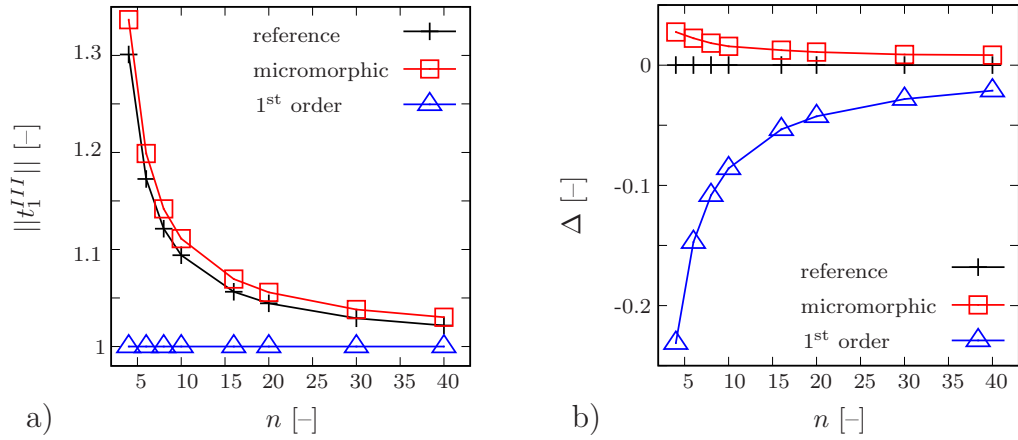


Figure 10.6: Shear test in X_{M1} -direction for the rotated microstructure. a) Normalised traction at surface III . b) Relative error of the FE^2 calculations in comparison to the reference solution.

Regarding the two-scale calculations, one observes the first order approach not to describe the stiffening effect but converging towards the reference solution for large samples. The micromorphic model now slightly overestimates the exact result by about 2% for $n = 4$. With increasing sample size, this error decays and accounts for less than 1% for $n = 40$.

Note that the found anisotropy corresponds to the results found in [107, 119] responding to [27, 28]. In these contributions, it has been figured out that the parameters of a centro-symmetric Cosserat material do depend on the microtopological orientation of the honeycomb structure. One may amend at this point that the honeycomb structure, following the missing skew-symmetry of the microdeformation tensor, does not allow for any micropolar modelling at all, i. e. the kinematics of the Cosserat continuum theory does not satisfy the micromechanical deformation mechanisms of the honeycomb structure.

10.3 Tension test

Let us secondly consider the uniaxial tension test. Again, we assume an infinitely large domain $L \rightarrow \infty$, whereas $h = nl/2$ or $h = n\sqrt{3}l$, respec-

about two times stiffer than it is the structure rotated by 90° .

tively. In fig. 10.7, the results of the two-scale calculations are compared to the reference solution.

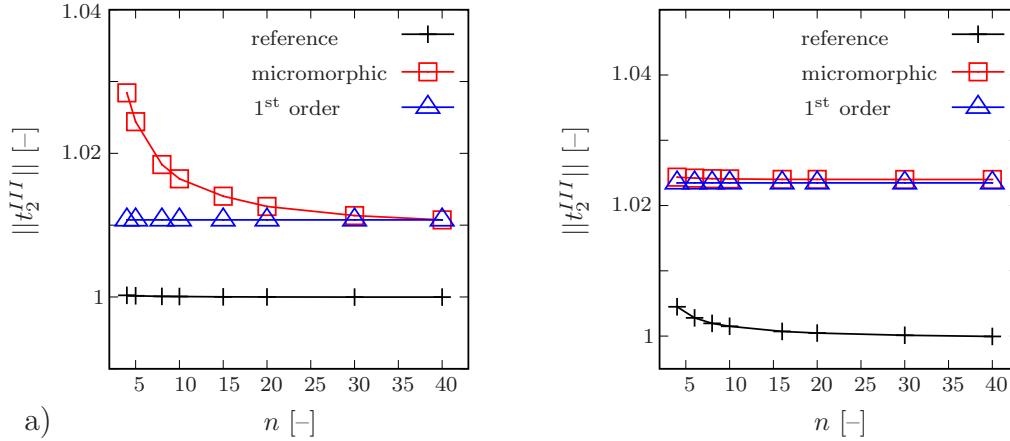


Figure 10.7: Tension test in X_{M2} -direction. Normalised tensile traction at surface III , a) unrotated, b) rotated state.

Whereas the reference calculation exhibits a subordinate stiffening effect for small sample sizes below 0.5 %, the first order two-scale model features a scale invariant tension stiffness, overestimated by about 2.5 %. For the unrotated situation, the micromorphic model predicts a certain stiffening effect whereas it is nearly scale invariant for the rotated situation. But altogether, the error is smaller than 3 % and the two-scale solutions may still considered to be rather exact.

10.4 Bending test of a sandwich structure

After the, at least in the X_{M1} -direction, homogeneous shear and tension tests, the honeycomb structure will now be subject to a clearly inhomogeneous experiment. In the preceding experiments, it has been pointed out the structure to undergo a significant boundary layer effect, if the macroscopic dimensions of the sample are chosen comparable to the microscopic length scale and if the boundary conditions restrict microstructural rotations. Besides the shear test, a further experiment, featuring a certain technical relevance, is the bending test of a sandwich composite consisting of at least one cellular core and an appropriate number of thin, compact surface sheets. From the physical point of view, the cellular kernels support the structure as spacers,

which ensure two neighbouring sheets not to buckle or to come into contact. With a view to light-weight construction, it is meaningful to reduce the dimensions of the sample. A stiffening effect within slender kernels could result in a higher effective bending stiffness with respect to the weight of the composite structure.

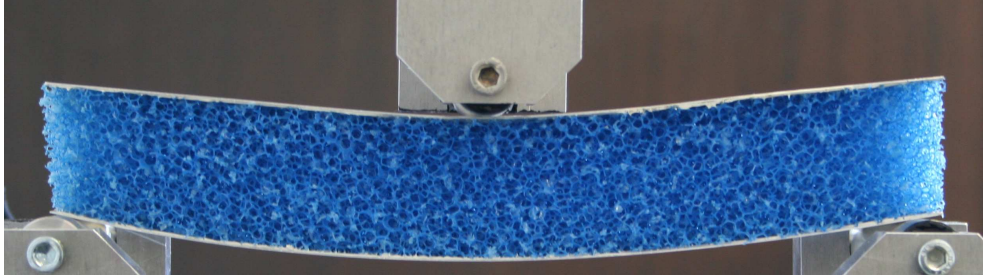


Figure 10.8: Three-point bending experiment of a sandwich panel consisting of thin Aluminium surface sheets and an open-cell Polyurethane core.

Of course, it can not be the aim of the present contribution to find an optimal dimensioning of sandwich panels under certain loading conditions. But in the sequel, the power of the proposed micromorphic two-scale methodology to describe the underlying micromechanical effects will be demonstrated. For that purpose, let us restrict to the most simple case of a sandwich structure consisting of one cellular kernel of variable thickness, covered by two compact sheets. The sheets are assumed to be of the same material as the cellular struts.⁴

The experimental setup is given in fig. 10.9 in a schematic way. The thickness of the surface sheets is assumed to equal $d = 5b$, where b defines the thickness of the microstructural struts, cf. fig. 10.1. Apart from the additional surface sheets, the boundary conditions are chosen in correspondence to the definition given in fig. 8.2: Surface *I* is fixed ($\mathbf{u}_M^I = \mathbf{0}$, $\bar{\chi}_{M12}^I = \bar{\chi}_{M21}^I = 0$), surface *IV* is subject to the displacement $u_{M2}^{IV} = \bar{u} = 0.01L$, whereas $u_{M1}^{IV} = 0$ and $\bar{\chi}_{M12}^{IV} = \bar{\chi}_{M21}^{IV} = 0$, i. e. one assumes symmetry condition. Surfaces *II* and *III* are left unloaded.

From the numerical point of view, the question arises how to model the given composite structure. On the one hand, the honeycomb kernel requires the micromorphic macromodel to be applied, on the other hand, the surface sheets are considered to be compact, i. e. without any microscopic substructure

⁴Note again that the choice of the particular materials is not the matter of the present work but the influence of the microtopology on the effective material behaviour.

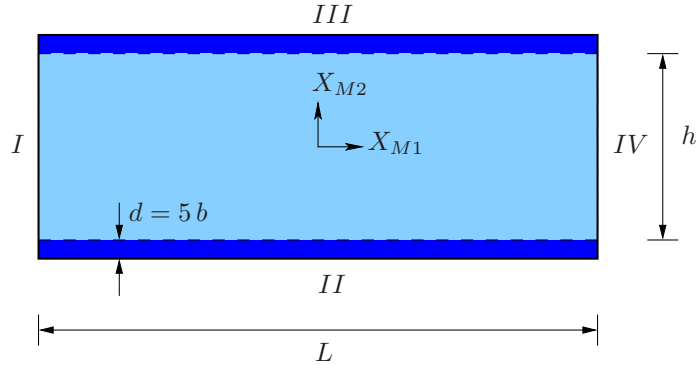


Figure 10.9: Sketch of the macroscopic geometry and assignment of the boundaries.

comparable to the size of the sheet itself. Having in mind the geometrical interpretation of the extended degrees of freedom, one may model the surface sheets via the micromorphic homogenisation procedure. But nevertheless, it is absolutely not clear how to transfer the extended degrees of freedom between the two materials. The interpretation of the microdeformation is strictly coupled with the underlying microtopology, i. e. it is not comparable for the compact sheet and the cellular kernel. However, from the physical point of view, the microstructural rotations should be expected to be suppressed at the kernel-sheet interfaces.

In order to circumvent the transition of the microdeformation components between the two materials, the numerical implementation combines the Cauchy continuum modelling using Hooke's law for the compact sheets and the micromorphic two-scale modelling for the cellular kernel. Introducing a formulation which is dealing with a penalty multiplier λ , the microdeformation is constrained to equal the identity within the surface sheets. Details may be found in appendix C.

Let us start again with a qualitative comparison between the reference calculations on the one hand, and the two-scale calculations on the other hand. The underlying dimensions of the bending test are defined as follows:

$$L = 32\sqrt{3}l, \quad h = 12l.$$

The observed deformation pictures of the reference solution and the micromorphic one are given in fig. 10.10. It may be found both results to describe the same macroscopic deflection. Furthermore, one should notice the micro-

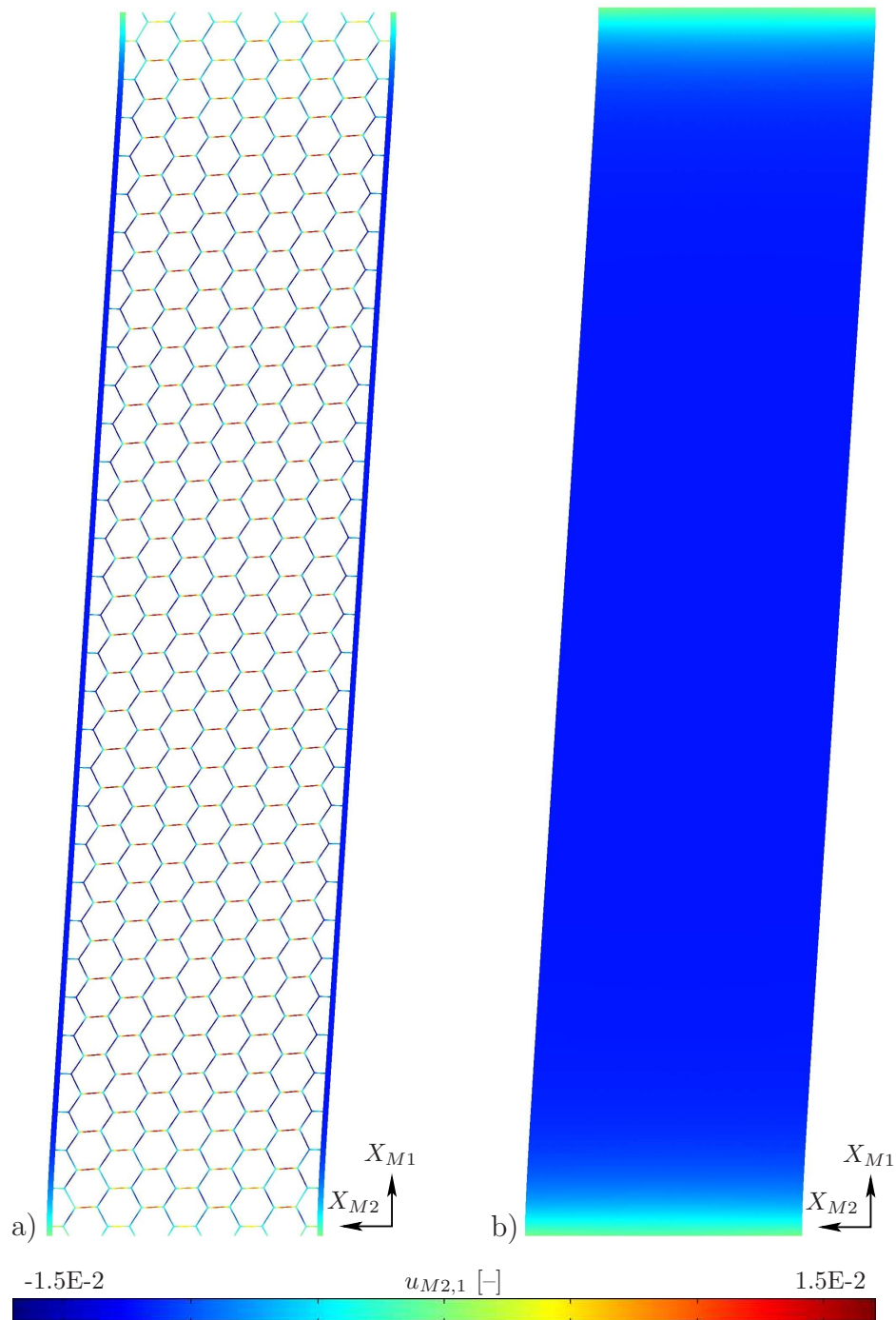


Figure 10.10: Picture of the sandwich bending test, gradient $u_{M2,1}$ of the deflection in longitudinal direction. a) Reference calculation, b) micromorphic two-scale calculation. Note the boundary conditions chosen for the numerical experiment to differ from those in fig. 10.8.

structural fluctuations within the picture of the reference calculation. Due to local effects, there are areas of a positive and a negative value of the shear deformation plotted in fig. 10.10. By contrast, the homogenised solution is absolutely smooth. Here, the physical meaning of the word *homogenisation* becomes apparent. It may be considered as the most important requirement on any homogenisation method to smooth all the microstructural effects without losing the microtopological information. Obviously, the micromorphic homogenisation scheme fulfils this condition in a much more precise way than it does the first order homogenisation methodology. In fig. 10.11, the deflection line gradients of the reference, the micromorphic and the first order calculation, observed within the surface sheets, are compared. Whereas the micromorphic deflection gradient can not be distinguished from the reference, the first order solution exhibits an absolutely different bending characteristic. In contrast to the reference and the micromorphic solution, the deformation process is concentrated very close to the boundary. From the physical point of view, this result does not surprise anymore. The first order approach does not describe the boundary stiffening due to restricted rotations. The region close to the boundary is estimated too soft and, consequently, the deformation process can not be displayed in an adequate manner.

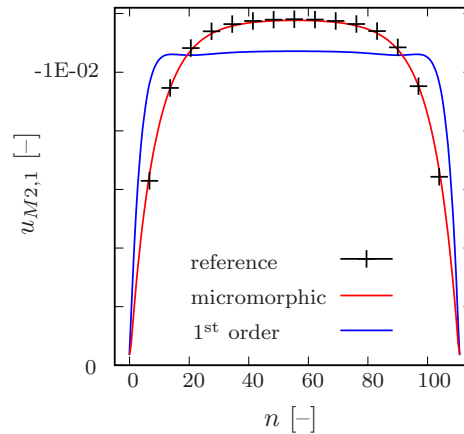


Figure 10.11: Deflection lines observed in a compact surface sheet in comparison between the reference, the micromorphic and the first order two-scale methodology.

In order to illustrate the inhomogeneity of the deformation state within the above mentioned bending test of the sandwich structure, the microdeformation components as well as a selection of the microdeformation gradient components can be found displayed in figs. 10.12 – 10.14. Note that, due to the introduction of the penalty formulation cf. appendix C, all extended

quantities vanish within the surface sheets. Thus, the rotation of the microstructural struts is ensured to be suppressed at the interface between the cellular kernel and the compact surface sheets.

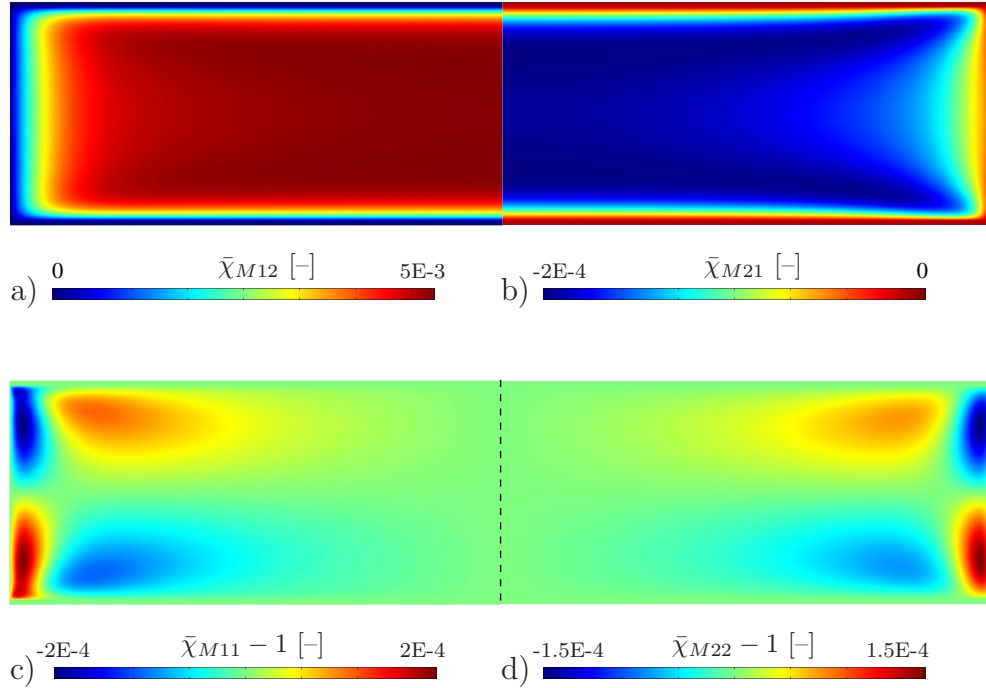


Figure 10.12: The four components of the microdeformation tensor $\bar{\chi}_M$ observed in the sandwich three-point bending test.

Consequently both, the interfaces between the kernel and the hard boundaries I and IV as well as those ones between the kernel and the surface sheets, cause boundary layers and microstructural bending effects. But one should remark the bending mechanisms, i. e. the particular bending deformation modes, to differ between the two types of interfaces due to their orientation with respect to the external loading, cf. figs. 10.13 and 10.14. One should furthermore notice that the distinct inhomogeneity of the sandwich bending activates the microstrain components $\bar{\chi}_{M11}$ and $\bar{\chi}_{M22}$, cf. fig. 10.12 c) and d), which are of the same order of magnitude as the microshear deformations, especially close to the cross-over of the two different boundary layers. This microstrain character is, besides the missing skew-symmetry of the microdeformation tensor, a further hint that the modelling of honeycomb structures applying a micropolar (Cosserat) continuum formulation must fail.

Finally, let us conclude the numerical investigations of the regular honeycomb structure by varying the height h of the composite structure, whereas the

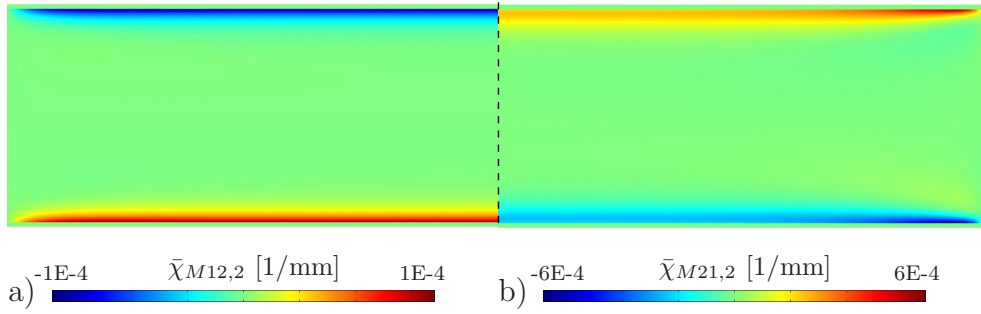


Figure 10.13: The gradients of the microshear deformation components with respect to the X_{M2} -direction.

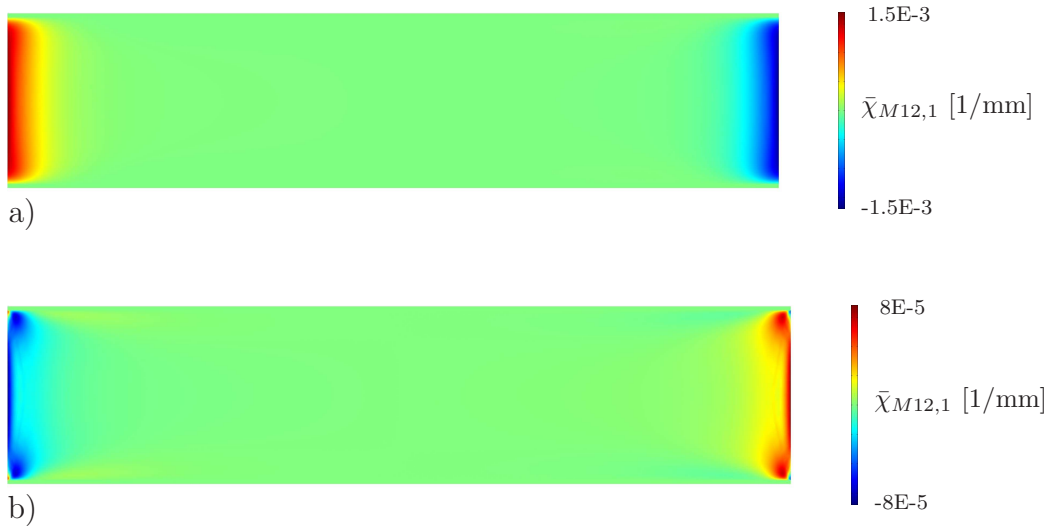


Figure 10.14: The gradients of the microshear deformation components with respect to the X_{M1} -direction.

length L as well as the thickness of the surface sheets d is kept constant. In order to point out the high effective bending stiffness of the composite structures, a comparison to a set of compact samples has been drawn. These compact samples consist of the same material as the surface sheets and the microscopical struts. Their geometry is defined by the length $L = 32\sqrt{3}l$, identical to the sandwich structures. The absolute height of the compact samples has been chosen in a way that their particular mass corresponds to that one of the sandwich counterpart. In fig. 10.15, the reaction force in X_{M2} -direction, integrated over boundary IV , i. e. RF_{M2}^{IV} , has been observed and divided by that one of the appropriate compact sample, called RF^* . On the left hand side of fig. 10.15, the result is plotted versus the height h of the sample. On the right hand side, the relative error of the FE²-calculation is

given with respect to the reference solution.

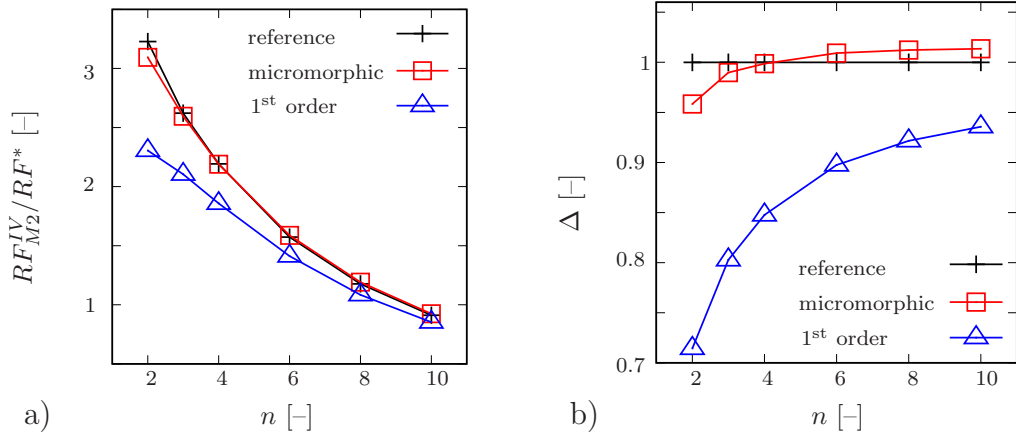


Figure 10.15: Bending test of the sandwich structure ($L = 32\sqrt{3}l$, $h = n3/2l$, $d = 1/3l$). a) Reaction force in X_{M2} -direction observed at surface IV , normalised with respect to a compact sample of the same mass. b) Relative error of the FE^2 calculations in comparison to the reference solution.

Let us at first discuss the results of the reference calculations. For very thin cellular core layers, we find the sandwich structure to exhibit an effective bending stiffness about three times higher than that one of the compact sample ($n = 2$). This advantage is decaying and finally, the sandwich structure becomes softer than the compact sample ($n > 10$). Considering now the first order computations, one finds a qualitatively similar behaviour. Nevertheless, the relative error of the first order solutions accounts for up to 30% for $n = 2$ and decreases for a larger kernel thickness. By contrast, the micromorphic two-scale approach is displaying the microstructural deformation processes in a very exact way. Thus, even for the most slender kernel layer ($n = 2$), the relative error only accounts for about 4%. For larger samples, the predicted results converge towards a relative error of about 1.5%. Having in mind the first order FE^2 approach not to deal with microstructural bending effects, this relative aberration between the first order and the micromorphic two-scale computations allows to estimate the influence of the microstructural bending effects on the absolute stiffening for slender sandwiches. Consequently, only about 30% of the 300% stiffening ($n = 2$) can be explained by microstructural boundary layer effects. Thus, different mechanisms have to be taken into account to describe this particular behaviour.⁵

⁵Note that the given bending experiment has been introduced to verify the micromorphic two-scale methodology. The particular stiffening behaviour of the reference structure

10.5 Discussion

Let us conclude the investigations concerning the regular honeycomb structure with a brief summary of the found results.

- Already the results found in chapter 6 have indicated the description of the honeycomb structure as a 2-particle system to fail within the micromorphic homogenisation procedure. For that purpose, an alternative formulation of the honeycomb unit cell has been developed by dividing it into two mirrored parts. Consequently, the effective picture of the honeycomb structure may be interpreted as the arithmetic average of its two kinds of vertices, differing only in their orientation.
- In the following, several numerical experiments have been accomplished. It has been pointed out that it is insufficient from the micromechanical point of view to describe the honeycomb structure's deformation processes by a micropolar (Cosserat) macrotheory. The microdeformation must be assumed neither skew-symmetric nor free of microstrain effects.
- The extended homogenisation method has been subject to different quantitative investigations. It has been demonstrated the methodology to describe the micromechanical deformation processes in a very high accordance to, at least in one direction, homogeneous reference experiments.
- A further study has been concerned to the description of composite structures. Even for the highly inhomogeneous sandwich bending test, it has been proved the proposed methodology to predict the results found by the reference computations in a quality which is, in the author's opinion, more than acceptable.

It is maybe the most fundamental result of the preceding studies that it is possible to reduce a system, which is commonly interpreted as a 2-particle system, cf. [107, 119], to an 1-particle system by combination of the particular vertices. In the future, that superposition methodology may allow for the micromorphic modelling of realistic three-dimensional structures based on an exact knowledge of the underlying micromechanical processes.

is not subject to further investigations within the present contribution.

11

Auxetic structures

Concluding the numerical investigations within the present work, the complexity of the underlying microtopologies undergoes a further increase taking into account so-called auxetic materials. This class of materials is commonly interpreted to exhibit a lateral expansion during stretching processes and a contraction during compression, i. e. a negative Poisson's ratio. Typical examples are e. g. structures with inverted cells, re-entrant or enfolded foams, cf. [10, 15, 36, 46, 50, 83]. Thus, keeping the connectivity unchanged, the basic symmetry of the unit cells is modified. In fig. 11.1, a folded honeycomb structure is depicted. Alternatively, it is possible to assume the basic geometry to be maintained, i. e. the position of the vertices compared to their neighbours, but the shape of the connecting struts to feature undulations. In fig. 11.2, the unit cell of the single-cross microstructure is depicted where the struts exhibit an S-shape.

Apparently, one has to expect a complex microstructural deformation behaviour for both structures, if they undergo stretching conditions. Whereas the enfolded honeycomb structure fig. 11.1 should show bending deformations within the connecting struts, one may predict rotations of the vertices for the undulated single-cross fig. 11.2, depending on the bending stiffness of the struts.

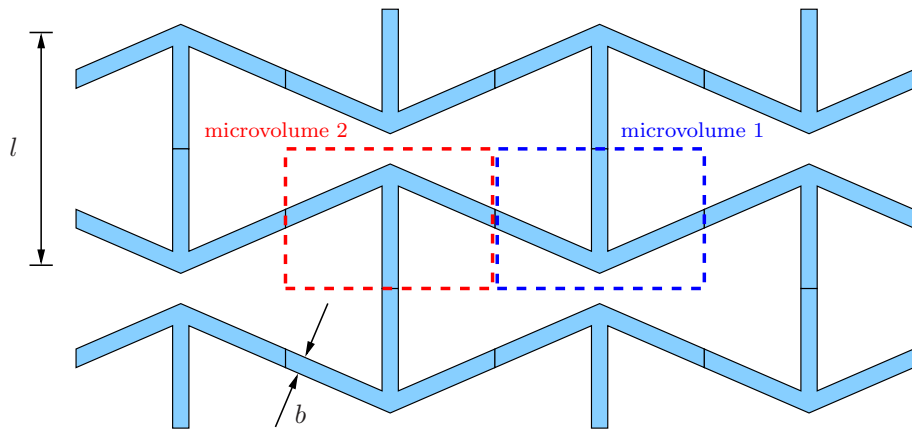


Figure 11.1: The folded honeycomb structure ($b/l \approx 1/15$).

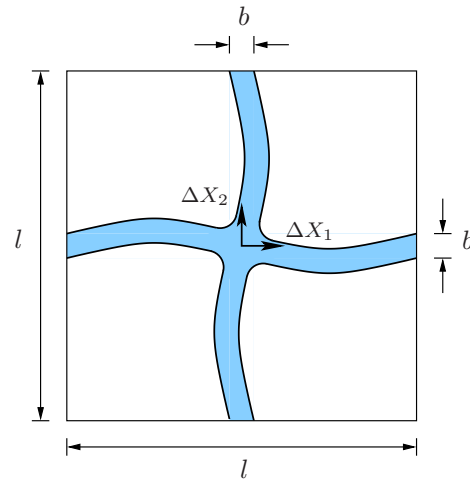


Figure 11.2: The unit cell of the undulated single cross ($b/l = 1/15$).

In the following sections, the micromechanical deformation mechanisms and their representation by the extended FE²-methodology will be investigated in detail.

11.1 Folded honeycomb

In analogy to the regular honeycomb structure presented in the preceding chapter, the folded honeycomb may also be reduced to an 1-particle system

for the micromorphic two-scale modelling, cf. fig. 11.3.

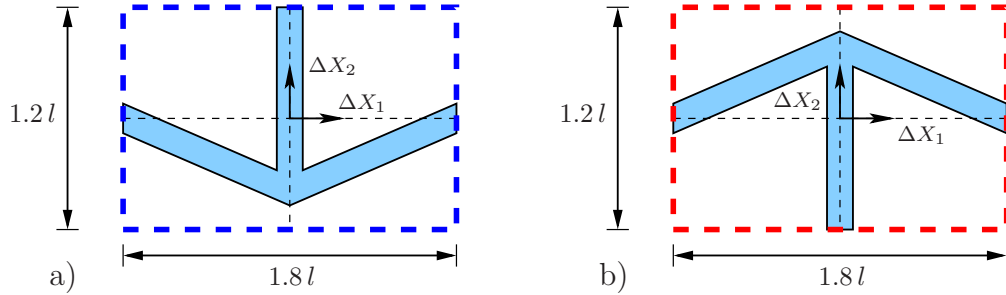


Figure 11.3: Detail from fig. 11.1: One pair of microvolumina featuring one unit cell of the investigated folded honeycomb microstructure.

In the following numerical experiment, the given structure is subject to a tension test in X_{M2} -direction, cf. fig. 8.2, $h = n 1.2l$, $L \rightarrow \infty$, where l denotes the length of the microstructural struts. Instead of observing the lateral expansion, which is suppressed due to the infinite size of the sample in X_{M1} -direction, the traction normal to surface IV has to be taken into account.¹ In fig. 11.4, both, the surface traction in stretching direction as well as in lateral direction are depicted. Apparently, the auxetic character of the structure comes into play and results in a negative lateral surface traction, i. e. the stretching in X_{M2} -direction causes a compression in X_{M1} -direction. Both surface tractions are predicted by the micromorphic homogenisation procedure with a certain exactness.

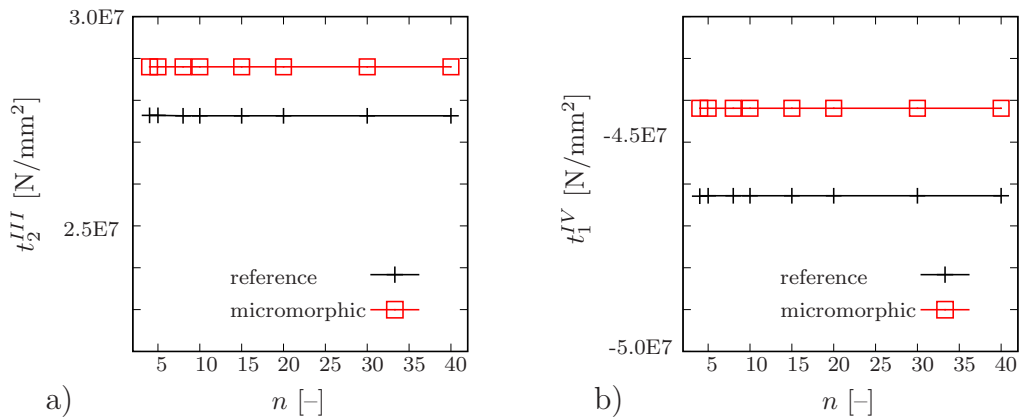


Figure 11.4: Tension test in X_{M2} -direction. a) Tensile traction at surface III . b) Tensile traction at surface IV .

¹Surface IV can be interpreted as a cutting line.

But one may notice as well that the given auxetic experiment does not exhibit any boundary stiffening or softening, i. e. the surfaces do not induce any bending effects. This observation can be clarified if one reminds the surface-induced bending effects to depend on a restricted rotation of microstructural struts connected to the boundary. In the given experiment, no microscopic rotations of the vertical struts are activated. Consequently, it should be possible to display the observed effect as well by a first order two-scale approach.

11.2 Undulated single-cross

Let us now focus on the second auxetic microstructure, proposed in fig. 11.2, the undulated single-cross. In difference to the folded honeycomb structure, the auxetic mechanism now results from the S-shape of the connecting struts instead of a vertex shifting. One may imagine the struts to bend and the vertices to rotate in consequence even if the structure is subject to an axial stretching condition. Furthermore, remembering the micromorphic degrees of freedom exactly to describe the rotations within the connecting struts, one may expect, apart from a very complex microscopic deformation behaviour, certain boundary layer effects for this second auxetic microstructure.

11.2.1 Tension test

Let us start with the examination of a numerical tension test in X_{M2} -direction ($h = nl, L \rightarrow \infty$). Note again the domain to be infinite in X_{M1} -direction. The auxeticity will be verified observing the lateral traction t_{M1} parallel to surface *III*. At first, the character of the microdeformation field within the sample will be studied in a qualitative way. For that purpose, the various components of the microdeformation tensors are depicted in figs. 11.5 and 11.6. Regarding fig. 11.5, one may notice at first the microstrain deformation components not to be of minor significance but, at least $\bar{\chi}_{M22}$, to account only for one order of magnitude smaller than the microshear deformation components depicted in fig. 11.6. Remember that there are no boundary conditions at all for $\bar{\chi}_{M11}$ and $\bar{\chi}_{M22}$ but only $\bar{\chi}_{M12} = \bar{\chi}_{M21} = 0$.

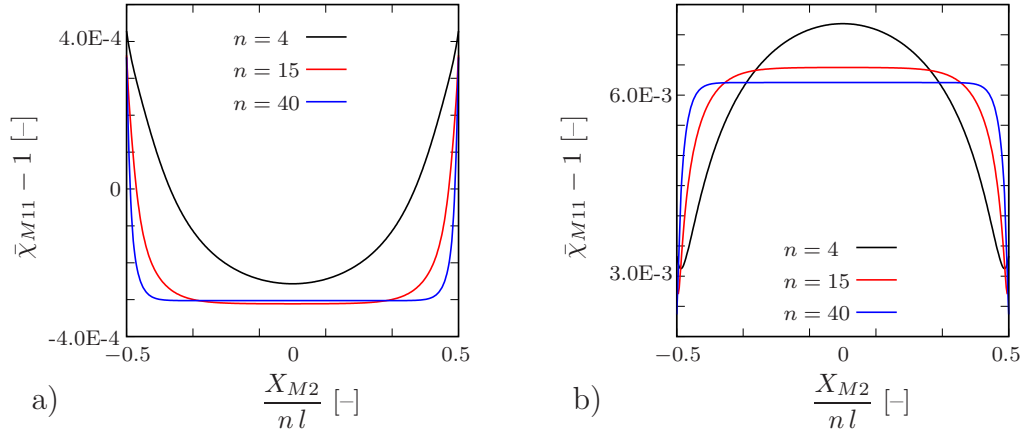


Figure 11.5: Microstrain deformation components during the tension test.

Nevertheless, one may observe a distinct boundary layer for those components featuring a constant thickness if increasing the macroscopic height h . Consequently, the microstrain deformation components must couple in an inherent way with the microshear components depicted in fig. 11.6. But this inherent coupling between the microstrain and the microshear deformation modes is not restricted to the bending dominated boundary layer but also becomes apparent in the center of the sample.

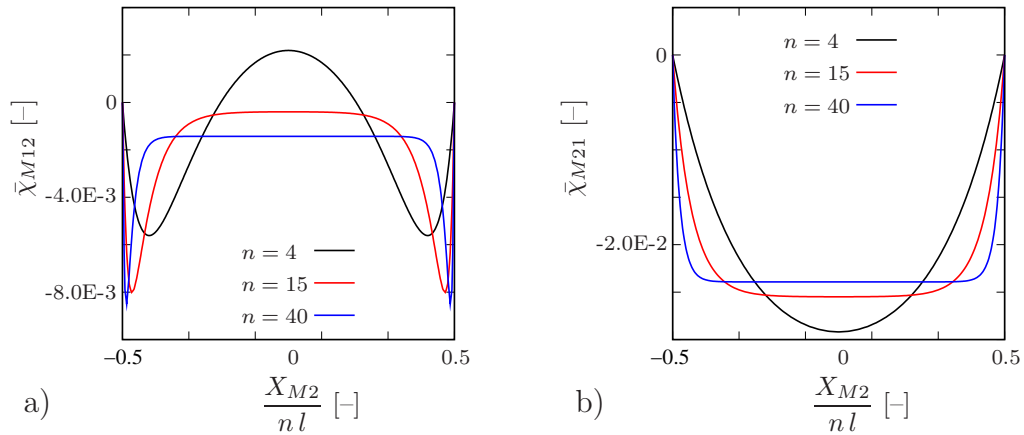


Figure 11.6: Microshear deformation components during the tension test.

Different from the deformation behaviour under tensile conditions of the regular single-cross microstructure discussed in chapter 8, the S-shape of the microstructural struts activates the microshear deformations even under the given loading conditions. This effect can be explained taking into account the reorientation processes during stretching, i. e. the undulated struts start to unfold which causes a rotation of their intersections at the boundary of

the microvolume as well as a rotation of the central vertex. But the rotation of the intersections can only be enabled by the microshear deformations. The rotation of the top and the bottom boundaries of the unit cell depicted in fig. 11.2 are coupled to the microshear component $\bar{\chi}_{M21}$, the rotation of the left and the right boundary to the component $\bar{\chi}_{M12}$, cf. fig. 5.1. The fact all components of the microdeformation tensor to be activated, indicates the system to require the full micromorphic macrocontinuum and does not allow for any restriction of the extended kinematics.

Let us now investigate the quality of the exactness of the results predicted by the micromorphic two-scale approach. In fig. 11.7, the traction t_{M2} normal to surface *III*, i. e. in stretching direction, is displayed, whereas fig. 11.8 shows the traction t_{M1} parallel to surface *III*.

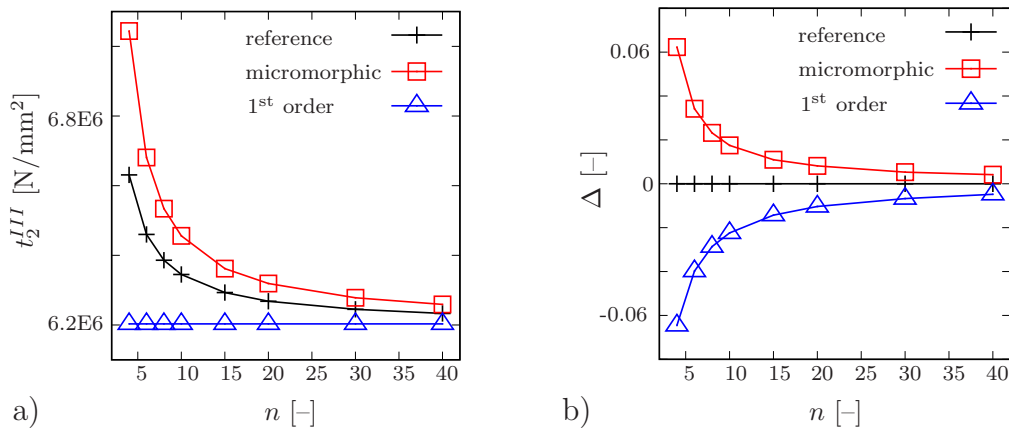


Figure 11.7: Tension test in X_{M2} -direction. a) Tensile traction at surface *III*. b) Relative error of the FE² calculations compared to the reference solution.

Firstly taking into account the normal stress one finds, in contrast to the undulation-free single-cross discussed earlier, a stiff boundary layer of about 6.5% for $n = 4$ in the reference calculation. Again, the first order solution is not sensitive for bending effects and predicts a tensile stress constant for the various sample sizes h . With increasing h , the first order converges towards the reference results. By contrast, the micromorphic approach predicts a stiff boundary layer. But the absolute values of the predicted results overestimate the reference solution. Especially for small sample size ($h = 4$), the relative error accounts for the same order of magnitude as the stiffening effect itself. Similar to the first order approach, the micromorphic calculations converge towards the plateau stress for large samples.

Let us proceed towards the shear stress resulting from the stretching loading conditions, cf. fig. 11.8. The auxeticity becomes apparent if one considers the negative value of the shear stress. Furthermore, one finds the shear stress to exhibit a soft boundary layer. For $n = 4$, the resulting shear stress is about 12% softer than the plateau value for very large samples. Not surprisingly, the first order FE² methodology is not able to predict this softening effect. By consequence, it is meaningful to assume the softening effect to be caused by bending effects. Regarding the micromorphic prediction, one finds the softening effect to be overestimated with up to 9% for $n = 4$. Therefore one may derive that the micromorphic two-scale approach is not able to meet the auxetic boundary effects in a precise way although the effects are predicted correctly in a qualitative manner.

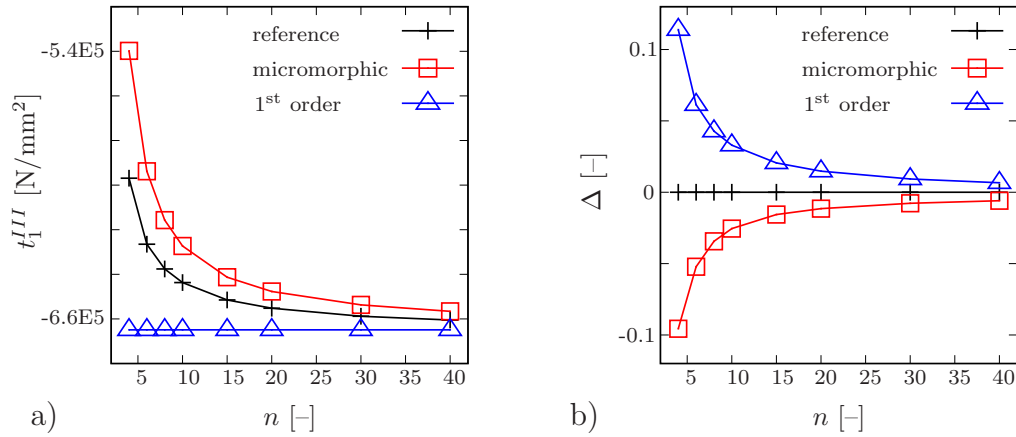


Figure 11.8: Tension test in X_{M2} -direction. a) Tensile traction at surface III . b) Relative error of the FE² calculations compared to the reference solution.

11.2.2 Shear test

Analogously to the investigations in chapter 8 and 10, the proposed microstructure will be subject to a shear test of the infinite domain ($h = nl, L \rightarrow \infty$). Prior to the quantitative evaluation of the results achieved by the two-scale approach, let us consider the predicted microdeformation at first. Whereas fig. 11.9 shows the microshear components of the microdeformation tensor, fig. 11.10 concentrates on the microstrain components for various sample sizes n . Again, the microshear deformations are suppressed

at the top and the bottom boundaries, whereas the microstrain deformations are left unrestricted.

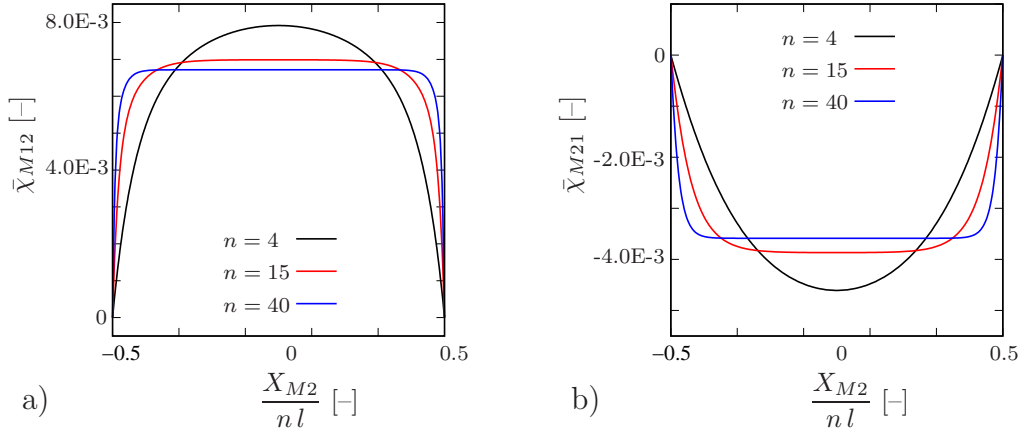


Figure 11.9: Microshear deformation components during the shear test.

Consequently, we find the boundary layer of the microshear deformations in fig. 11.9 similar to those detected for the regular single-cross structure, cf. fig. 8.3 a). But analogous to the tension test, no skew-symmetry can be detected for the microshear deformation.

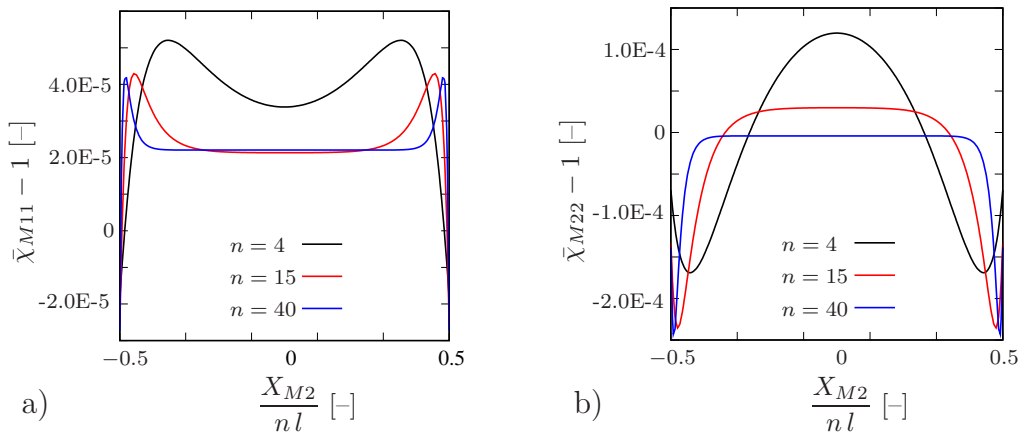


Figure 11.10: Microstrain deformation components during the shear test.

Bringing now the microstrain deformations into play, one may observe that, vice versa to the tensile loading, the macroscopic shear deformation induces a microstrain deformation, i. e. microcompression modes of the microvolumina, depending how close to the boundary they are. Furthermore, the characteristic of the microstrain components over the height of the sample is very peculiar. Whereas the usual boundary layer effects converge continuously

towards a plateau with increasing distance from the boundary, this is not the case for the microstrain components. By contrast, they run through an extremum before reaching the plateau in the center of the sample. This complex behaviour is solely dominated by the boundary condition for $\bar{\chi}_{M12}$ as well as for $\bar{\chi}_{M21}$ and, therefore, indicates anew the inherent coupling between shearing and stretching microdeformation modes.

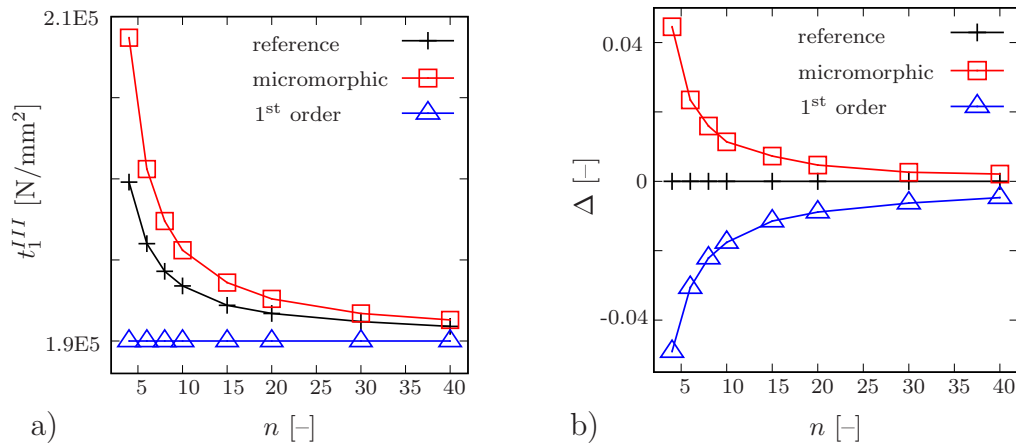


Figure 11.11: Shear test in X_{M1} -direction. a) Shear traction at surface III . b) Relative error of the FE^2 calculations compared to the reference solution.

Skipping now the qualitative considerations, one may compare the results computed using the two-scale algorithm in comparison to the reference as well as to the first order FE^2 calculations in a quantitative manner. In fig. 11.11, the shear stress is displayed, i. e. the traction t_{M1} parallel to surface III . The given microstructure describes a stiff boundary layer under the shear condition and the stiffening effect accounts for about 5 % for $n = 4$. Whereas the first order FE^2 solution results in the plateau stress for large samples sizes h , the micromorphic two-scale calculation overestimates the stiffening effect by about 4 % for $n = 4$. The error decays with an increasing sample size. Hence, for small samples, we find the error caused by the method to be of the same order of magnitude than the boundary layer effect itself.

Evaluating the tensile stress depicted in fig. 11.12, i. e. a compressive stress, we find very similar to the tensile experiment a soft boundary layer effect which accounts for about 12 % for $n = 4$. Besides the plateau stress given by the first order approach, the micromorphic methodology results in a too soft solution, i. e. the softening effect is overestimated by about 9 % ($n = 4$). The most peculiar effect is the coherence between the shear stress under tensile

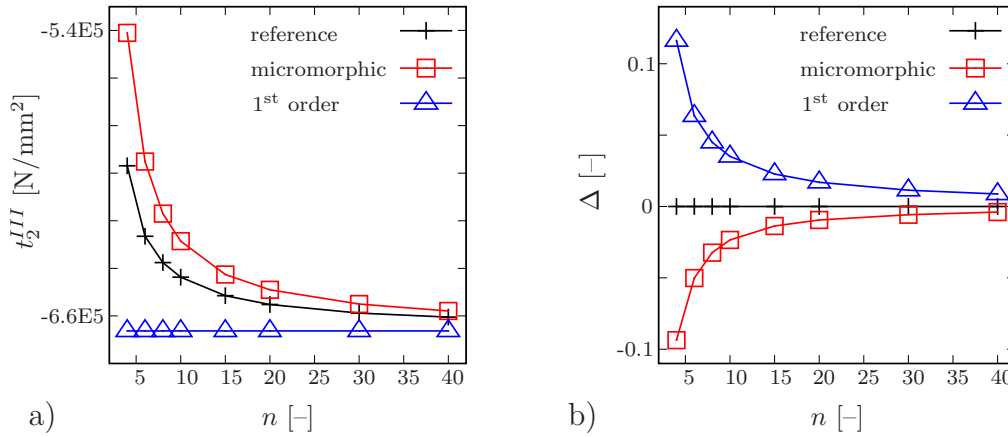


Figure 11.12: Shear test in X_{M1} -direction. a) Shear traction at surface III . b) Relative error of the FE^2 calculations compared to the reference solution.

loading, cf. fig. 11.8, and the compressive stress under shear deformation, cf. fig. 11.12. Apparently even for the reference solution, both characteristics are identical. This special effect seems to be a consequence of the coupling between the shear and the strain properties of the material. The question, which will not be discussed furthermore, arises, if that is a special case or a general feature of this class of auxetic materials.

11.3 Discussion

At the end of the present chapter concerning the negative Poisson's ratio effect, let us briefly review the found results.

- The first example has been up to the description of a honeycomb structure with inverse cell walls. Stretching the microstructure, the cell walls are able to unfold which causes an effective expansion in lateral direction. In the presented case, the lateral expansion has been suppressed and the compression stress has been observed. It has been pointed out the deformation to take place by bending the lateral struts, i. e. the struts, which are not parallel to the chosen loading direction. By contrast, the vertical struts and the struts connected to the boundary conditions among those do not account for any bending process. Consequently, no rotations are activated within the vertical struts and the

suppressed rotation at the boundaries does not restrict the deformation of the system. No boundary layer effects have been observed. Although the micromorphic two-scale approach has predicted the reference results including the auxeticity with an acceptable exactness, it does not offer any advantage compared to the first order two-scale methodology involving periodic boundary conditions under the given loading conditions.

- Secondly, a single-cross microstructure has been the point of interest, whose connecting struts have undergone a S-shape undulation. Both numerical experiments, the tension test as well as the shear test, have exhibited size depending boundary layer effects, besides stiffening effects in the loading direction also softening effects in the cross direction. In comparison to the boundary effects studied in the previous chapters, one may find the amount of the stiffening effect to be much less pronounced.
- The basic microscopic deformation mechanisms result from two related reorientation processes. On the one hand, the external deformations cause the microstructural struts to unfold. Because they are connected rigidly to the central vertices, the unfolding effects the vertices to rotate and to induce a further reaction in the lateral direction at the same time.
- Applying the micromorphic modelling, it has been shown this mutual coupling between stretching and shear deformations to be reflected in the components of the microdeformation tensor as well. In contrast to the regular single-cross structure, where the microstrain deformation quantities have not been activated in any experiment, the deformations of the undulated single-cross require those deformation modes to become apparent. The microstrain deformation in lateral direction can be understood as an inherent consequence of the rotation of the central vertex. No restrictions of the micromorphic kinematics are admissible.
- If not influenced by boundary induced effects, i. e. in the center of sufficiently large samples, the micromorphic methodology is able to predict the deformation processes in a very exact way. Apparently, the cubic projection polynomial within the micromorphic two-scale algorithm is sufficient to reflect all essential periodic deformation processes of the microstructure without taking into account higher order periodic boundary conditions.

- Nevertheless, it has been pointed out the micromorphic two-scale model to predict the boundary layers in a qualitative manner. The particular amount of the stiffening or softening effect has been found overestimated with an error of the same order of magnitude as the stiffening effect, softening effect, respectively. Thus, a further limitation case for the proposed homogenisation scheme has been detected.

Obviously, the bending effects of the real microstructure can not be reproduced by the kinematics of a micromorphic continuum theory of grade one taking into account an affine microdeformation. The logical consequence for this particular case is the further extension of the micromorphic FE^2 scheme to even higher grades.

For the preceding discussion, the auxetic structures may be designated as artificial constructions, whereas e. g. the honeycomb structure can be interpreted as the two-dimensional counterpart of realistic cellular structures. From the physical point of view, the question arises, if auxetic microstructures bear any relevance, i. e. do there exist materials with comparable microscopic properties. E. g. Lakes et al. [46, 83] have succeeded to generate re-entrant metal or polymeric foams applying a heat treatment in combination with incremental plastic deformations. Nevertheless, it seems to be dubious if those materials, i. e. the class of re-entrant and enfolded structures similar to the folded honeycomb structure given above, justify further efforts in the formulation of appropriate higher order homogenisation techniques.

A different material class seems to be more auspicious, namely the wide field of semi-flexible biopolymer networks. The most established representatives of those materials are networks of actin and various further protein filaments which are basic elements e. g. of cell walls and other biological tissues, cf. [72, 80, 85, 112, 113, 117]. Typically, they consist of long flexible components which are linked in vertices. The chains between the links are not free but undulated due to thermodynamical effects. From the mechanical point of view, those materials are of special interest because they feature a strain-stiffening effect, i. e. the strain stiffness increases disproportionately if shearing or stretching the network. The reason can be found in the bending to stretching transformation, cf. e. g. [14]. Whilst at the beginning of the transformation, the chains exist in their undulated form, they are able to unfold, making use of local bending processes until all the chains are reorientated parallel to the external loading.

Against this background, the above mentioned undulated single-cross structure may be interpreted as the most simple case of such a type of network involving a high degree of cross-linking of the chains. Similarly as for the reorientations within the biopolymers, we have observed stretching deformations of the undulated struts to occur even under external shear loading. By consequence, the vertices have been found to rotate. Thus, one may expect similar boundary effects for sufficiently dense and therefore stiff networks.

In literature, further examinations have been accomplished to describe the strain stiffening behaviour making use of micromechanical models and replacing the biopolymer by a network of beam elements. Doing so it has been pointed out the reorientation process, based on local bending effects, to feature a *non-affine character*, cf. [19, 25, 57, 60, 101].

Especially for this bending dominated regime, the micromorphic continuum theory of whatever grade promises to provide a toolbox for the sound description of the complex kinematical processes.

12

Discussion of the methodology

Let us bring the present contribution to its end drawing a final recapitulation of the proposed methodology. It has been the scope of this work to describe the complex effective material behaviour of cellular structures. Special attention has been paid to the modelling of the inherent size depending boundary layers of those structures. For that purpose, the heterogeneous Cauchy microcontinuum, representing the cellular network, has been substituted for a homogeneous micromorphic macrocontinuum in part I, taking into account higher order degrees of freedom. Based on the exact knowledge of the microscopic deformation mechanisms, those degrees of freedom have been expressed in terms of a cubic mean field depending on the macroscopic deformation measures. Hence, an exact geometrical interpretation of the microdeformation and its gradient has been given. Evaluating an energy criterion, i. e. an extended form of the Hill-Mandel condition balancing the macroscopic and the microscopic strain energy rate, an appropriate homogenisation scheme has been elaborated in order to transfer the local stresses to the effective level.

By consequence, the macroscopic deformation state is defining a microscopic Dirichlet boundary value problem on the boundary of the microvolume attached to each macroscopic material point. By homogenisation of the stress

response, the macroscopic constitutive modelling is a priori circumvented. No effective material parameters have to be interpreted on the micromorphic macroscale and the effective material modelling is strictly dominated by the microscopic processes. It has been pointed out that the given algorithm introduces a microscopic length scale in an inherent way by defining the size of the unit cell.

In the second part, the properties of the micromorphic two-scale approach have been subject to various numerical investigations. In chapter 6, the relevance of the higher order deformation modes has been studied within several experiments accounting for microscopic resolution. For that purpose, different periodic unit cells of regular cellular structures have been studied. It has been indicated the micromorphic polynomial to involve all the essential deformation mechanisms, if the attached microvolume comprises exactly one vertex connected to its neighbours via slender struts. In analogy to particle systems it has been mentioned the micromorphic degrees of freedom to lose their physical meaning for $(n > 1)$ -particle systems. This conclusion contrasts fundamentally to the usual procedure within the first order FE² approach. Whereas the micromorphic scheme requires the smallest possible unit cell in order to give a meaningful interpretation of the extended degrees of freedom, the first order technique usually requires large representative volume elements for a correct prediction of the effective material properties. From the numerical point of view, this restriction to very small attached microvolumina surely bears a higher grade of efficiency. But on the other hand, the micromorphic scheme requires a high microstructural regularity.

In chapter 7, the scale transition properties have been taken into account. It has been found the quadratic deformation modes to transfer the microstructural length scale, i. e. the size of the attached microvolume, from the micro- to the macroscale. Again, it should be emphasised that a physically meaningful interpretation of the microstructural length scale requires the size of the microvolume to correspond to the characteristic length scale, usually considered as the characteristic length of the connecting struts. Thus, the quality of a result predicted by the micromorphic two-scale approach strictly depends on the choice of the underlying microvolume size.

In the following chapters 8 – 11, the complete two-scale methodology has been subject to various numerical experiments taking into account a single-cross microstructure including a modification of the central vertex, a honeycomb microstructure and finally two auxetic structures, accounting for a negative effective Poisson's ratio. For the single-cross microstructure, it has

been found the micromorphic two-scale approach to result in a highly exact approximation of the different loading conditions even if applying unloaded Neumann boundary conditions, i. e. free boundaries. The accuracy of the predicted material properties has been pointed out strictly to depend on the aspect ratio of the connecting struts (the smaller the exacter). Similarly, it has been mentioned that the central vertex must not be chosen too large. Furthermore, one should notice that the observed deformation mechanisms feature a more or less skew-symmetric character. Nevertheless, the micropolar restriction on the macroscale has caused a certain systematical error within the observed results. Finally, increasing the size of the microvolume to a 4-particle system, it has been demonstrated the micromorphic modelling not to be meaningful from the physical point of view.

For the honeycomb modelling, the first requirement has been the formulation of appropriate 1-particle microvolumina. This task has been accomplished dividing the periodic unit cell into two parts, only differing in their orientation with respect to the macroscopic base system. In the subsequent numerical experiments, it has been demonstrated that an arithmetic superposition of the microvolumina results in a correct description of the material properties under the different loading conditions. Moreover, the microstructure has undergone the highly inhomogeneous loading conditions as the core material within a sandwich structure.

Maybe the most exciting finding within the mentioned investigations one should remind the microdeformation to exhibit a strong asymmetry even for the perfectly regular honeycomb structure. Having in mind even more complex three-dimensional microstructures, the Cosserat modelling does not seem to be the adequate choice. Consequently, the proposed methodology offers a clear geometrical explanation for this failure of the Cosserat continuum theory discussed in literature earlier, e. g. [107, 119].

In order to detect a further limitation of the present methodology, the single-cross microstructure has been subject to a topological undulation of the connecting struts in chapter 11. Due to local bending-driven reorientation processes within the connecting struts, it has been shown this structure to feature an auxetic character involving an inherent coupling between the shear and the stretching degrees of freedom. Moreover, the bending effects due to restricted boundary rotations have been predicted in a qualitative way. But apparently, the absolute value of the resulting boundary stiffening and softening effects could not be reproduced. Whereas the periodic properties have been displayed adequately exact, the description of the bending dominated

boundary layers has failed. By consequence, the quadratic bending deformation modes provided by the micromorphic projection polynomial do not comprise all essential deformation mechanisms.

Altogether, let us conclude the introduced micromorphic two-scale approach to offer a powerful methodology for the description of cellular materials with comparable macroscopic and microscopic length scales and with an adequate regular microtopology, allowing for a clear connection between microscopic processes and extended degrees of freedom. The significance of the described boundary layer effects, which are able to cause an effective structural stiffening up to 30 %, becomes apparent having in mind light-weight constructions, especially for layered composites such as the demonstrated sandwich structure. Nevertheless one may insist that the numerical experiments within the present work have undergone very severe restrictions. In the future, further efforts have to be made taking into account microstructures with superimposed stochastic perturbations. The application of the methodology to three-dimensional structures would allow for a verification in physical experiments such as indicated in fig. 10.8. Furthermore, the methodology may offer the possibility to learn more about the structure of appropriate macroscopic micromorphic constitutive equations. With respect of the huge amount of unknown material parameters, each reduction of the parameter set would help to identify reliable constitutive relations applying inverse techniques.

Finally, the proposed methodology bears the potential to be extended to even higher order micromorphic continua, e. g. with a view to the micromechanical modelling of semiflexible biopolymer networks comprising reorientation processes based on higher order bending effects. Not least in that case, the computation of the numerical experiments within a geometrical nonlinear regime would be of high interest.

A

Alternative choice of the micromorphic projection polynomial

In chapter 5, the cubic projection polynomial eq. (5.9) has been introduced including the purely macroscopic coefficient tensors \mathbf{A}_M^1 , \mathbf{B}_M^2 , \mathbf{C}_M^3 and \mathbf{D}_M^4 . If one considers only the odd polynomial links, one may identify four linear deformation modes as well as eight independent cubic deformation modes (two-dimensional case). Concurrently, the averaging rules eqs. (5.4) – (5.8) indicate the odd deformation modes to depend on the macroscopic displacement gradient $\text{GRAD } \mathbf{u}_M$ and on the microdeformation $\bar{\boldsymbol{\chi}}_M$. I. e. there are only eight macroscopic deformation components available. By consequence, further assumptions have to be taken into account in order to reduce the number of independent deformation modes. In the present contribution, only the periodic parts of the cubic polynomial link have been considered,

$$\Delta u_1^{\text{cub}} = \frac{1}{6}(D_{M1111} \Delta X_1^3 + D_{M1222} \Delta X_2^3), \quad (\text{A.1})$$

$$\Delta u_2^{\text{cub}} = \frac{1}{6}(D_{M2111} \Delta X_1^3 + D_{M2222} \Delta X_2^3), \quad (\text{A.2})$$

whereas the deformation modes depending on $\Delta X_1^2 \Delta X_2$ and $\Delta X_1 \Delta X_2^2$ have been neglected. Doing so, it has been shown in chapter 5 the microdeformation $\bar{\chi}_M$ not to contribute to any effective deformation state. By contrast, some periodic *inner* deformation modes are activated resulting in a cubic fluctuation of the boundary displacements, cf. fig. 5.1.

The proposed projection polynomial fulfils the above mentioned averaging rules a priori. But, of course, this choice is not unique. Forest et al. [39, 45] have introduced a different definition of the projection polynomial. In order to identify the unknown polynomial coefficients in terms of the macroscopic deformation quantities, the linear deformation modes have been assumed solely to depend on the macroscopic displacement gradient $\text{GRAD } \mathbf{u}_M$, resulting in four side conditions and completing the equation system. Doing so, the linear polynomial link reads

$$\Delta u_1^{\text{lin}} = u_{M1,1} \Delta X_1 + u_{M1,2} \Delta X_2, \quad (\text{A.3})$$

$$\Delta u_2^{\text{lin}} = u_{M2,1} \Delta X_1 + u_{M2,2} \Delta X_2 \quad (\text{A.4})$$

and the cubic one

$$\begin{aligned} \Delta u_1^{\text{cub}} = & -\frac{10}{l^2} \left(\chi_{M11}^* (\Delta X_1^3 - 3 \Delta X_1 \Delta X_2^2) \right. \\ & \left. + \chi_{M12}^* (\Delta X_2^3 - 3 \Delta X_1^2 \Delta X_2) \right), \end{aligned} \quad (\text{A.5})$$

$$\begin{aligned} \Delta u_2^{\text{cub}} = & -\frac{10}{l^2} \left(\chi_{M21}^* (\Delta X_1^3 - 3 \Delta X_1 \Delta X_2^2) \right. \\ & \left. + \chi_{M22}^* (\Delta X_2^3 - 3 \Delta X_1^2 \Delta X_2) \right) \end{aligned} \quad (\text{A.6})$$

for a square unit cell of the size l^2 . The difference deformation defines as

$$\chi_M^* = \text{GRAD } \mathbf{u}_M - (\bar{\chi}_M - 1). \quad (\text{A.7})$$

A square microvolume of the edge length l , deformed depending on the horizontal components of $\text{GRAD } \mathbf{u}_M$ and $\bar{\chi}_M$, is depicted in fig. A.1.

Apparently, the coupling behaviour between the macroscopic displacement gradient and the microdeformation is much more pronounced than it has

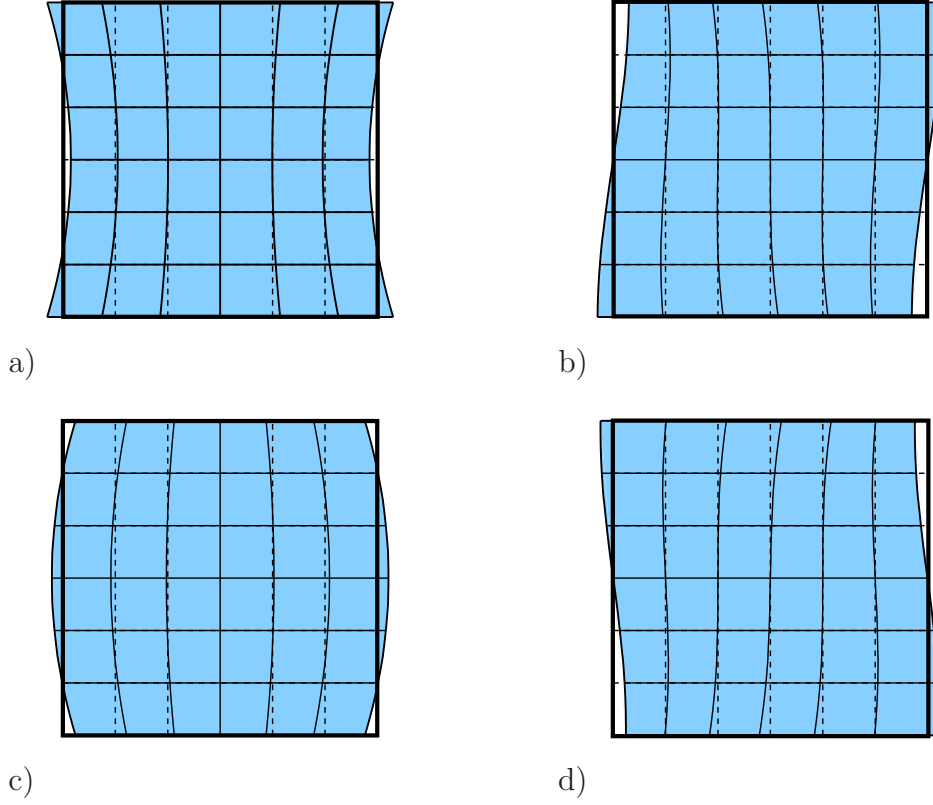


Figure A.1: Alternative odd deformation modes proposed in [45], depending on a) u_{M11} , b) u_{M12} , c) $\bar{\chi}_{M11} - 1$ and d) $\bar{\chi}_{M12}$ for a quadratic microvolume.

been for the projection rule proposed in chapter 5. Let us study again the displacement in dependence of $u_{M1,2} = \bar{u}$ at position $\Delta X_1 = 0$, $\Delta X_2 = l/2$. One finds

$$\Delta u_1^{\text{alternative}} \left(\Delta X_1 = 0, \Delta X_2 = \frac{l}{2} \right) = \bar{u} \frac{l}{2} + \frac{10}{l^2} \frac{l^3}{8} = \bar{u} \frac{7}{4} l, \quad (\text{A.8})$$

whereas the first order approach accounts for

$$\Delta u_1^{\text{1st order}} \left(\Delta X_1 = 0, \Delta X_2 = \frac{l}{2} \right) = \bar{u} \frac{l}{2}. \quad (\text{A.9})$$

The microscopic deformation induced by the macroscopic displacement gra-

dient does not equal the effective deformation on the macroscale and the difference has to be equalised by the microshear deformation. By consequence, the decoupling of the linear deformation modes requires the microdeformations to contribute to the effective deformation and therefore induces vice versa an inherent coupling between the macro- and the microdeformations. From the physical point of view, at least for the geometries investigated in the present work, this alternative choice of the projection polynomial is not meaningful. Nevertheless, this second polynomial satisfies the averaging rules introduced in chapter 5. Note that the curvature deformation modes are not concerned by the different formulations.

Summing up, one may conclude that the choice of the additional restrictions for the projection polynomial must correspond to the deformation mechanisms essential for the underlying microstructure. Analogously, there is no methodical need to establish a polynomial projection rule. If required, one may also introduce an arbitrary function within the limits defined by the averaging rules.

B

Downwards compatibility

By introduction of the micromorphic homogenisation technique, the question arises if the two-scale approach coincides under certain conditions with the first order approach. Or clearly spoken: Is the proposed scheme downwards compatible?

For that purpose, let us reflect again the proposed projection polynomial eq. (5.16)

$$\begin{aligned} \Delta \mathbf{u} = & \frac{1}{2} \left(-\text{GRAD } \bar{\boldsymbol{\chi}}_M : \mathbf{G} + (5(\bar{\boldsymbol{\chi}}_M - \mathbf{I}) - 3 \text{GRAD } \mathbf{u}_M) \cdot \Delta \mathbf{X} \right. \\ & \left. + \text{GRAD } \bar{\boldsymbol{\chi}}_M : (\Delta \mathbf{X} \otimes \Delta \mathbf{X}) \right) \\ & - \frac{1}{6} \left(5((\bar{\boldsymbol{\chi}}_M - \mathbf{I}) - \text{GRAD } \mathbf{u}_M) \cdot \overset{4}{\mathbf{I}} \cdot \mathbf{G}^{-1} \right) : (\Delta \mathbf{X} \otimes \Delta \mathbf{X} \otimes \Delta \mathbf{X}). \end{aligned} \quad (\text{B.1})$$

Putting the projection rule in the context of the second gradient continuum

theory, let us furthermore establish the internal constraint

$$\bar{\boldsymbol{\chi}}_M = \mathbf{F}_M, \quad (\text{B.2})$$

i. e. the microdeformation $\bar{\boldsymbol{\chi}}_M$ does not longer comprise an independent microscopic deformation quantity but is strictly coupled to the macrodeformation \mathbf{F}_M . By consequence, the projection polynomial collapses towards the purely quadratic polynomial

$$\Delta \mathbf{u} = \text{GRAD } \mathbf{u}_M \cdot \Delta \mathbf{X} + \frac{1}{2} \left(\text{GRAD } \mathbf{F}_M : (\Delta \mathbf{X} \otimes \Delta \mathbf{X} - \mathbf{G}) \right), \quad (\text{B.3})$$

taking into account the constant rigid body translation equalising the volume centroid's shifting induced by the quadratic modes. The resulting expression corresponds exactly to the kinematic projection found by Kouznetsova et al. [77, 79] for the second gradient continuum theory on the macroscale. Apparently, the cubic polynomial link, which can be interpreted as the difference of the total microscopic deformation and the macroscopic deformation, does not appear any more.¹

If one furthermore assumes the microvolume l^2 attached to the macroscopic material point to be very small, i. e. $l \rightarrow 0$, the quadratic polynomial link, which is of the order $\mathcal{O}(l^2)$ can be neglected and the projection polynomial reduces to the linear expression

$$\Delta \mathbf{u} = \text{GRAD } \mathbf{u}_M \cdot \Delta \mathbf{X}, \quad (\text{B.4})$$

continuously ignoring any periodic fluctuations. Thus, this second reduction implies a perfect separation between the macroscopic length scale and the microscopic one. Since only the first gradient of the macroscopic displacement field is taken into account, this last expression describes the micro-to-macro transition for the case of a macroscopic first gradient continuum theory, i. e. the standard Cauchy continuum theory. The appropriate homogenisation rules for the stress quantities follow by a correct evaluation of the particular form of the Hill-Mandel condition. Note that the analogous

¹Note, that the given geometrical interpretation of the difference deformation $\bar{\boldsymbol{\chi}}_M^* = \bar{\boldsymbol{\chi}}_M - \mathbf{F}_M$ is only valid for the small deformation regime. For the geometrically nonlinear context, the relation $\bar{\mathbf{E}}_M = \bar{\boldsymbol{\chi}}_M \cdot \mathbf{F}_M^{-1} - \mathbf{I} = (\bar{\boldsymbol{\chi}}_M - \mathbf{F}_M) \cdot \mathbf{F}_M^{-1}$ has to be taken into account for the geometrical interpretation, which is in fact an objective strain measure.

reduction of the projection polynomial holds if one chooses the alternative projection polynomial eqs. (A.5) and (A.6) following Forest et al. [39, 45].

In order to confirm the found downwards compatibility, let us consider the homogenisation of a homogeneous microvolume. Therefore, one may compute a shear experiment of a infinitely large domain, cf. fig. 8.2. For the geometrical interpretation of the micromorphic degrees of freedom is not clear in the case of a homogeneous microcontinuum, let us assume the microdeformation to be left unprescribed at the boundaries, i. e. no clamping conditions. Furthermore, the microvolume is assumed to be several orders of magnitude smaller than the macroscopic sample size h .²

Finally, one finds the shear test to prescribe a homogeneous shear deformation throughout the whole sample volume, $u_{M1,2} = \bar{u}/h$ and the microshear deformation calculates as $\bar{\chi}_{M12} = u_{M1,2}$. The homogeneous shear stress corresponds to the analytical solution. Analogous results are found for different loading states. Apparently, the homogeneous microcontinuum comprises the choice of the internal constraint $\bar{\chi}_M = \mathbf{F}_M$. Again, the choice of the alternative projection polynomial eqs. (A.5) and (A.6) produces the identical results. With respect to the simplicity of the result, no plot has been added at this point.

²From the technical point of view, one also may equivalently choose the microvolume size comparable to the macroscopic sample size while suppressing the quadratic deformation modes and neglecting the resulting couple stresses.

C

Balance equations in the weak form

The numerical investigations within the present contribution are based on the solution of a set of coupled partial differential equations (PDE), i. e. the balance of momentum and the balance of momentum moments, applying the Finite Element Method (FEM), cf. e. g. [129].

Doing so, the so-called strong formulation of the balance equations has to be transformed into the weak form. Any volume forces and volume double forces will be neglected in the sequel. Considering the physical body \mathcal{B}_0 , let us introduce Dirichlet and Neumann boundary conditions

$$\mathbf{u} = \mathbf{u}_0, \quad \bar{\boldsymbol{\chi}} = \bar{\boldsymbol{\chi}}_0 \quad \text{on} \quad \partial\mathcal{B}_0^D, \quad (\text{C.1})$$

$$\mathbf{P} \cdot \mathbf{N} = \mathbf{p}_0, \quad \mathbf{Q} \cdot \mathbf{N} = \mathbf{q}_0 \quad \text{on} \quad \partial\mathcal{B}_0^N, \quad (\text{C.2})$$

where

$$\partial\mathcal{B}_0^D \cup \partial\mathcal{B}_0^N = \partial\mathcal{B}_0 \quad \text{and} \quad \partial\mathcal{B}_0^D \cap \partial\mathcal{B}_0^N = \{\}. \quad (\text{C.3})$$

Balance of momentum

The strong formulation of the balance of momentum within the material frame reads¹

$$\text{DIV } \mathbf{P} = \mathbf{0}. \quad (\text{C.4})$$

To generate the weak formulation, the balance equation has to be multiplied with an appropriate testing function $\delta \mathbf{u}$, where $\delta \mathbf{u} = \mathbf{0}$ on $\partial \mathcal{B}_0^D$. Furthermore, the resulting expression is integrated over the volume captured by the physical body \mathcal{B}_0 ,

$$\int_{\mathcal{B}_0} \delta \mathbf{u} \cdot \text{DIV } \mathbf{P} \, dV = 0, \quad (\text{C.5})$$

$$\Leftrightarrow \underbrace{\int_{\partial \mathcal{B}_0^N} \delta \mathbf{u} \cdot \mathbf{p}_0 \, dA}_{\text{Neumann BC}} - \int_{\mathcal{B}_0} \underbrace{\text{GRAD } \delta \mathbf{u} : \mathbf{P}}_{\text{residual } \mathcal{R}_i} \, dV = 0, \quad (\text{C.6})$$

where one integration by parts and the Neumann boundary condition have been applied. For the implementation within COMSOL Multiphysics[®], the local residuals have to be computed for each testing function $\delta \mathbf{u}$ and one finds

$$\mathcal{R}_1 = \delta u_{1,1} P_{11} + \delta u_{1,2} P_{12}, \quad (\text{C.7})$$

$$\mathcal{R}_2 = \delta u_{2,1} P_{21} + \delta u_{2,2} P_{22}. \quad (\text{C.8})$$

¹Besides the symmetry conditions for the Cauchy stress tensor, the balance of momentum exhibits the identical structure for both, the classical Cauchy continuum as well as for the extended micromorphic continuum.

Balance of moments of momentum

The strong formulation of the balance of moments of momentum within the material frame reads

$$\text{Div } \mathbf{Q}^3 + (\mathbf{P} - \mathbf{S}) \cdot \mathbf{F}^T = \mathbf{0}. \quad (\text{C.9})$$

By multiplication with the testing function $\delta\bar{\chi}$, where $\delta\bar{\chi} = \mathbf{0}$ on $\partial\mathcal{B}_0^D$, and by integration over the volume captured by the body \mathcal{B}_0 , one finds the weak formulation

$$\int_{\mathcal{B}_0} \delta\bar{\chi} : (\text{Div } \mathbf{Q}^3 + (\mathbf{P} - \mathbf{S}) \cdot \mathbf{F}^T) \, dV = 0 \quad (\text{C.10})$$

$$\Leftrightarrow \underbrace{\int_{\partial\mathcal{B}_0^D} \delta\bar{\chi} : \mathbf{q}_0 \, dA}_{\text{Neumann BC}} - \int_{\mathcal{B}_0} \underbrace{\left(\text{GRAD } \delta\bar{\chi} : \mathbf{Q}^3 - \delta\bar{\chi} : (\mathbf{P} - \mathbf{S}) \cdot \mathbf{F}^T \right)}_{\text{residual } \mathcal{R}_i} \, dV = 0, \quad (\text{C.11})$$

where again one integration in parts has been applied. Furthermore, the Neumann boundary condition for the surface double traction has been inserted. The local residuals calculate as follows:

$$\begin{aligned} \mathcal{R}_3 &= \delta\bar{\chi}_{11,1} Q_{111} + \delta\bar{\chi}_{11,2} Q_{112} \\ &\quad - \delta\bar{\chi}_{11} \left((P_{11} - S_{11}) F_{11} + (P_{12} - S_{12}) F_{12} \right), \end{aligned} \quad (\text{C.12})$$

$$\begin{aligned} \mathcal{R}_4 &= \delta\bar{\chi}_{12,1} Q_{121} + \delta\bar{\chi}_{12,2} Q_{122} \\ &\quad - \delta\bar{\chi}_{12} \left((P_{11} - S_{11}) F_{21} + (P_{12} - S_{12}) F_{22} \right), \end{aligned} \quad (\text{C.13})$$

$$\begin{aligned} \mathcal{R}_5 &= \delta\bar{\chi}_{21,1} Q_{211} + \delta\bar{\chi}_{21,2} Q_{212} \\ &\quad - \delta\bar{\chi}_{21} \left((P_{21} - S_{21}) F_{11} + (P_{22} - S_{22}) F_{12} \right), \end{aligned} \quad (\text{C.14})$$

$$\begin{aligned} \mathcal{R}_6 &= \delta\bar{\chi}_{22,1} Q_{221} + \delta\bar{\chi}_{22,2} Q_{222} \\ &\quad - \delta\bar{\chi}_{22} \left((P_{21} - S_{21}) F_{21} + (P_{22} - S_{22}) F_{22} \right). \end{aligned} \quad (\text{C.15})$$

Sandwich structure

As it has been mentioned earlier, special attention has to be paid to the macroscale numerical implementation of the sandwich structure in chapter 10. Whereas the cellular kernel requires a micromorphic continuum formulation on the macroscale, the compact surface sheets follow Hooke's law in the context of the classical Cauchy continuum formulation.

For the micromorphic kernel, the residuals are formulated following eqs. (C.7) and (C.8) as well as eqs. (C.12) – (C.15). At the interface between the cellular kernel and the surface sheets, the microdeformation $\bar{\chi}$ has to be restricted. To do so, the residuals of the balance of momentum moments are modified applying a penalty multiplier λ ,

$$\mathcal{R}_3 = \lambda (\bar{\chi}_{11} - 1), \quad (\text{C.16})$$

$$\mathcal{R}_4 = \lambda \bar{\chi}_{12}, \quad (\text{C.17})$$

$$\mathcal{R}_5 = \lambda \bar{\chi}_{21}, \quad (\text{C.18})$$

$$\mathcal{R}_6 = \lambda (\bar{\chi}_{22} - 1). \quad (\text{C.19})$$

If the penalty multiplier λ is chosen large, the Finite Element Method calculates the microdeformation $\bar{\chi}$ to equal the identity within the surface layers. Thus, at the interface between the kernel and the surface sheets, the microdeformation degrees of freedom undergo the same restrictions as at a rigid boundary.

Bibliography

- [1] ALTENBACH, J. & H. ALTENBACH [1994]. *Einführung in die Kontinuumsmechanik*. B. G. Teubner, Stuttgart.
- [2] ALTENBACH, J., H. ALTENBACH & V. A. EREMEYEV [2010]. ‘On generalized Cosserat-type theories of plates and shells: A short review and bibliography.’ *Arch. Appl. Mech.*, **80**, pp. 73–92.
- [3] ANDERSON, W. B., C. P. CHEN & R. S. LAKES [1994]. ‘Experimental study of size effects and surface damage in closed-cell polymethacrylimide and open-cell copper foams.’ *Cellular polymers*, **13(1)**, pp. 1–15.
- [4] ANDERSON, W. B. & R. S. LAKES [1994]. ‘Size effects due to Cosserat elasticity and surface damage in closed-cell polymethacrylimide foam.’ *J. Mat. Sci.*, **29**, pp. 6413–6419.
- [5] ANDREWS, E. W., G. GIOUX, P. R. ONCK & L. J. GIBSON [2001]. ‘Size effects in ductile cellular solids. Part II: Experimental results.’ *Int. J. Mech. Sci.*, **43**, pp. 701–713.
- [6] BADUR, J. & H. STUMPF [1989]. *On the influence of E. and F. Cosserat on modern continuum mechanics and field theory*. Mitteilungen aus dem Institut für Mechanik Nr. 72, Ruhr-Universität Bochum.
- [7] BAŽANT, Z. P. & M. CHRISTENSEN [1972]. ‘Analogy between micropolar continuum and grid frameworks under initial stress.’ *Int. J. Solids Structures*, **8**, pp. 327–346.
- [8] BECKER, E. & W. BÜRGER [1976]. *Kontinuumsmechanik*.

- [9] BEREZOVSKI, A., J. ENGELBRECHT & G. A. MAUGIN [2010]. ‘Generalized thermomechanics with dual internal variables.’ *Arch. Appl. Mech.*, **article in press**.
- [10] BLUMENFELD, R. [2005]. ‘Auxetic strains – insight from iso-auxetic materials.’ *Molecular Simulation*, **31(13)**, pp. 867–871.
- [11] DE BOER, R. [1982]. *Vektor- und Tensorrechnung für Ingenieure*. Springer Verlag, Berlin.
- [12] DE BORST, R. [1991]. ‘Simulation of strain localization: A reappraisal of the Cosserat continuum.’ *Eng. Comp.*, **8**, pp. 317–332.
- [13] BREZNY, R. & D. J. GREEN [1990]. ‘Characterization of edge effects in cellular materials.’ *J. Mat. Sci.*, **25**, pp. 4571–4578.
- [14] BUXTON, G. A. & N. CLARKE [2007]. ‘Bending to stretching transition in disordered networks.’ *Phys. Rev. Lett.*, **98(23)**, pp. 238103.
- [15] CADDOCK, B. D. & K. E. EVANS [1989]. ‘Microporous materials with negative Poisson’s ratio: I. Microstructure and mechanical properties.’ *J. Physics D: Appl. Phys.*, **22**, pp. 1877–1882.
- [16] CAPRIZ, G. [1980]. *Continua with Microstructures*, volume 35 of *Springer Tracts in Natural Philosophy*. Springer, New York.
- [17] CHEN, C. & N. A. FLECK [2002]. ‘Size effects in the constrained deformation of metallic foams.’ *J. Mech. Phys. Solids*, **50**, pp. 955–977.
- [18] COSSERAT, E. & F. COSSERAT [1909]. *Théorie des corps déformables*. A. Hermann et Fils, Paris.
- [19] DAS, M., F. C. MACKINTOSH & A. J. LEVINE [2007]. ‘Effective medium theory of semiflexible filamentous networks.’ *Phys. Rev. Lett.*, **99(3)**, pp. 038101.
- [20] DIEBELS, S. [1999]. ‘Ein mikropolares Materialgesetz für poröse Festkörper.’ *Z. Angew. Math. Mech.*, **79**, pp. S533–S534.
- [21] DIEBELS, S. [2000]. *Mikropolare Zweiphasenmodelle: Modellierung auf der Basis der Theorie Poröser Medien*. Habilitationsschrift, Institut für Mechanik (Bauwesen), Nr. II-4, Universität Stuttgart.

- [22] DIEBELS, S. & H. STEEB [2002]. ‘The size effect in foams and its theoretical and numerical investigation.’ *Proc. R. Soc. Lond. A*, **458**, pp. 2869–2883.
- [23] DIEBELS, S. & H. STEEB [2003]. ‘Stress and couple stress in foams.’ *Comp. Mat. Science*, **28**, pp. 714–722.
- [24] DILLARD, T., S. FOREST & P. IENNY [2006]. ‘Micromorphic continuum modelling of the deformation and fracture behaviour of Nickel foams.’ *Eur. J. Mech., A/Solids*, **25 (3)**, pp. 526–549.
- [25] VAN DILLEN, T., P. R. ONCK & E. V. DER GIESSEN [2008]. ‘Models for stiffening in cross-linked biopolymer networks: A comparative study.’ *J. Mech. Phys. Solids*, **56**, pp. 2240–2264.
- [26] EBINGER, T., S. DIEBELS & H. STEEB [2007]. ‘Numerical homogenization techniques applied to growth and remodelling phenomena.’ *Comp. Mech.*, pp. 815–830.
- [27] EBINGER, T., H. STEEB & S. DIEBELS [2005]. ‘Modeling and homogenization of foams.’ *Comp. Assisted Mechanics and Engineering Sciences*, **12**, pp. 49–63.
- [28] EBINGER, T., H. STEEB & S. DIEBELS [2005]. ‘Modeling macroscopic extended continua with the aid of numerical homogenization schemes.’ *Comp. Mat. Science*, **32**, pp. 337–347.
- [29] EBINGER, T., H. STEEB & S. DIEBELS [2008]. ‘Kinematically extended continuum theories: Correlation between microscopic deformation and macroscopical strain measures.’ *Technische Mechanik*, **28 (2)**, pp. 64–86.
- [30] EHLERS, W., E. RAMM, S. DIEBELS & G. A. D’ADDETTA [2003]. ‘From particle ensembles to Cosserat continua: Homogenization of contact forces towards stresses and couple stresses.’ *Int. J. Solids Structures*, **40**, pp. 6681–6702.
- [31] EHLERS, W. & W. VOLK [1997]. ‘On shear band localization phenomena of liquid-saturated granular elastoplastic porous solid materials accounting for fluid viscosity and micropolar solid rotations.’ **2 (4)**, pp. 301–320.
- [32] ERINGEN, A. C. [1966]. ‘Linear theory of micropolar elasticity.’ *Math. Mech.*, **15(6)**, pp. 909–923.

- [33] ERINGEN, A. C. & E. S. SUHUBI [1964]. ‘Nonlinear theory of simple micro-elastic solids - I.’ *Int. J. Engng. Sci.*, **2**, pp. 189–203.
- [34] ERINGEN, C. [1976]. *Polar and Nonlocal Field Theories*, volume IV of *Continuum Physics*. Academic Press, Boston-New York.
- [35] ERINGEN, C. [1999]. *Microcontinuum Field Theories, Vol. I: Foundations and Solids*. Springer-Verlag, Berlin.
- [36] EVANS, K. E. & B. D. CADDOCK [1989]. ‘Microporous materials with negative Poisson’s ratio: II. Mechanisms and interpretation.’ *J. Physics D: Appl. Phys.*, pp. 1883–1887.
- [37] FEYEL, F. [1998]. *Application du calcul parallèle aux modèles à grand nombre de variables internes*. PhD-thesis, Ecole National Supérieure des Mines de Paris, Paris, France,.
- [38] FEYEL, F. & J. L. CHABOCHE [2000]. ‘FE² multiscale approach for modelling the elastoviscoplastic behaviour of long fiber SiC/Ti composite materials.’ *Comp. Meth. Appl. Mech. Eng.*, **183**, pp. 309–330.
- [39] FOREST, S. [1998]. ‘Mechanics of generalized continua: Construction by homogenization.’ *J. Phys. IV*, pp. 39–48.
- [40] FOREST, S. [2002]. ‘Homogenization methods and the mechanics of generalized continua - Part 2.’ *Theoretical and Applied Mechanics*, **28–29**, pp. 113–143.
- [41] FOREST, S. [2006]. ‘Nonlinear microstrain theories.’ *Int. J. Solids Structures*, **43**, pp. 7224–7245.
- [42] FOREST, S. [2009]. ‘Micromorphic approach for gradient elasticity, viscoplasticity, and damage.’ *J. Eng. Mech.*, **135 (3)**, pp. 117–131.
- [43] FOREST, S., F. BARBE & G. CAILLETAUD [2000]. ‘Cosserat modelling of size effects in the mechanical behaviour of polycrystals and multi-phase materials.’ *Int. J. Solids Structures*, **37**, pp. 7105–7126.
- [44] FOREST, S., J. M. CARDONA & R. SIEVERT [2000]. ‘Thermoelasticity of second-grade media.’ In *Continuum Thermomechanics, The Art and Science of Modelling Material Behaviour*, edited by G. Maugin, R. Drouot & F. Sidoroff, Paul Germain’s Anniversary Volume, pp. 163–176. Kluwer Academic Publishers, Dordrecht.

- [45] FOREST, S. & K. SAB [1998]. ‘Cosserat overall modeling of heterogeneous materials.’ *Mech. Res. Commun.*, **25**, pp. 449–454.
- [46] FRIIS, E. A., R. S. LAKES & J. B. PARK [1988]. ‘Negative Poisson’s ratio polymeric and metallic foams.’ *J. Mat. Sci.*, **23**, pp. 4406–4414.
- [47] GEERS, M. G. D., V. G. KOUZNETSOVA & W. A. M. BREKELMANS [2001]. ‘Gradient-enhanced computational homogenization for the micro-macro scale transition.’ **11**, pp. 145–152.
- [48] GERMAIN, P. [1973]. ‘La méthode des puissances virtuelles en mécanique des milieux continus, Première partie: Théorie du second gradient.’ *J. Mecanique*, **12**, pp. 235–274.
- [49] GERMAIN, P. [1973]. ‘The method of virtual power in continuum mechanics. Part 2: Microstructure.’ *SIAM J. Appl. Math.*, **25**, pp. 556–575.
- [50] GIBSON, L. J. & M. F. ASHBY [1997]. *Cellular solids. Structure and properties*. Cambridge Solid State Science Series. Cambridge University Press, Cambridge.
- [51] GOLDSTEIN, H. [1963]. *Klassische Mechanik*. Akademische Verlagsgesellschaft, Frankfurt am Main.
- [52] GRAMMENOUDIS, P. & C. TSAKMAKIS [2009]. ‘Micromorphic continuum Part I: Strain and stress tensors and their associated rates.’ *Int. J. Non Lin. Mech.*, **44** (9), pp. 943–956.
- [53] GRENESTEDT, J. L. [1999]. ‘Effective elastic behaviour of some models for ‘perfect’ cellular solids.’ *Int. J. Solids Structures*, **36**, pp. 1471–1501.
- [54] GÜNTHER, W. [1958]. ‘Zur Statik und Kinematik des Cosseratschen Kontinuums.’ *Abhandlungen der Braunschweigischen Wissenschaftlichen Gesellschaft*, **10**, pp. 195–213.
- [55] HAIN, M. [2007]. *Computational homogenization of micro-structural damage due to frost in hardened cement paste*. Dissertation, Leibniz-Universität Hannover.
- [56] HAMEL, G. [1912]. *Elementare Mechanik*. Teubner, Leipzig.
- [57] HATAMI-MARBINI, H. & R. C. PICU [2008]. ‘Scaling of nonaffine deformation in random semiflexible fiber networks.’ *Phys. Rev. E*, **77**(6), pp. 062103.

- [58] HAUPT, P. [2000]. *Continuum Mechanics and Theory of Materials*. Springer-Verlag, Berlin.
- [59] HAUPT, P. & C. TSAKMAKIS [1989]. ‘On the application of dual variables in continuum mechanics.’ *Continuum Mech. Therm.*, **1**, pp. 165–196.
- [60] HEAD, D. A., A. J. LEVINE & F. C. MACKINTOSH [2003]. ‘Deformation of cross-linked semiflexible polymer networks.’ *Phys. Rev. Lett.*, **91** (10), pp. (108102), 1–4.
- [61] HILL, R. [1963]. ‘Elastic properties of reinforced solids: Some theoretical principles.’ *J. Mech. Phys. Solids*, **11**, pp. 357–372.
- [62] HILL, R. [1972]. ‘On constitutive macro-variables for heterogeneous solids at finite strain.’ *Proc. R. Soc. Lond. A*, **326**, pp. 131–147.
- [63] HIRSCHBERGER, C. B. [2008]. *A Treatise on Micromorphic Continua. Theory, Computation, Homogenization*. Ph.D. thesis, Technische Universität Kaiserslautern.
- [64] HIRSCHBERGER, C. B., E. KUHL & P. STEINMANN [2007]. ‘On deformational and configurational mechanics of micromorphic elasticity - Theory and computation.’ *Comp. Meth. Appl. Mech. Eng.*, **196** (41–44), pp. 4027–4044.
- [65] HIRSCHBERGER, C. B., N. SUKUMAR & P. STEINMANN [2008]. ‘Computational homogenization of material layers with micromorphic mesostructure.’ *Phil. Mag.*, **88** (30–32), pp. 3603–3631.
- [66] HUET, C. [1999]. ‘Coupled size and boundary-condition effects in viscoelastic heterogeneous and composite bodies.’ *Mech. Mater.*, **31**, pp. 787–829.
- [67] JANG, W. Y., A. M. KRAYNIK & S. KYRIAKIDES [2008]. ‘On the microstructure of open-cell foams and its effect on elastic properties.’ *Int. J. Engng. Sci.*, **45**(7–8), pp. 1845–1875.
- [68] JÄNICKE, R. & S. DIEBELS [2009]. ‘A numerical homogenisation strategy for micromorphic continua.’ *Nuovo Cimento Soc. Ital. Fis. C*, **31** (1), pp. 121–132.
- [69] JÄNICKE, R. & S. DIEBELS [2010]. ‘Numerical homogenisation of micromorphic media.’ *Technische Mechanik*, **30**(4), pp. 364–373.

- [70] JÄNICKE, R. & S. DIEBELS [2010]. ‘Requirements on Periodic Micromorphic Media.’ In *Mechanics of Generalized Continua*, edited by G. A. Maugin & A. Metrikine, pp. 99–108. Springer-Verlag, Berlin.
- [71] JÄNICKE, R., S. DIEBELS, H. G. SEHLHORST & A. DÜSTER [2009]. ‘Two-scale modelling of micromorphic continua.’ *Continuum Mech. Therm.*, **21** (4), pp. 297–315.
- [72] JANMEY, P. A., S. HVIDT, J. KÄS, D. LERCHE, A. MAGGS, E. SACKMANN, M. SCHLIWA & T. P. STOSSEL [1994]. ‘The mechanical properties of actin gels: Elastic modulus and filament motions.’ *J. Biol. Chem.*, **269**(51), pp. 32503–32513.
- [73] JOHLITZ, M., S. DIEBELS, J. BATAL, H. STEEB & W. POSSART [2008]. ‘Size effects in polyurethane bonds: Experiments, modelling and parameter identification.’ *J. Mat. Sci.*, **43**, pp. 4768–4779.
- [74] KACZMARCZYK, L., C. J. PEARCE & N. BIĆANIĆ [2008]. ‘Scale transition and enforcement of RVE boundary conditions in second-order homogenization.’ *Int. J. Numer. Meth. Eng.*, **74**, pp. 506–522.
- [75] KIRCHNER, N. & P. STEINMANN [2007]. ‘Mechanics of extended continua: modeling and simulation of elastic microstretch materials.’ *Comp. Mech.*, **40**(4), pp. 651–666.
- [76] KOUZNETSOVA, V. G., , M. G. D. GEERS & W. A. M. BREKELMANS [2004]. ‘Size of a representative volume element in a second-order computational homogenization framework.’ *Int. J. of Multiscale Computational Engineering*, pp. 575–598.
- [77] KOUZNETSOVA, V. G. [2002]. *Computational homogenization for the multi-scale analysis of multi-phase materials*. PhD-thesis, Technische Universiteit Eindhoven, The Netherlands.
- [78] KOUZNETSOVA, V. G., W. A. M. BREKELMANS & F. P. T. BAAIJENS [2001]. ‘An approach to micro-macro modeling of heterogeneous materials.’ *Comp. Mech.*, pp. 37–48.
- [79] KOUZNETSOVA, V. G., M. G. D. GEERS & W. A. M. BREKELMANS [2002]. ‘Multi-scale constitutive modelling of heterogeneous materials with a gradient-enhanced computational homogenization scheme.’ *Int. J. Numer. Meth. Eng.*, **54**, pp. 1235–1260.
- [80] KROY, K. & E. FREY [1996]. ‘Force-extension relation and plateau modulus for wormlike chains.’ **77**(2), pp. 306–309.

- [81] LADÈVEZE, P., O. LOISEAU & D. DUREISSEIX [2001]. ‘A micro-macro and parallel computational strategy for highly heterogeneous structures.’ *Int. J. Numer. Meth. Eng.*, **52**, pp. 121–138.
- [82] LAKES, R. S. [1983]. ‘Size effects and micromechanics of porous solids.’ *J. Mat. Sci.*, **18**, pp. 2572–2580.
- [83] LAKES, R. S. [1987]. ‘Foam Structures with a negative Poisson’s Ratio.’ *Science*, **235**, pp. 1038.
- [84] LARSSON, F. & K. RUNESSON [2006]. ‘Adaptive computational meso-macro-scale modeling of elastic composites.’ *Comp. Meth. Appl. Mech. Eng.*, **195**, pp. 324–338.
- [85] MACKINTOSH, F. C., J. KÄS & P. A. JANMEY [1995]. ‘Elasticity of semiflexible biopolymer networks.’ *Phys. Rev. Lett.*, **75(24)**, pp. 4425–4428.
- [86] MAUGIN, G. A. [1980]. ‘The method of virtual power in continuum mechanics: Application to coupled fields.’ *Acta Mech.*, **35**, pp. 1–70.
- [87] MAUGIN, G. A. [1992]. *The Thermomechanics of Plasticity and Fracture*. Cambridge University Press, Cambridge.
- [88] MICHEL, J.-C., H. MOULINEC & P. SUQUET [1999]. ‘Effective properties of composite materials with periodic microstructure: A computational approach.’ *Comp. Meth. Appl. Mech. Eng.*, **172**, pp. 109–143.
- [89] MIEHE, C. [1996]. ‘Numerical computation of algorithmic (consistent) tangent moduli in large-strain computational inelasticity.’ *Comp. Meth. Appl. Mech. Eng.*, **134**, pp. 223–240.
- [90] MIEHE, C. & A. KOCH [2002]. ‘Computational micro-to-macro transitions of discretized microstructures undergoing small strains.’ *Arch. Appl. Mech.*, **72**, pp. 300–317.
- [91] MIEHE, C., J. SCHOTTE & J. SCHRÖDER [1999]. ‘Computational micro-macro transitions and overall moduli in the analysis of polycrystals at large strains.’ *Comp. Mat. Science*, **16**, pp. 372–382.
- [92] MINDLIN, R. D. [1964]. ‘Micro-structure in linear elasticity.’ *Arch. Rat. Mech. Anal.*, **16**, pp. 51–78.
- [93] MINDLIN, R. D. [1965]. ‘Second gradient of strain and surface tension in linear elasticity.’ *Int. J. Solids Structures*, **1**, pp. 417–438.

- [94] MOULINEC, H. & P. SUQUET [1998]. ‘A numerical method for computing the overall response of non-linear composites with complex microstructure.’ *Comp. Meth. Appl. Mech. Eng.*, **157**, pp. 69–94.
- [95] MÜHLHAUS, H. B. [1990]. ‘Stress and couple stress in a layered half plane with surface loading.’ *Int. J. Numer. Anal. Met. Geomech.*, **14(8)**, pp. 545–563.
- [96] MÜHLHAUS, H. B. & E. C. AIFANTIS [1991]. ‘A variational principle for gradient plasticity.’ *Int. J. Solids Structures*, **28(7)**, pp. 845–857.
- [97] NEFF, P. [2004]. ‘On material constants for micromorphic continua.’ In *Proceedings of ‘International Symposium on Trends in Applications of Mathematics to Mechanics’*, edited by K. Hutter & Y. Wang. Shaker, Aachen.
- [98] NEFF, P. & S. FOREST [2007]. ‘A geometrically exact micromorphic model for elastic metallic foams accounting for affine microstructure. Modelling, existence of minimizers, identification of moduli and computational results.’ *J. Elasticity*, **87(2-3)**, pp. 239–276.
- [99] NEMAT-NASSER, S. & M. HORI [1993]. *Micromechanics*. North-Holland, Amsterdam.
- [100] ONCK, P. R., E. W. ANDREWS & L. J. GIBSON [2001]. ‘Size effects in ductile cellular solids. Part I: modeling.’ *Int. J. Mech. Sci.*, **43**, pp. 681–699.
- [101] ONCK, P. R., T. KOEMAN, T. VAN DILLEN & E. VAN DER GIESSEN [2005]. ‘Alternative explanation of stiffening in cross-linked semiflexible networks.’ *Phys. Rev. Lett.*, **95**, pp. 1–4.
- [102] PEERLINGS, R. H. J. & N. A. FLECK [2001]. ‘Numerical analysis of strain gradient effects in periodic media.’ *J. Phys. IV*, **11**, pp. 153–160.
- [103] PIDERI, C. & P. SEPPECHER [1997]. ‘A second gradient material resulting from the homogenization of an heterogeneous linear elastic medium.’ *Continuum Mech. Therm.*, **9**, pp. 241–257.
- [104] PODIO-GUIDUGLI, P. & M. VIANELLO [2010]. ‘Hypertractions and hyperstresses convey the same mechanical information.’ *Continuum Mech. Therm.*, **22**, pp. 163–176.

- [105] PRADEL, F. & K. SAB [1998]. ‘Homogenization of discrete media.’ *J. Phys. IV*, **8**, pp. 317–324. Proc. of Euromech-Mecamat 1997, Magdeburg.
- [106] RECHENBERG, I. [1973]. ‘Evolutionsstrategie: Optimierung technischer Systeme nach Prinzipien der biologischen Evolution.’ *Frommann-Holzboog, Stuttgart*.
- [107] SAB, K. & F. PRADEL [2009]. ‘Homogenisation of periodic Cosserat media.’ *Int. J. Comput. Appl. Technol.*, **34(1)**, pp. 60–71.
- [108] SCHAEFER, H. [1967]. ‘Das Cosserat-Kontinuum.’ *Z. Angew. Math. Mech.*, **47**, pp. 485–498.
- [109] SCHRÖDER, J. [2000]. *Homogenisierungsmethoden der nichtlinearen Kontinuumsmechanik unter Beachtung von Stabilitätsproblemen*. Habilitationsschrift, Institut für Mechanik (Bauwesen), Lehrstuhl I, Universität Stuttgart.
- [110] SCHWEFEL, H. P. [1995]. ‘Evolution and optimum seeking.’ *John Wiley & Sons, New York*.
- [111] SEHLHORST, H.-G., R. JÄNICKE, A. DÜSTER, E. RANK, H. STEEB & S. DIEBELS [2009]. ‘Numerical investigations of foam-like materials by nested high-order finite element methods.’ *Comp. Mech.*, **45 (1)**, pp. 45–59.
- [112] SHADWICK, R. E. [1999]. ‘Mechanical design in arteries.’ *J. Exp. Biol.*, **202**, pp. 3305–3313.
- [113] SHAH, J. V. & P. A. JANMEY [1997]. ‘Strain hardening of fibrin gels and plasma clots.’ *Rheol. Acta*, **36**, pp. 262–268.
- [114] VAN DER SLUIS, O. [2001]. *Homogenisation of structured elastoviscoplastic solids*. Ph.D. thesis, Eindhoven University of Technology, The Netherlands.
- [115] SMIT, R., W. BREKELMANS & H. MEIJER [1998]. ‘Prediction of the mechanical behaviour of nonlinear heterogeneous systems by multi-level finite element modelling.’ *Comp. Meth. Appl. Mech. Eng.*, **155**, pp. 181–192.
- [116] STEEB, H. & S. DIEBELS [2005]. ‘Continua with affine microstructure: Theoretical aspects and application.’ *Proc. Appl. Math. Mech.*, **5**, pp. 319–320.

- [117] STORM, C., J. J. PASTORE, F. C. MACKINTOSH, T. LUBENSKY & P. A. JANMEY [2005]. ‘Nonlinear elasticity in biological gels.’ *Nature*, **435**, pp. 191–194.
- [118] SVENDSEN, B. [1999]. ‘On the thermodynamics of thermoelastic materials with additional scalar degrees of freedom.’ *Continuum Mech. Therm.*, **4**, pp. 247–262.
- [119] TEKOĞLU, C. & P. R. ONCK [2005]. ‘Size effects in the mechanical behaviour of cellular materials.’ *J. Mat. Sci.*, **40**, pp. 5911–3564.
- [120] TEKOĞLU, C. & P. R. ONCK [2008]. ‘Size effects in two-dimensional voronoi foams: A comparison between generalized continua and discrete models.’ *J. Mech. Phys. Solids*, **56**, pp. 3541–3564.
- [121] TEMIZER, I. & P. WRIGGERS [2008]. ‘On a Mass Conservation Criterion in Micro-to-Macro Transitions.’ *J. Appl. Mech.*, **75**, pp. 0545031–0545034.
- [122] TERADA, K. & N. KIKUCHI [2001]. ‘A class of general algorithms for multi-scale analysis of heterogeneous media.’ *Comp. Meth. Appl. Mech. Eng.*, **190**, pp. 5427–5464.
- [123] TRUESDELL, C. A. & R. TOUPIN [1960]. *The classical field theories*. In S. Flügge (Herausgeber), *Handbuch der Physik III/1*, Springer-Verlag, Berlin.
- [124] VERNERY, F. J., W. K. LIU & B. MORAN [2007]. ‘Multi-scale micromorphic theory for hierarchical materials.’ *J. Mech. Phys. Solids*, **55** (12), pp. 2603–2651.
- [125] VERNERY, F. J., W. K. LIU, B. MORAN & G. OLSON [2008]. ‘A micromorphic model for the multiple scale failure of heterogeneous materials.’ *J. Mech. Phys. Solids*, **56** (4), pp. 1320–1347.
- [126] VOLK, W., S. DIEBELS, M. LÄTZEL & S. LUDING [2001]. ‘Analogiebetrachtungen für mikropolare Kontinua mit Anwendung auf den Biaxialversuch.’ In *Zur Beschreibung komplexen Materialverhaltens: Beiträge anlässlich des 50. Geburtstags von Herrn Prof. Dr.-Ing. Wolfgang Ehlers*, edited by S. Diebels, pp. 189–206. Institut für Mechanik (Bauwesen) Nr. 01-II-7, Universität Stuttgart.
- [127] WARREN, W. E. & A. M. KRAYNIK [1988]. ‘The linear elastic properties of open-cell foams.’ *J. Appl. Mech.*, **55**, pp. 341–346.

- [128] WARREN, W. E. & A. M. KRAYNIK [1991]. ‘The nonlinear elastic behavior of open-cell foams.’ *J. Appl. Mech.*, **58**, pp. 376–381.
- [129] ZIENKIEWICZ, O. C. & R. L. TAYLOR [1967]. *The Finite Element Method*, volume 1. McGraw-Hill Book Company, New York-London, fourth edition.